2017

The Role of Defects in the Metal-Nonmetal Transition in Metallic Oxide Films

Gaomin Wang
Louisiana State University and Agricultural and Mechanical College

THE ROLE OF DEFECTS IN THE METAL-NONMETAL TRANSITION IN METALLIC OXIDE FILMS

A Dissertation

Submitted to the Graduate Faculty of the
Louisiana State University and
Agricultural and Mechanical College
in partial fulfillment of the
requirements for the degree of
Doctor of Philosophy

in

The Department of Physics and Astronomy

by
Gaomin Wang
B.S., University of Science and Technology of China, 2009
August 2017

Acknowledgements

Upon the moment of completing this thesis, I was feeling quite complicated, to be honest. I had not quite believed that I could actually pull this off but yet here I am, and I have so many people to thank for the support they have given me along the way.

My first and most gratitude must go to my advisor, Professor Jiandi Zhang, who is one of the most supportive advisor and mentors I have ever met. Although I have been a disappointing student to him for all this time, Jiandi has never given up on me for a single moment and tried all he can to offer me financial support and the guidance along the road to my graduation. The past eight years has been a tough and confused chapter of my life filled with struggles and trials, self-doubt and self-denial. In my darkest hours, the thought of quitting had occurred to me more than once, including when I was writing this thesis; although there is no one to blame except myself, the frustration about how little I knew and how much I needed to learn was haunting me every minute and almost destroyed my momentum to move forward for quite a few times. However, during these times, it was always the thought that Jiandi had not given up on me despite how much I let him down that kept me going. I still remember that many years ago, Jiandi had told me firmly that persistence was the key to accomplishments; and now that I have completed this thesis which also marks the end of an important chapter in my life, I have finally come to understand how good it feels to be finishing something that I have started up a long time ago, despite all these years of struggle. Without Jiandi's support and guidance, I could definitely not have made it this far. I feel that in many ways, Jiandi is very much like my father: both of

them are honorable men with integrity, who values honesty, diligence and persistence; and I have and always will respect and look up to them.

I would like to thank all my current and previous committee members, Dr. E. Ward Plummer, Dr. Rongying Jin, Dr. Juana Moreno, Dr. Harris Wong, Dr. William Shelton and Dr. Catherine Deibel, who have given me a lot of help and academic advice. For a number of unfortunate reasons, some of them could no longer be on my defense committee, but I am equally grateful for all the kindness and support from them in the past.

I would also like to thank all the past and current members in our group. Many of them were already in the group when I first came here; and had offered me tremendous help as I picked up the basics skills for working in this field. The others have also done a lot for me not only through the collaboration on my projects, but also by maintaining a pleasant work environment. Apart from being my colleges, a lot of them are also my friends in private life. For the limitation on the length of this acknowledgement, I can only list the name of all these group members below instead of expressing my thanks to each of them here individually; nevertheless, I would still like to say the one and most important thing to them: eight years is too short to be working with you wonderful and intelligent people, and I hope that someday in the future, there would still be a chance that our life paths could intersect. My thanks go to all of you: Dr. Zhaoliang Liao, Dr. Yi Li, Dr. Junsoo Shin; Dr. Hangwen Guo, Dr. Zhen Wang, Dr. Lina Chen, Dr. Mohammad Saghayezhian, Meng Meng, David Howe, Prahald Siwakoti; Dr. Chen Chen, Dr. Fangyang Liu, Dr. Amar Karki, Jianneng Li, Dr. Zhenyu Diao, Dr. Jiayun Pan; Dr. Jisun Kim, Dr. Zhenyu

Zhang, Yifan Yang, Joel Taylor, Dr. Guixin Cao, Silu Huang, Roshan Nepal and Ramakanta Chapai.

One of the best things that have happened to me in the past eight years is that life has brought to me my best friend, Erica Xin Wu, who has given me endless support and encouragement through the completion of this thesis. Thank you for everything. You have helped me see the light in my darkest days and it is my privilege to have such a loyal and loving friend like you who would always understand me and stand by my side. Now that your life is also soon to start a new chapter, my most sincere wishes go to you and your family and I promise that I will always be there for you, just like you are always here for me.

I would also like to thank my therapist Amy, who had helped me get through the dark moments and regain confidence in myself. You are a good counselor and I know that you will do great working towards your PhD in Psychology. I offer you my best wishes for your future.

I would like to thank my father and mother. Not everyone can be as lucky as me to have such liberal, loving and supportive parents like you. Words fail me when I try to express how much love and gratitude I feel towards you, so please accept these simple words as my highest praise: I think you have done a really wonderful job raising me up. I am what I am today because of you. If I were to become a parent someday in the future, I would also like to become one like you.

Lastly, I would like to acknowledge the final support from U. S. National Science Foundation, which made the completion of this study possible.

Table of Contents

List of Tables

List of Figures

Abstract

Metal-nonmetal transition, or more specifically, metal-insulator transition (MIT) has been one of the most intriguing topics in condensed matter physics. Two theories describing fundamental driving mechanisms of MIT has been well-established over time: Mott-Hubbard theory and Anderson localization theory. The former mainly deals with contribution of electron interactions/correlations to the MIT, and the latter focuses on the role of disorder. However, it is an open topic how a system behaves when both effects exist in a system. This study mostly takes interest in a type of MIT induced by dimensionality-crossover in the transition metal oxides (TMOs) systems. TMO system is a perfect playground for studying the underlying mechanisms behind MIT due to wide presence of strong electron interactions in the d-band, and the existence of oxygen vacancies as an unavoidable form of disorder. The focus of this study is mainly on the role played by disorder. A metallic TMO system $SrVO_3$ (SVO) was chosen to perform the investigation due to its simple structure and lack of magnetic ordering. Well-ordered SVO thin films have been fabricated in a layer-by-layer fashion on crystalline $SrTiO_3$ (001) substrates. Surface structural characterization and morphology images suggest that the SVO films are of high quality with correct symmetry and atomically flat surfaces. The structural and chemical composition characterization indicates the existence of a significant amount of oxygen vacancies in the first three layers of the SVO films, coinciding with the critical thickness for the MIT, which has been confirmed by spectroscopic analysis which reveals zero density of states at the Fermi level for films with thickness below 3 unit cell (u.c.). Transport measurements reveal

weakly localized lnT behavior for metallic SVO films close to the critical thickness, agreeing with the picture of a 2D disordered correlated system. Negative magnetoresistance observed in the weakly localized films is consistent with the prediction that disorder dominates over correlation effects. Moreover, by deliberately introducing more disorder into metallic SVO films, MIT can also be induced. Through our research, we conclude that the disorder effect is the major driving mechanism for MIT.

Chapter 1. Introduction to Metal-Insulator Transition, Transition Metal Oxides and $SrVO_3$

1.1 Introduction

In this chapter, we describe the motivation of this study by reviewing the metal-insulator transition (MIT) and its possible driving mechanisms, following by the introduction of transition metal oxides (TMOs) systems. We will also review some important properties of the $SrVO_3$ system we are working on in the last section of this chapter. We hope that when we reach the end of this chapter, we would have justified our investigation in a good manner.

1.2 A Brief Introduction of Different Types of Metal-Insulator Transition

Metal-insulator transitions, as the name indicates, is the transition a system undergoes between metallic and insulating states. MIT is a widely observed phenomenon known to occur in many systems with various kinds of driving force like pressure, temperature and so on [1]. Being one of the most fundamental problems in condensed matter physics, MIT is also among the least understood. The study of the mechanism behind metal-insulator transition not only allows us to gain better understanding of the physics but also give us more control over the material and its engineering process which can potentially develop into devices that change every aspect of our daily life.

Based on the underlying mechanism, MITs can generally be divided into two large categories: the MITs caused by strong electron interactions/correlations, which is known as the Mott-Hubbard transition [2]; and the MITs caused by the existence of strong disorder, known as

Anderson transition [3]. In this section, we will give a general introduction of MIT and put a little more focus on Mott-Hubbard theory since it is closely related to the TMO system that we study. For Anderson transition and related theory, a detailed introduction will be given in Chapter 6.

1.2.1 Mott-Hubbard Transitions

In order to understand MIT, we have to refer back to the basic definition of metals and insulators. The first theory distinguishing a metal and an insulator was established by Bethe, Sommerfeld and Bloch in the late 1920s [4-6], with semiconductors added to the picture a few years later by Wilson [7-10]. The so–called band theory states that the distinction between metals and insulators can be understood based on the electronic band filling. If the Fermi level lies inside an electronic band, the system is metallic; while if the Fermi level lies in the bad gap, it can be either insulating or semiconducting depending on the size of the band gap. If the band gap is small enough that the electrons can cross over it under thermal excitation, the system will show some conductivity and will be semiconducting. A schematic picture of the band diagram is shown in Figure 1.1.

The band theory has been quite successful in describing the difference between metals and insulators. However, in this scenario, it is assumed that the band structures are formed entirely by the periodic crystal lattice and the electron interactions are completely ignored. When it comes to systems with strong electron correlations like transition-metal oxides, the model is no longer accurate. In 1937, de Boer and Evert Verwey stated that many transition-metal oxides such as

NiO with a partially filled d-band were also poor conductors or even insulators [11]. In the same year, Peierls pointed out that the strong Coulomb repulsion between electrons could be a critical

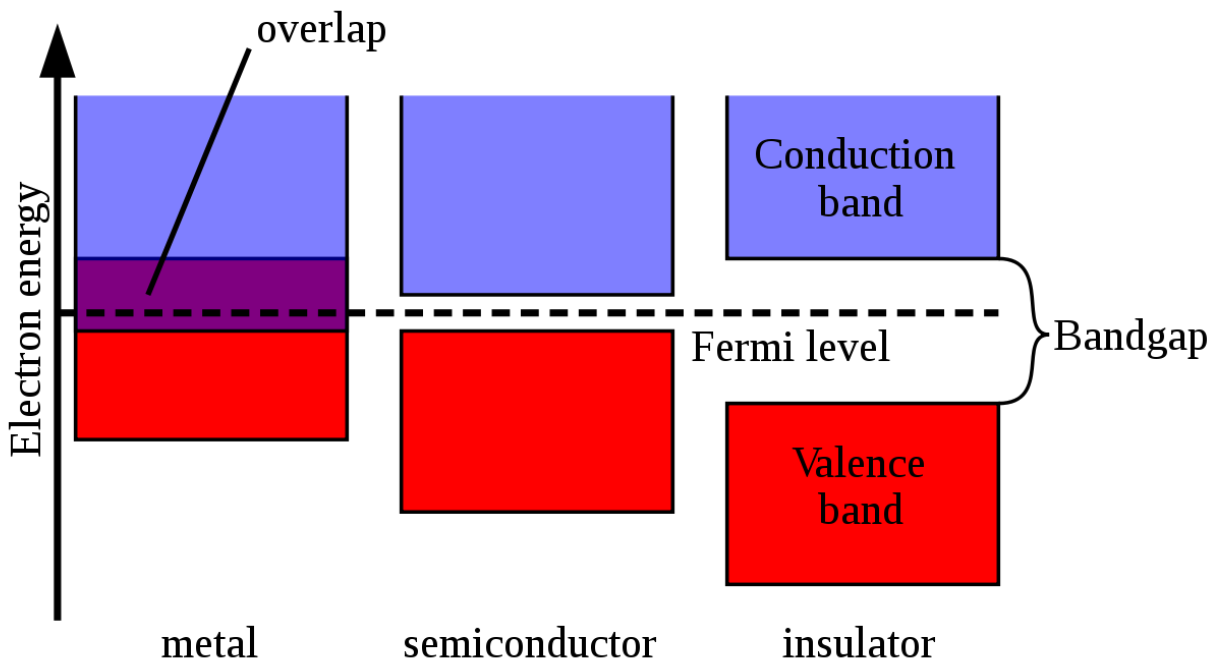

Figure 1.1. A schematic band diagram of metal, semiconductor and insulator based on the description of the band theory.

contributing factor of the observed insulating behavior in TMOs [12]. Since then, strong electron interactions as an important mechanism driving the MIT has been extensively studied by many scientists. The most famous among them is probably Sir Nevill Mott. In fact the insulating state resulted from strong electron interactions is named after him as Mott insulator. In the model proposed by Mott, in each site there exists an electronic orbital. In the absence of electron interactions, these orbitals overlap and form a single band which becomes full when two electrons with opposite spins occupy the same site. When the Coulomb repulsion is sufficiently strong, the band will split up into two separate bands called the lower and upper Hubbard band.

The lower Hubbard band is formed by electrons occupying empty sites, while the upper Hubbard band is formed by electrons occupying the sites that are already taken by another electron. When there is one electron per site, the lower Hubbard band will be full and the upper Hubbard band will be empty. The Fermi level lies in the band gap; therefore the system will be an insulator. In the d-electron systems, depending on the closeness between the d-band and the p-band, Mott insulators can be further classified into two categories: Mott-Hubbard insulators and charge-transfer insulators, as shown in Figure 1.2, which is taken from Ref. [1]. In this study, all our discussion is limited to d-electron systems, or to say, TMOs. We are going to give a more detailed introduction of TMO systems, in the next section.

In Mott picture, there are two important factors which have control over the MIT: the electron correlation strength U/t and the band filling n. The former determines the distance between the lower and upper band and the latter denotes the number of electrons per site. In the tradition band theory picture we introduced at the beginning of this section, the band insulator is formed by fully filled bands, corresponding to the n=0 or n=2 cases in Mott picture. When the d-band is half-filled, i.e. n=1, the change of electron correlation strength U/t tunes the splitting of the d-bands at some critical value U_c, MIT will be induced, which is called a bandwidth control (BC)-MIT. Apart from tuning the electron correlation strength, the MIT can also result from changing the filling n by doping extra carriers in a parent Mott insulator. In this case, the transition is called filling control (FC)-MIT. Another schematic diagram also taken from Ref. [1] showing these control parameters is presented in Figure 1.3.

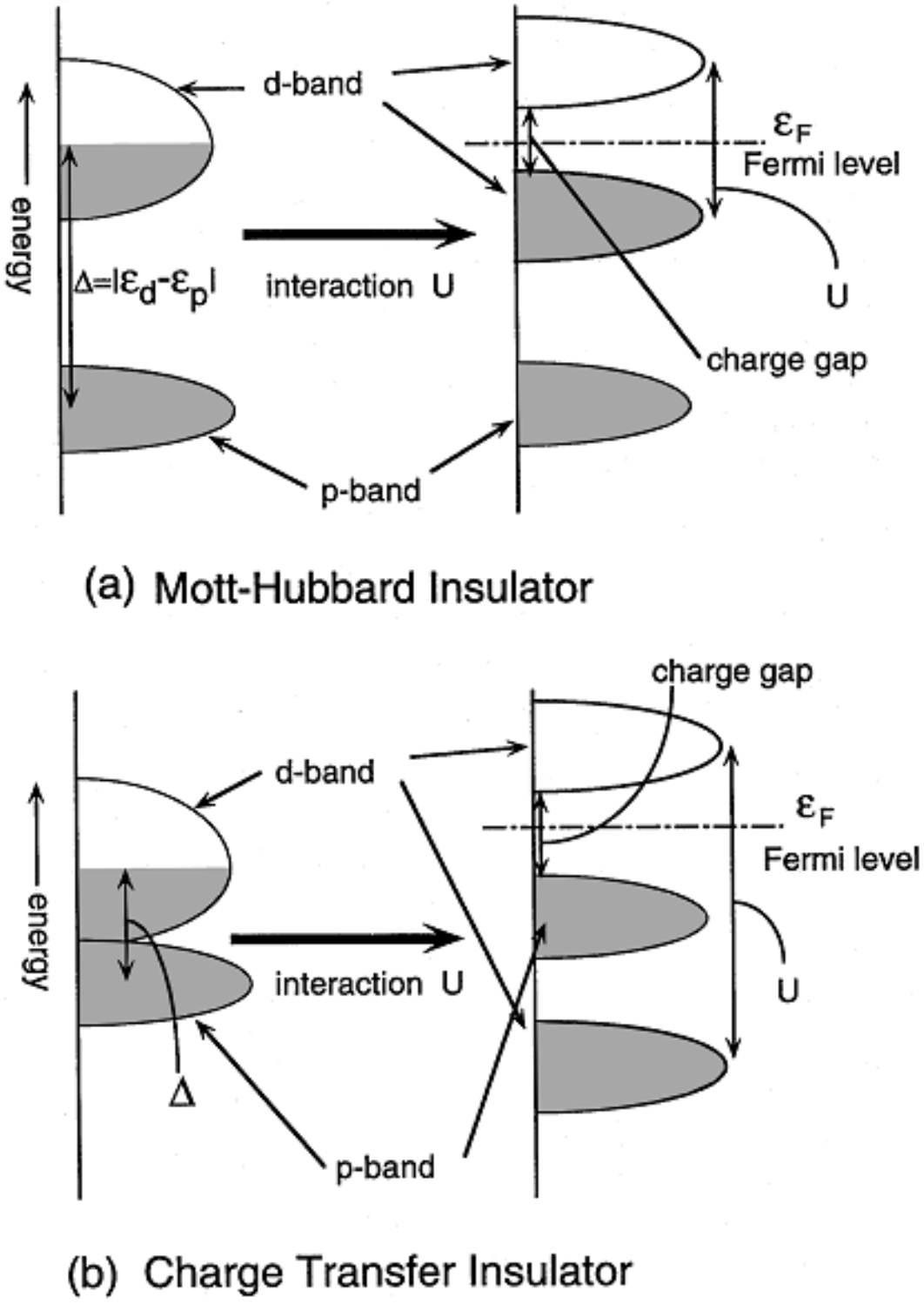

Figure 1.2. A schematic picture of the energy levels of two common types of Mott insulators [1]. (a) Mott-Hubbard insulator; (b) charge-transfer insulator.

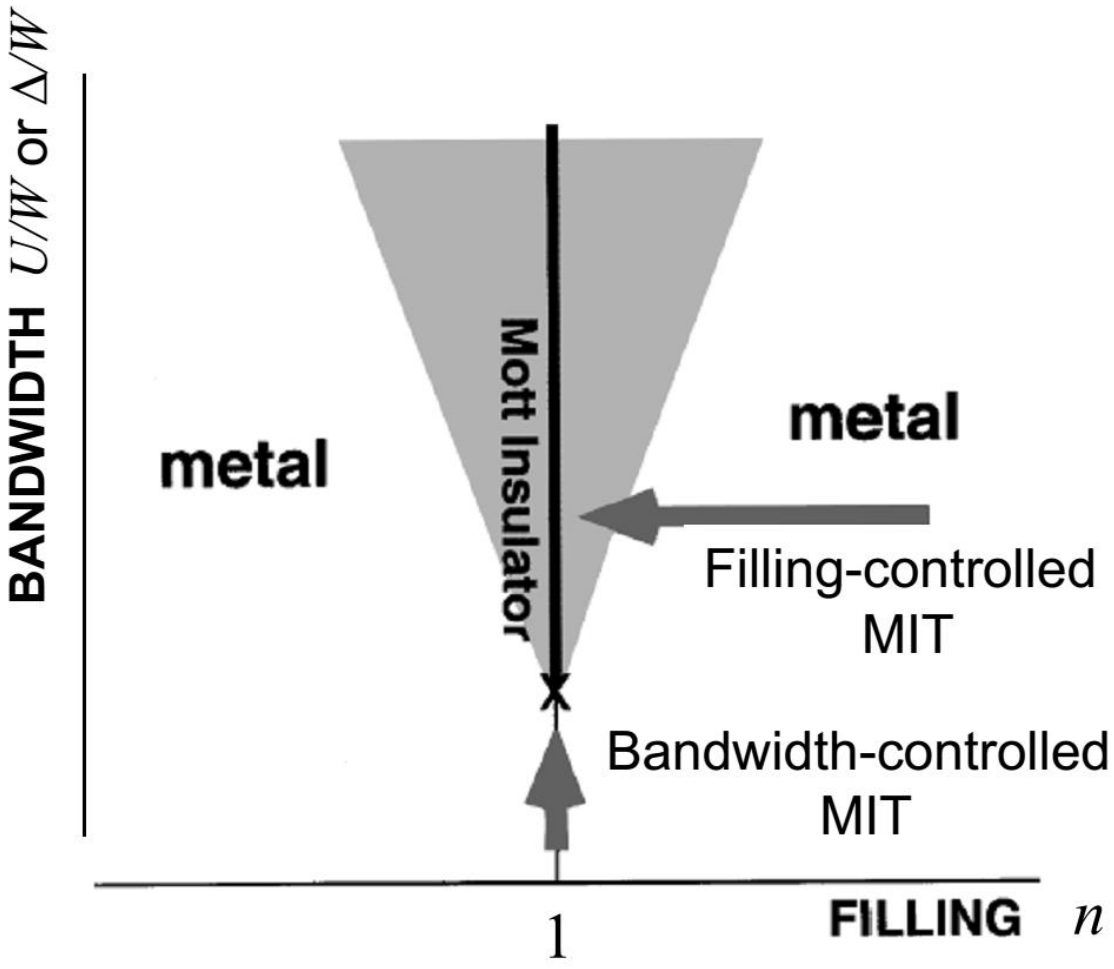

Figure 1.3. A schematic picture of the realization of Mott-type MIT with two routes shown: FC-MIT and BC-MIT [1].

1.2.2 Anderson Transitions

The discussion of the Mott-Hubbard type MIT in the previous section is based on the existence of strong electrons interactions in the system. However, if we also take the atomic lattice into account, we encounter another type of MIT which is the Anderson transition. To be more precise, Anderson transition is induced by the existence of strong disorder in a crystal lattice, defects, dislocation and off-stoichiometry, for example. The existence of the defects or

disorder introduces an additional random potential to the original periodic lattice potential and causes the Bloch waves to lose coherency. When the disorder is too strong that the random potential can no longer be treated as a perturbation, the electrons may be trapped in the local potential wells and become spatially localized, driving the system into the insulating state. We will not discuss more details of the theory regarding disorder-induced MIT here but in a separate chapter later. For now, the most important conclusion for us to bear in the mind is that both strong electron correlations and disorder has the capability of driving a system into the insulating state. This makes things especially interesting for transition metal oxides, where oxygen vacancies exist as a most common and unavoidable form of disorder and strong electron correlations also come into play in many TMO systems. The object of this study is to investigate the role of oxygen vacancies behind the MIT in a prototype TMO system $SrVO_3$. In the following section, we will give a brief introduction of the TMO and perovskites and justify the reason we choose $SrVO_3$ as the system for this study.

1.3 Transition Metal Oxides

Transition metal oxides (TMOs) have been one of the most-studied systems in condensed matter research for many decades. The narrow 3d band in TMOs often leads to electron correlations which not only give rise to MIT but also a variety of other interesting phenomena, such as high temperature superconductivity [13], and colossal magnetoresistance [14] and ferroelectricity [15]. Among the family of TMOs, perovskites have the simplest structure and are widely used in applications such as the making of catalyst electrodes in certain types of fuel cells

[16] and the manufacture of memory and spintronic devices [17]. In three-dimensional perovskite systems, the idea structure is cubic with an ABO_3 formula, with the A-cations located on the corners, and the B-cation, which is a transition metal element, in the center of the cubic structure. The oxygen atoms occupy the six face center position, and BO_6 octahedron is formed as shown in Figure. 1.4 [18]. Depending on the size of the ions and external conditions such as pressure and temperature, each octahedron may undergo shape-deformation, tilt, and rotation, and the whole system will deviate from a cubic structure to form an orthorhombic, tetragonal or rhombohedral structure [19]. One class of prototype structure distortions is Jahn-Teller distortion, which is usually caused by chemical doping, ionic size variation, etc. The octahedra may undergo an in-plane rotation and/or an out-of-plane tilt, as shown in Figure 1.5.

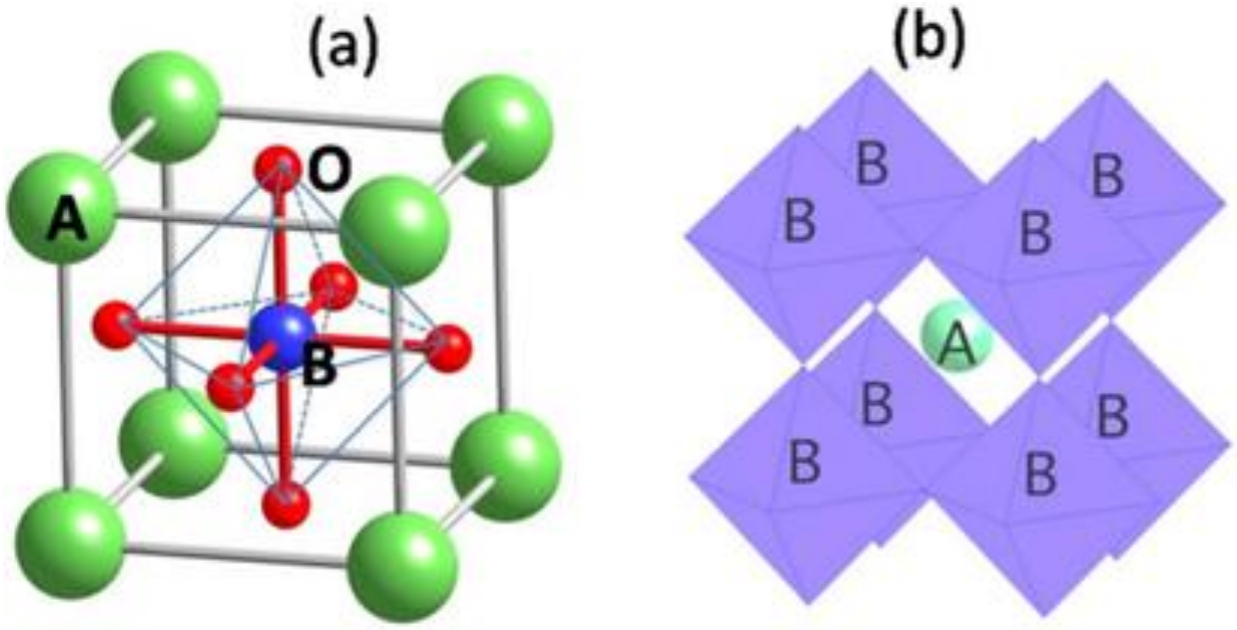

Figure 1.4. Structural model ABO_3 of cubic perovskite. (a) One single unit cell (u.c.). (b) A stack-up view.

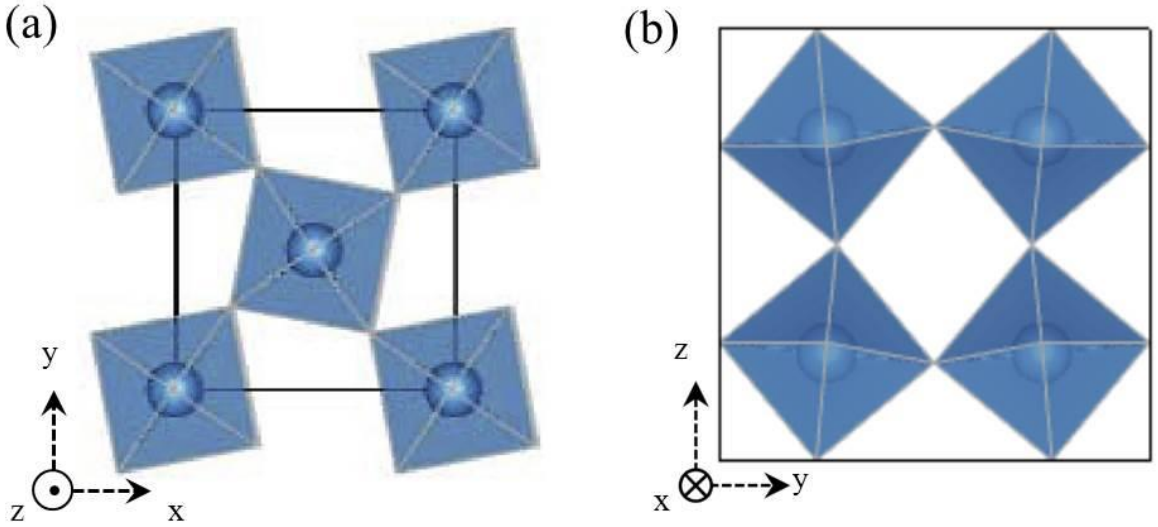

Figure 1.5. Jahn-Teller distortion in the perovskite system: (a) in-plane rotation [20] and (b) out-of-plane tilting of BO_6 octahedra.

In ideal cubic perovskites, the five d-orbitals of transition metal at the center of the octahedron are split into two categories: the doubly degenerate e_g orbitals with higher energy, $d_{x^2-y^2}$ and $d_{3z^2-r^2}$, which point toward the six oxygen ions located at the corners of octahedron; and the triply degenerate t_{2g} orbitals with lower energy, d_{xy}, d_{yz} and d_{zx}, which point between the oxygen ions, as shown in Figure 1.6. When Jahn-Teller structural distortion exists in the system, the degeneracies of the orbitals will be further lifted, causing the system to rest in a more stable state with lower energy. The electronic and magnetic properties of a perovskite system are determined by the d-electron configuration of the transition metal ion located at the B-site. In Figure 1.7, we illustrated the d-electron configurations of some typical perovskite systems. Among these system, $SrTiO_3$ (STO) and $LaMnO_3$ (LMO) are insulators and the rest are metals [1]. The insulating behavior of STO can be easily understood due to the lack of d-electron (d^0) such that it is a simple band insulator. As the number of d-electrons increase, the electrons

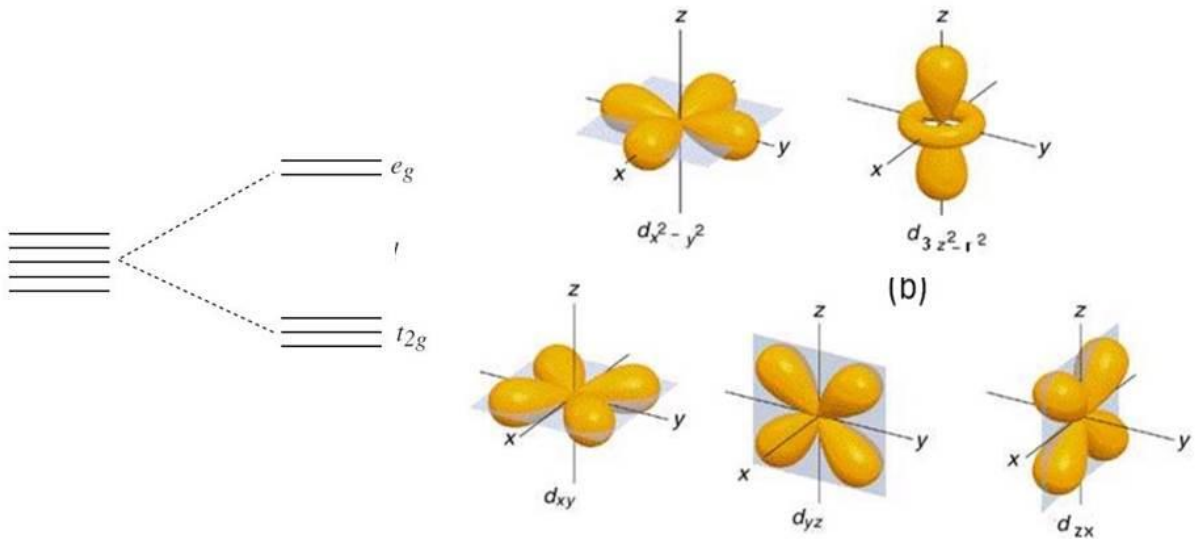

Figure 1.6. The splitting of d orbitals in perovskites.

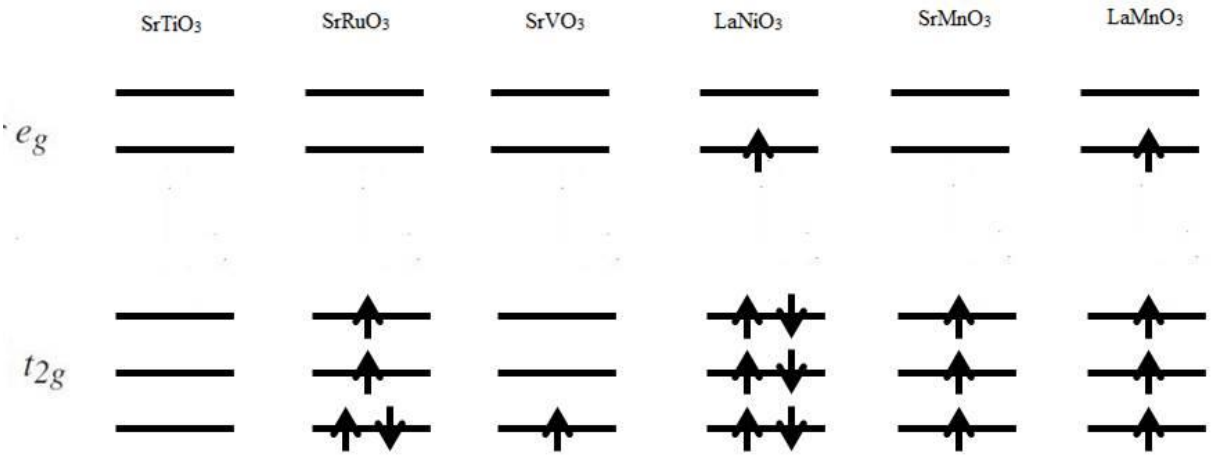

Figure 1.7. The d-electron configurations of the transition metal element in some typical perovskite systems.

tend to fill low-level t_{2g} orbitals first, allowing two electrons with opposite spins to occupy the same orbital, as in $SrVO_3$ (SVO), $SrMnO_3$ (SMO), $SrRuO_3$ (SRO) and $LaNiO_3$ (LNO). The LMO case is somewhat different due to the existence of a strong Hund's coupling that is larger than the energy gap of the e_g and t_{2g} orbitals. This results in a spin configuration in which all spins are aligned parallel with three electron occupying each of three t_{2g} orbitals and one electron

occupying one of the e_g orbitals. In the meantime, a strong Jahn-Teller distortion results in the further splitting of two e_g energy levels and finally makes the compound insulating.

As we stated above, the purpose of our project is to explore how oxygen vacancies as a type of disorder can drive the system into the insulating state. In order to achieve this, we have to choose a metallic system to start with; as we gradually introduce disorder into the system, the system will be driven towards insulating behavior. Also, to avoid the influences as much as possible from other driving forces such as lattice distortion and magnetic ordering, we would like to choose a system as simple as possible in both structure and properties to work with. Among all the systems mentioned above, SVO is the only metallic system with simple cubic structure and without magnetic ordering, which makes it a perfect candidate for theoretical understanding without the involvement of spin degree of freedom. In the following section, we will give a review of the properties of SVO and some similar TMOs.

1.4 Physical Properties of $SrVO_3$

The study of the SVO compound as a strong correlated metal has been continued for about thirty years since the photoemission spectroscopic analysis for SVO bulk in the 1980s. Recent reports of dimensionality crossover-driven MIT of SVO [21] has sparkled new interests in this system and since then there has been quite a few new findings proposing its promising application as transparent conductors [22], solid oxide fuel cell anodes [23], and epitaxial conducting electrode in oxide heterostructures [24-26]. In this section, we will give an introduction of the physical properties of SVO both in bulk and in thin films. Since the

mechanism behind dimensionality-driven MIT is the goal of our study, we will also review some similar effects reported in other TMO systems.

1.4.1 Bulk Properties

The $SrVO_3$ bulk is a strong correlated paramagnetic metal across all-temperature range [27]. When SVO is doped with Ca, the valence of vanadium remains unchanged and system remains metallic across all doping levels in bulk, but the V-O-V bond angle will gradually decreases from 180° to 160° , with leads to a decrease in the one electron d-bandwith [27]. On the other hand, doping with La introduces an extra d-electron into the SVO system along with some magnetic ordering, and MIT will be induced upon a certain doping level. Figure 1.8, displays several

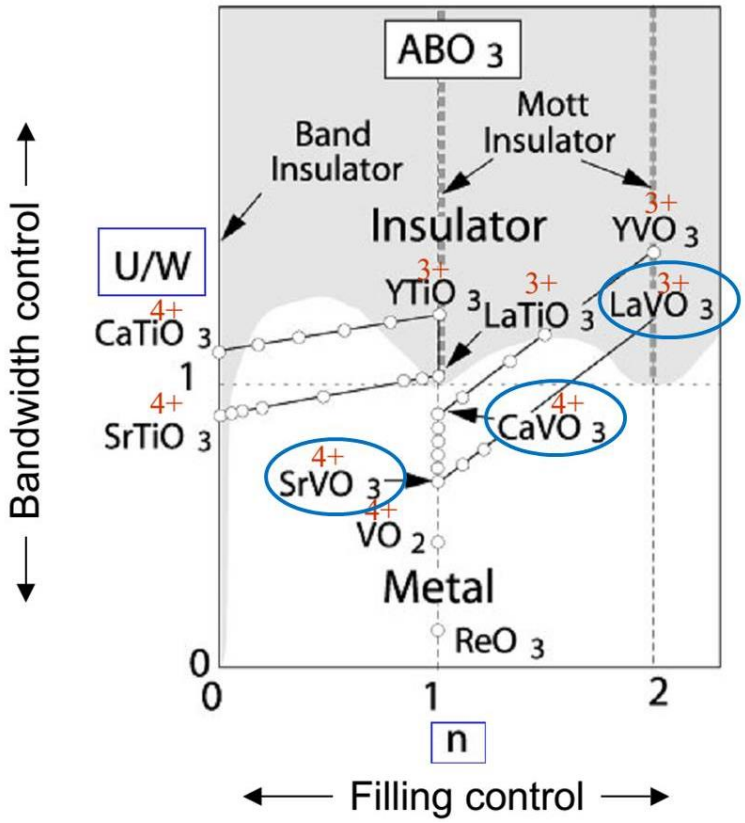

Figure 1.8. Some typical Mott-Hubbard systems with SVO and related vanadates circled out.

typical Mott-Hubbard systems, including SVO and related vanadates. A phase diagram depicting filling-control MIT in the $La_{1-x}Sr_xVO_3$ (LSVO) system is shown in Figure 1.9 (a), with the single crystal transport data upon doping level shown in Figure 1.9 (b) clearly showing the MIT [28].

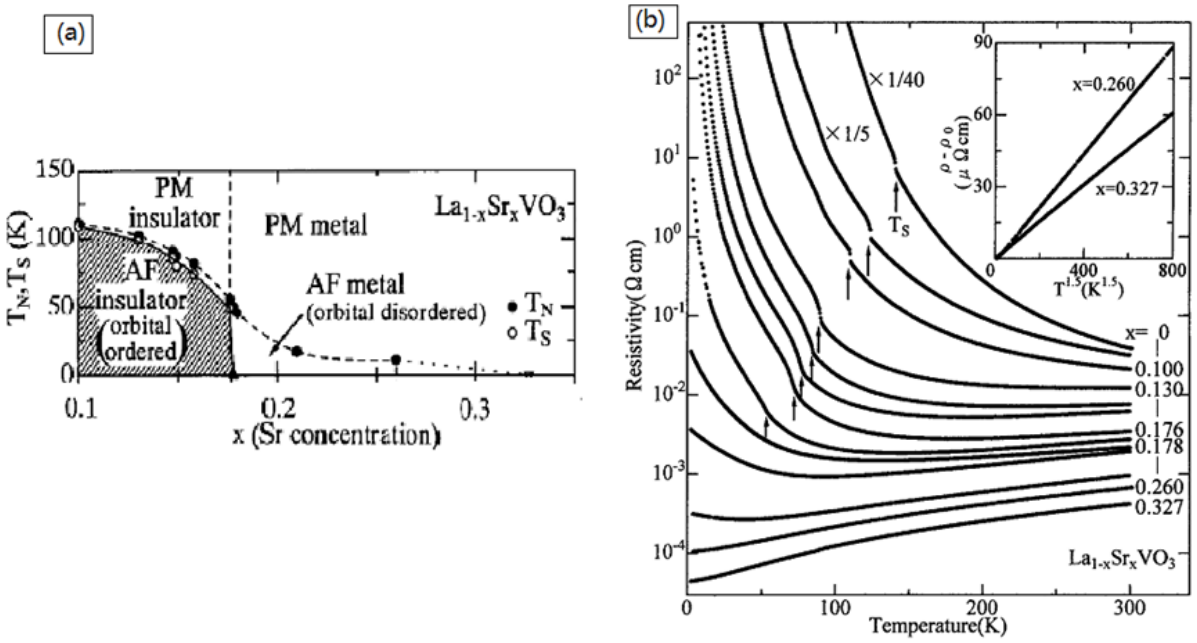

Figure 1.9. (a) The electronic phase diagram of $La_{1-x}Sr_xVO_3$ upon Sr concentration. (b) Temperature-dependent resistivity for single crystals of $La_{1-x}Sr_xVO_3$ with different Sr concentration [28].

The electronic structures of SVO have been intensively studied by both theoretical calculations and experimental spectroscopic investigation. The three t_{2g} bands in SVO are almost degenerate due to the perfect cubic structure. Band-structure calculations predicts that the weak hybridization between the d_{xy}, d_{yz} and d_{zx} orbitals will form three two-dimensional penetrating cylindrical sheets of Fermi surface, as shown in Figure 1.10 (a) [29]. Fermi surface mapping by ARPES done by Yoshida et.al confirms the above results (Figure 1.10 (b)) [30]. In their paper, Yoshida reported a coherent band with clear dispersive features at ~0.5 eV below E_F, while LDA

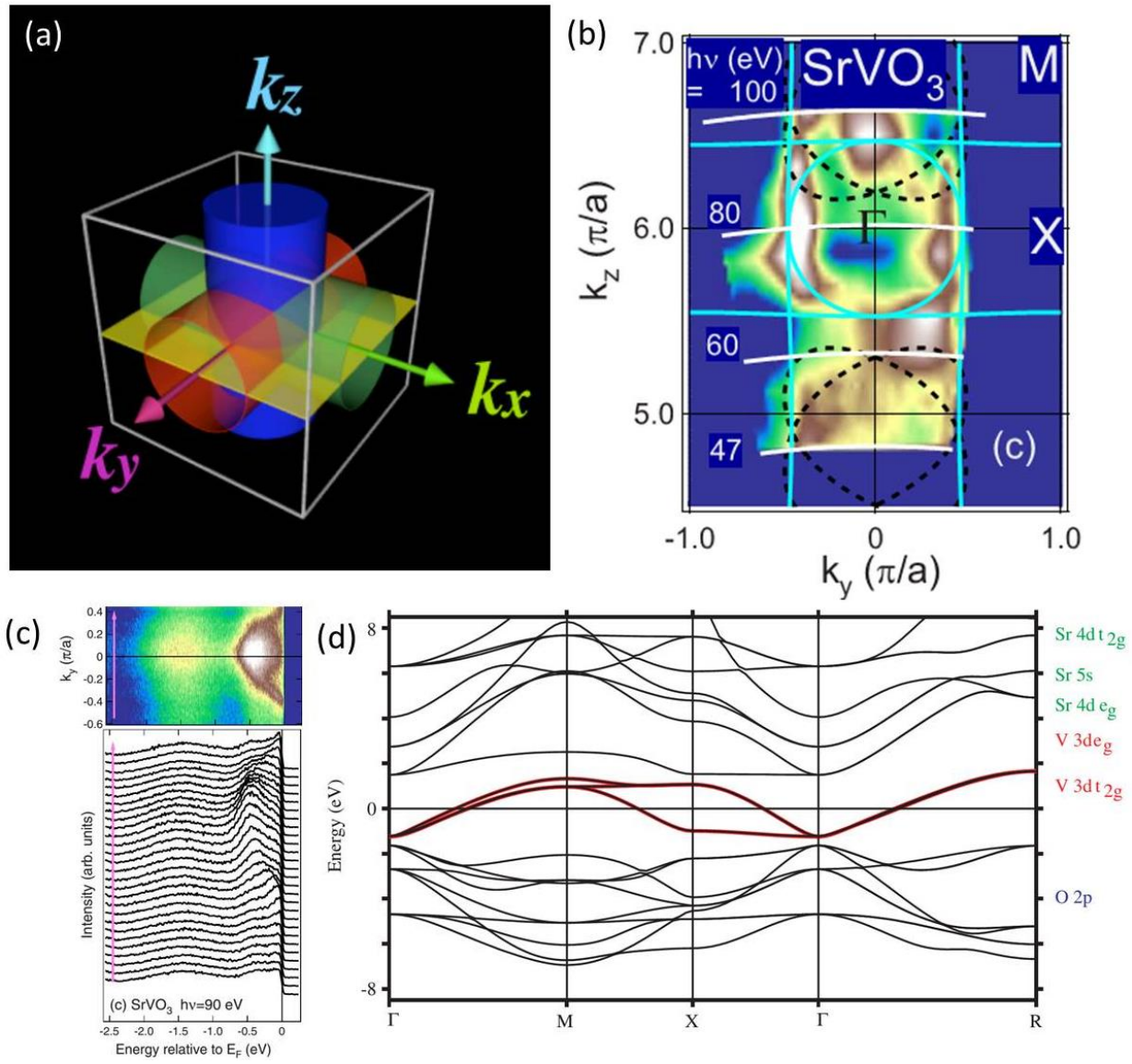

Figure 1.10. (a) Fermi surface of SVO bulk [29] (b) Fermi surface mapping of SVO single crystal by ARPES with comparison from theoretical calculations marked as blue lines. [30] (c) ARPES spectra of SVO displaying the dispersive coherent band [30] (d) Band structures calculated by LDA [31].

calculations predicts the value to be about twice (Figure 1.10 (c)-(d)) [31], indicating an electron mass renormalization with a factor of~2 due to the strong electron correlations which is also predicted from the electronic specific heat coefficient measurements done by Inoue *et. al.* in the

early days [27]. In a simple picture, we can understand SVO as a Fermi liquid with an enhanced effective mass.

1.4.2 Properties of $SrVO_3$ Thin Films

The reduction of dimensionality often causes the emergence of interestingly different properties in many materials and SVO is no exception. Yoshimatsu et al. reported the existence of quantum well (QW) states observed by ARPES in $SrVO_3$ ultrathin films grown on $SrTiO_3$ (001) substrate with thickness below 10 u.c. [29]. The formation of the quantum states can be easily understood by considering the electrons trapped in potential well, with its edges served by the interface between the film and the substrate and the surface of the film. When the film thickness decreases to a critical value of 2-3 u.c., the film is no longer metallic and a band gap is finally formed at a thickness 1 u.c., which is also reported by Yoshimatsu et al in another paper [21]. In Figure 1.11 and Figure 1.12, we present these important findings from their original source.

This MIT induced by reducing the dimensionality is what sparks the interest of our study. As we discussed before, two major fundamental driving forces for MIT are electron interactions and disorder. We have also shown in the last section that SVO is indeed a system with strong electron correlations, so naturally, the question come to our mind that whether electron correlations is responsible for this MIT, as proposed by Yoshimatsu *et. al.* in the reference we mentioned above and subsequently investigated by theoretical calculations. In this study, we would like to take another point of view and investigate the MIT from the role of disorder, or

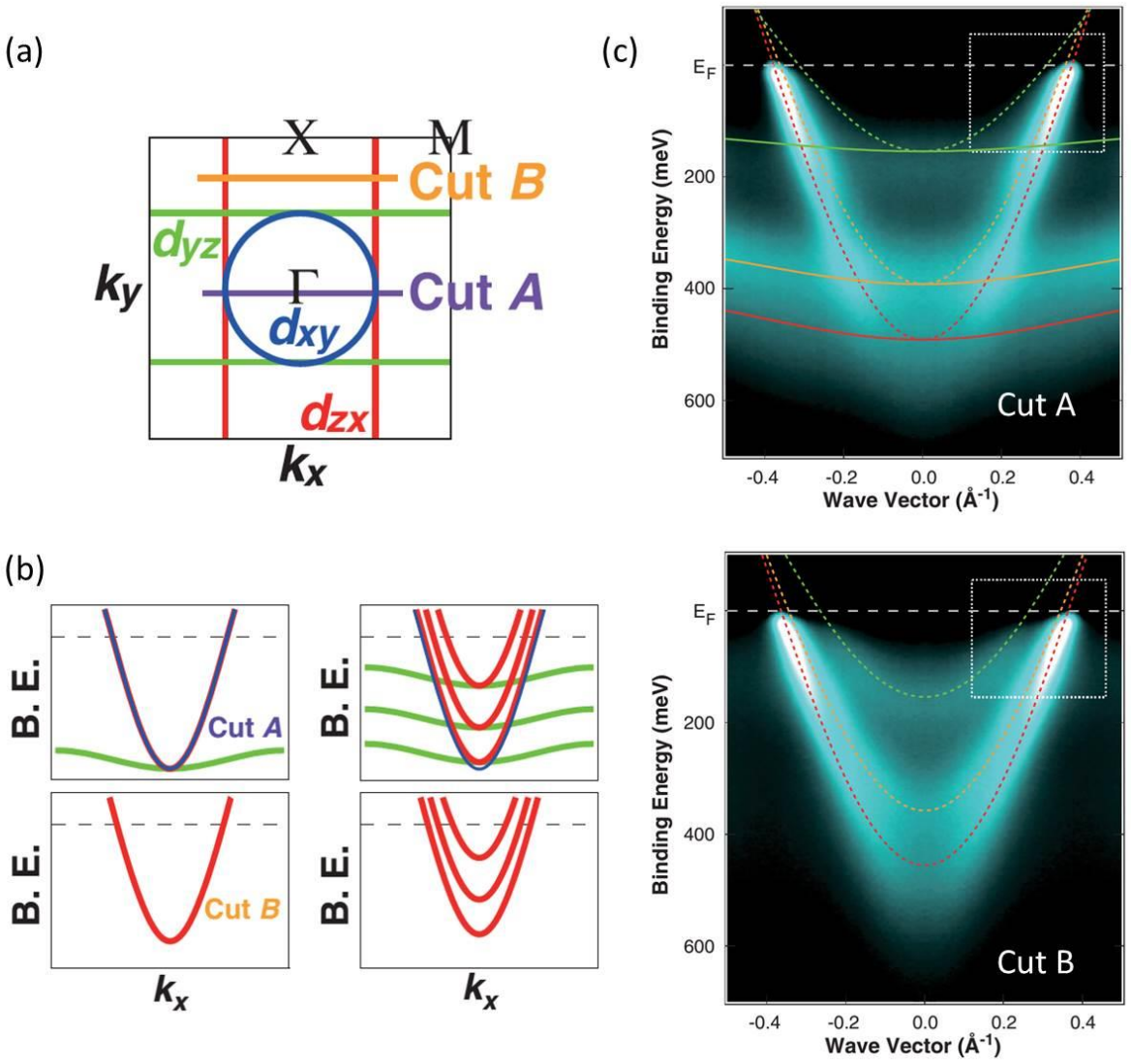

Figure 1.11. Quantum wells observed in SVO ultrathin films by ARPES [29] (a) The cross sections of Fermi surfaces in the k_z=0 plane. (b) The predicted band dispersions and quantization states along the two cuts illustrated in (a). (c) The observed quantum states by ARPES.

oxygen vacancies, to be specific. It should be noted that the dimensionality-crossover MIT is not unique for SVO but also has been observed in other TMOs where disorder has been proposed as the driving force, thus it is somewhat natural for us to speculate that this is perhaps more universal. In the following section, we will review two such examples which can hopefully help to justify our study.

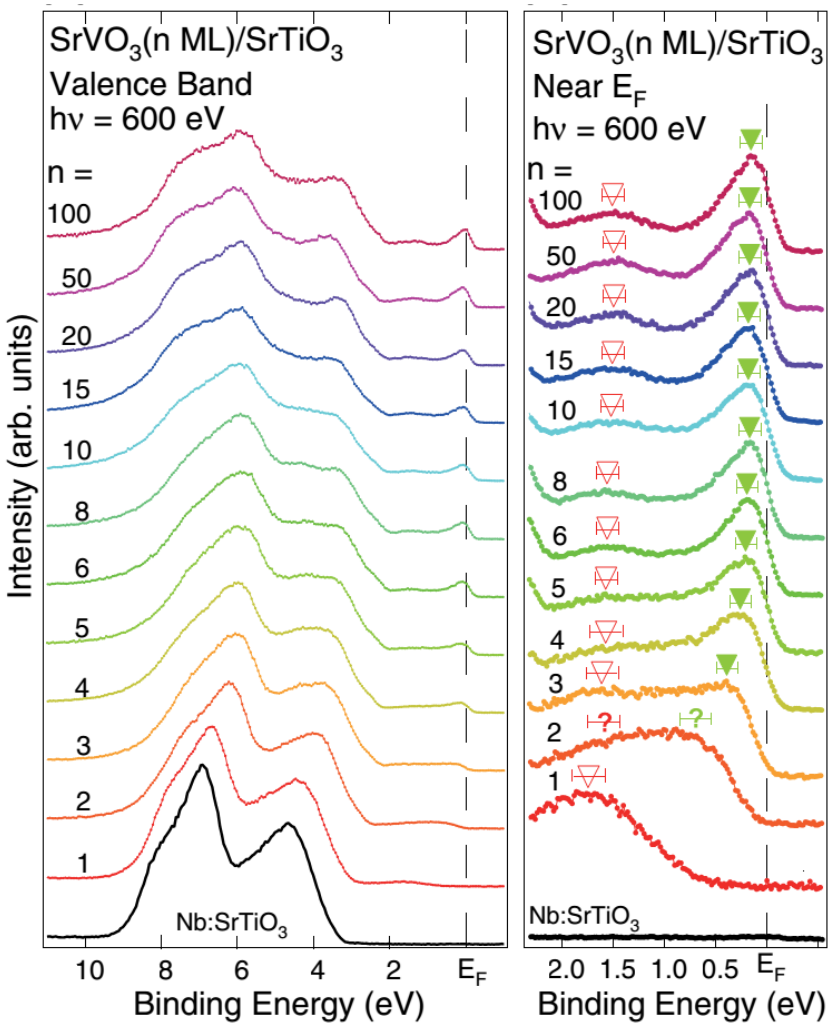

Figure 1.12. Thickness driven MIT in SVO thin films by PES spectra [21]. The evolution of a band gap is clearly visible as the film thickness decrease down to 1 u.c..

1.4.3 Dimensionality Properties of $SrVO_3$ Thin Films

In this section, we will review some of the experimental transport data showing the MIT for LNO and LSMO thin films with similar dimensionality effect.

In a paper by R. Scherwitzl *et. al.* thickness-driven MIT was reported in the ultrathin $LaNiO_3$ films grown on $SrTiO_3$ (001) substrates [32], as displayed in Figure 1.13. The transport data clearly shows an MIT at a critical thickness of 5 u.c., while just above the transition, the

upturn

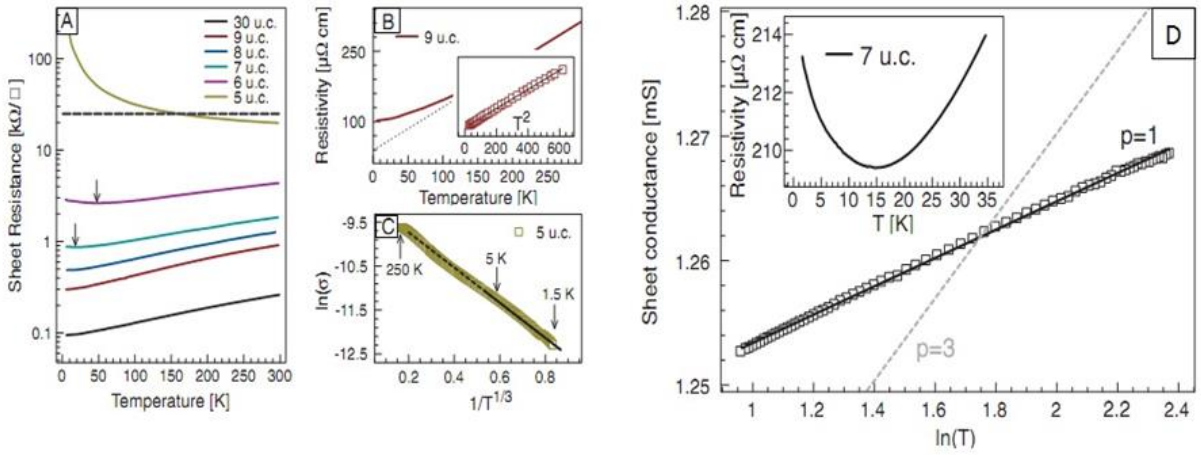

Figure 1.13. Transport properties of thicknesses for $LaNiO_3$ films grown on $SrTiO_3$ (001) substrates. (a) Sheet resistance versus temperature for different film. Arrows mark the temperatures where upturns in the sheet resistance occur. (b) Resistivity versus temperature for a metallic 9 u.c. film. The dotted line is an extrapolation of the high temperature linear behavior. The inset shows the resistivity versus T^2 for temperatures below 25 K. (c) Logarithm of conductance as a function of $1/T^{1/3}$ for a 5 u.c. film for temperatures from 1.5 to 250 K. The black line is the linear fit to the data between 1.5 and 5 K. (d) Sheet conductance versus the logarithm of temperature for a 7 u.c. film with a linear fit to the data (black line).The inset shows the resistivity of the same sample on a linear scale [32].

of the resistance curve begin to show up in the low temperature regime while maintaining metallicity at high temperatures, which seems to fit in the weak localization picture described by Anderson's MIT theory, i.e. the localization theory. The transport data in the fully-metallic regime (9 u.c.) was fitted with T^2, indicating Fermi-liquid behavior. The data in the insulating regime (5 u.c.) is well fitted to the variable range hopping (VRH) model which behaves like $\sigma = C\exp[-(T_0 / T)^{\alpha}]$, where σ is the sheet conductance, T is temperature, T_0 and C are constants and $\alpha = \frac{1}{d+1}$ for a d-dimensional system [33]. In the regime between the two limits of metal and insulator, the data is fitted to lnT. The good fitting results are consistent with the

description of strong and weak localization from Anderson's theory, which we will introduce in more details in Chapter 6.

A similar set of LSMO data from our group is displayed in Figure 1.14 below [34]. The

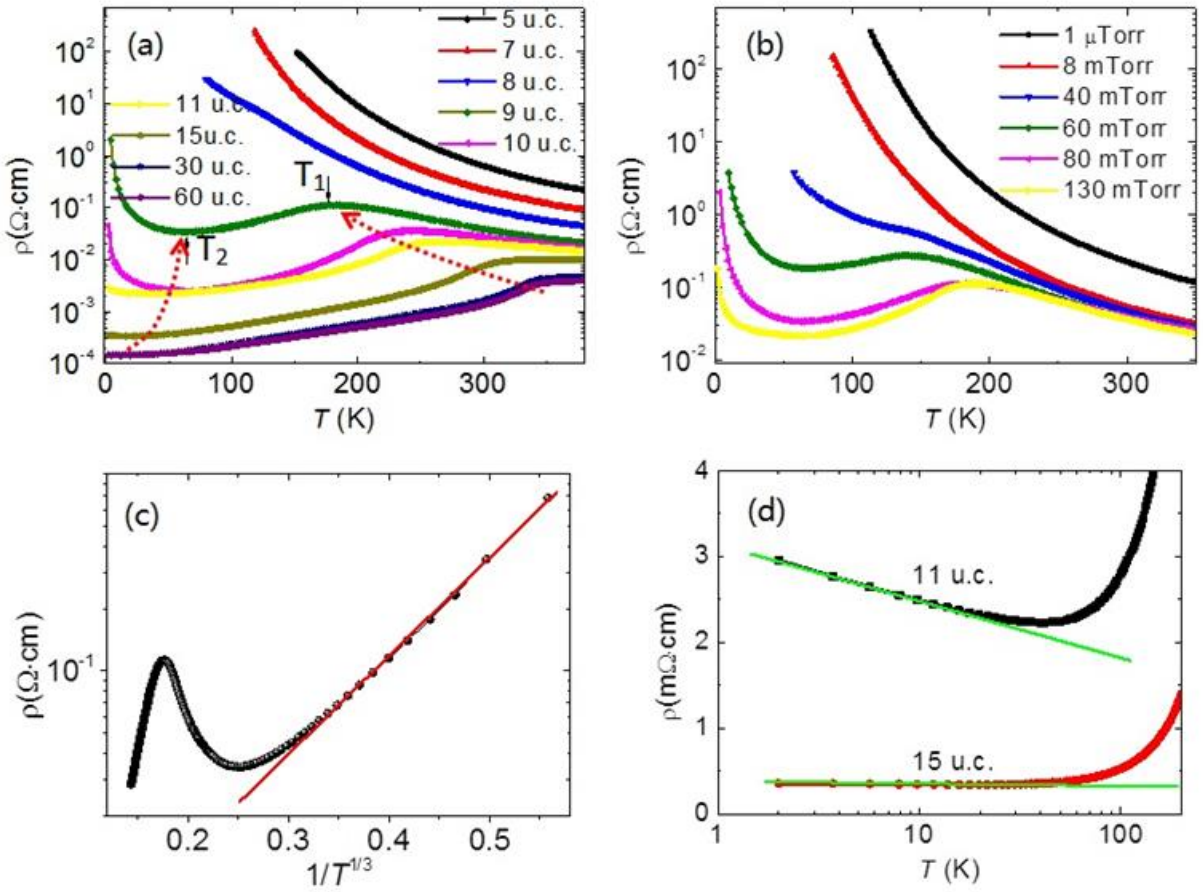

Figure 1.14. Transport properties of $La_{0.7}Sr_{0.3}MnO_3$ thin films grown on $SrTiO_3$ (110) substrates. (a) Temperature dependence of resistivity for films of difference thicknesses; T_1 and T_2 are defined as transition temperatures when the derivative of the resistivity curves cross over zero. (b) Temperature dependence of resistivity for 9 u.c. films grown under different oxygen partial pressure. (c) Fitting of the resistivity curve to $1/T^{1/3}$ for a 9 u.c. film grown at 80 mTorr. (d) Fitting of the resistivity curve to lnT for 11 u.c. and 15 u.c. films grown at 80 mTorr [34].

films are grown on SrTiO3 (110), and the substrate surface in this case is rectangular instead of cubic. Similar dimensionality effect with a critical thickness of 8 u.c. is observed in this case

(Figure 1.14 (a)). The T_1 and T_2 in the graph are defined by the transition points where the temperature derivative of the resistivity curves cross zero. As the thickness decreases, T_1 and T_2 are pushed closer until they vanish at the critical thickness. Interestingly, a very similar pattern of MIT has been observed in films with the same thickness but grown under different oxygen partial pressure, or to say, films with different levels of oxygen vacancies, as shown in Figure 1.14 (b). The film thickness is 9 u.c. for all films displayed in this panel, which is very close to the transition thickness and possess the best chance to cross to a different regime with slight tuning of parameters. In Figure 1.14 (c) and (d), similar fitting results of the transport curves of films in the different regimes are illustrated, which again fit well with the prediction from the localization theory.

The results from LNO and LSMO systems discussed above helps to support our speculation that disorder may be an important mechanism for the observed thickness-driven MIT. If this is the case, similar behavior in the SVO system can be expected. Indeed, in our study, we have shown that oxygen vacancies are capable of driving the SVO thin films to insulating. In the next five chapters, we plan elaborate on different aspects and characterize the SVO films in a systematic fashion to support our theory.

1.5 Summary

We have given a brief introduction of the two important driving forces for the MIT, electron-interactions and disorder. We are interested in the underlying mechanism of the dimensionality-crossover induced MIT and have chosen a strong correlated metal TMO, SVO, as

the system to perform our study due to its simplicity in structure and the absence of strong magnetic moments. In some other TMOs, similar MIT are observed with dimensionality decrease, and also by the tuning of oxygen content. We therefore make the bold assumption that oxygen vacancy as a most common type of disorder must have played an important role in the MIT in SVO, which concludes the motivation for this study.

Chapter 2. Instrumentation

2.1 Introduction

The main focus for our project is to study the role of disorder in the metal-nonmetal transition by investigating the structural and electronic properties of the SVO films. In order to achieve this, various experimental techniques will be applied, both in-situ and ex-situ.

The in-situ measurements are performed in an integrated ultra-high vacuum (UHV) chamber system displayed below (Figure. 2.1 (a)). The system is divided into two main parts: growth chamber and the analysis chamber. Films are deposited in the growth chamber by Laser Molecular Beam Epitaxy (Laser-MBE) and monitored real-time by Reflection High Energy Electron Diffraction (RHEED) for the film quality; then they are transferred into the analysis chamber for in-situ characterization without exposing the samples to the air, which guarantees the cleanness and offers the beast protection for the sample surface. The analysis chamber features various characterization tools including Low Energy Electron Diffraction (LEED), monochromated X-ray Photoelectron Spectroscopy (XPS), Ultraviolet Photoemission Spectroscopy (UPS)/Angle-Resolved Photoemission Spectroscopy (ARPES) and Scanning Tunneling Microscopy (STM). The manipulator in analysis chamber is Liquid Nitrogen (LN) and Liquid Helium (LH) capable which makes low-temperature analysis possible. The whole integrated system allows us to explore the physical properties and new functionalities at the surfaces and interfaces which we are interested in.

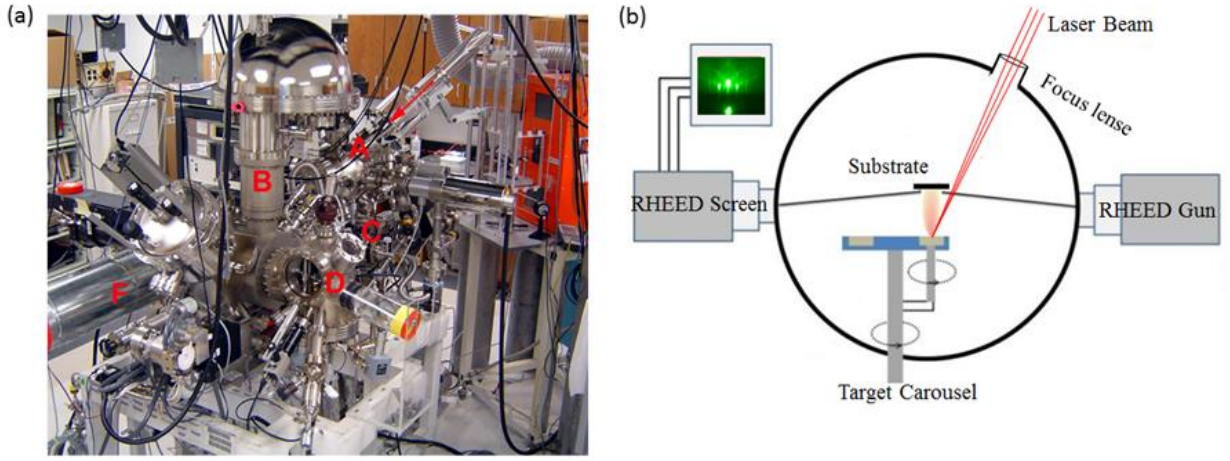

Figure 2.1. (a) Our integrated Laser-MBE and in-situ characterization system: (A) *In-situ* LMBE; (B) Small-spot monochromated ARXPS/ARPES; (C) Crystal cleaving setup; (D) STM/AFM; and (F) LEED setup. (b) Schematic diagram of Laser-MBE setup.

The ex-situ characterization in this project mainly consists of structural investigation by Scanning Transmission Electron Microscopy (STEM)/ Electron Energy Loss Spectroscopy (EELS) and transport and magnetoresistance (MR) measurements done by Physical Property Measurement System (PPMS).

2.2 Film growth

2.2.1 Laser Molecular Beam Epitaxy (Laser-MBE)

Pulsed laser deposition (PLD) is a thin film deposition technique. By focusing a high-power pulsed laser beam to ablate a target of the material that is to be deposited, the material is vaporized into the form of a plasma plume and is thus deposited on a substrate facing the target. The term “Laser-MBE” was introduced to describe a PLD system in which layer-by-layer growth is achieved and monitored by reflection high energy electron diffraction (RHEED). A typical set-up for Laser-MBE is shown in Fig. 2.1(b).

The major advantage of Laser-MBE is that the process is far from thermal equilibrium and, therefore, preserves complex stoichiometry. Today, PLD has been widely used in the film growth of high-temperature cuprates and other complex oxides. By monitoring the intensity of RHEED oscillations, one is able to control the growth of thin films at an atomic layer level, which is stated in the following section.

During growth, there are many experimental parameters that can be tuned to control the film qualities. First, the laser parameters such as laser energy, wavelength, pulse duration and repetition rate can be altered. Second, the preparation conditions, including substrate temperature, background gas and pressure, may be varied.

Our Laser-MBE system is based on the KrF excimer laser (COMPEx201) from Lambda Physik Company which produces the 248nm laser with pulse duration of 25 ns, maximum pulse energy of 700 mJ and maximum frequency of 10Hz. In the growth chamber, the base pressure is usually kept at a UHV level of 10^{-10} to 10^{-9} Torr and growth pressure up to 0.1 Torr can be achieved by inflating gas into the chamber, depending on the condition we need for the growth. The targets are mounted on the target carousel which can hold six targets, and we can change them in-situ without opening chamber, which makes it very convenient for the deposition of different materials on the same substrates. The distance between the target and the substrate is 4cm. The RHEED allows monitoring the growth pattern in real time.

2.2.2 Reflection High Energy Electron Diffraction (RHEED)

Reflection High Energy Electron Diffraction (RHEED) is a surface sensitive technique to probe surface topography, and can be used as a monitor during film growth. The RHEED setup is schematically shown in Figure 2.2 (a). A high energy electron beam is shot at the sample at a grazing angle θ (in our system $\theta \sim 2.5^0$), and reflected onto a phosphor screen. The diffraction pattern is recorded by a charge-coupled device (CCD) camera. The grazing angle of electron beam ensures the surface sensitivity of the technique. The diffraction pattern strongly depends not only on the surface symmetry but also the surface topography. The relation between surface topography and RHEED pattern is shown in Figure 2.2 (b).

By recording the time evolution of intensities of the diffraction spots, one is able to monitor

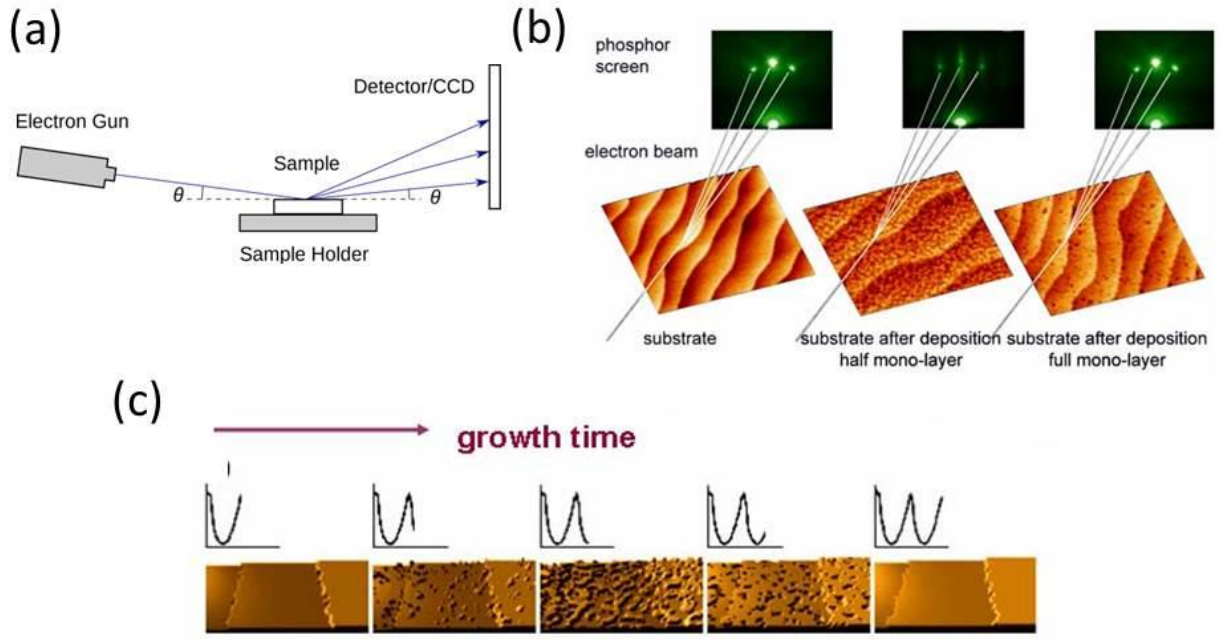

Figure 2.2. (a) Schematic diagram of RHEED. (b) RHEED patterns and AFM images during growth of one unit cell layer. (c) Ideal layer by layer film growth [35].

the film flatness. As shown in Figure 2.2 (b), when the substrate is covered by a complete monolayer, the intensities are the strongest. With the formation of incomplete monolayer as the film is deposited, the intensities decrease, and spots will evolve into streaks. When the new monolayer is completed, the intensities become strong and spots again come into shape. One period represents one complete monolayer. Thus by counting the number of the intensity oscillations, one can easily know how many unit cells have been deposited.

The RHEED in our system provides electron beam with energy of 35 keV. In Figure 2.3, the mean free path of electron is about 25 Å. The angle of incidence is about 2.5 degrees. At these grazing angles the penetration depth is about 1 Å, which is as small as one atomic layer, which makes RHEED a surface sensitive diffraction technique.

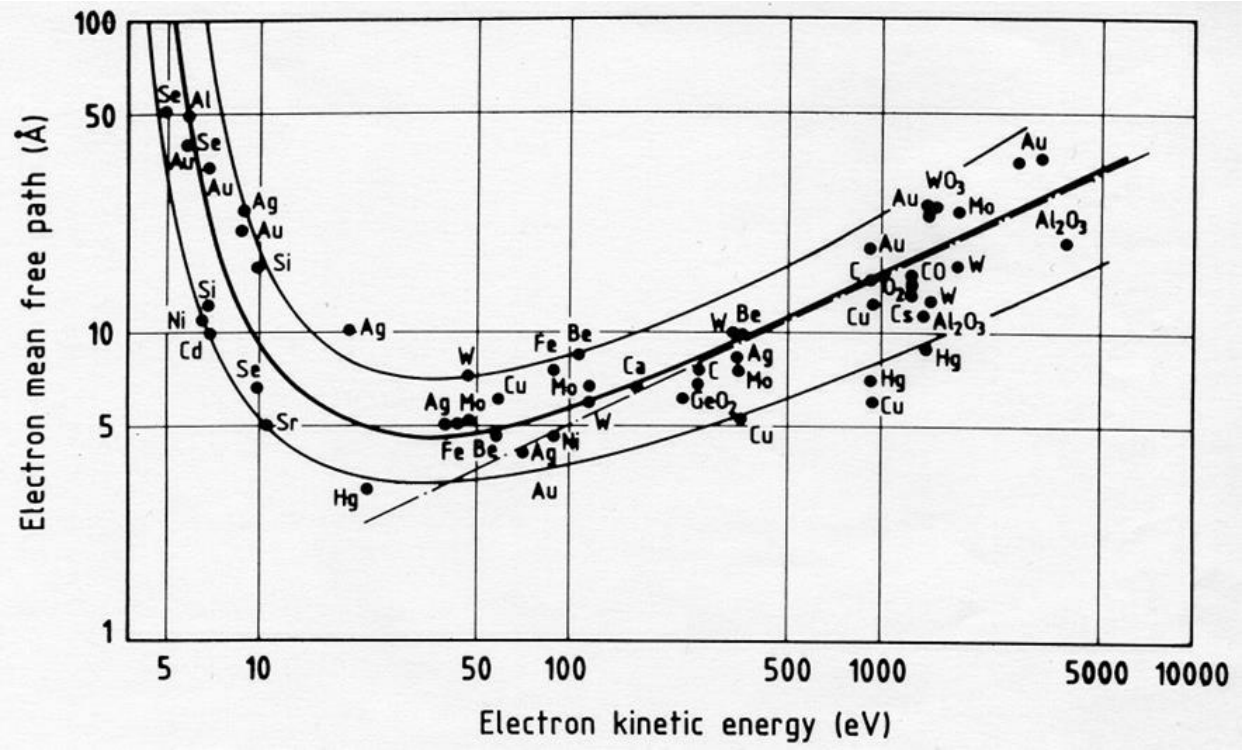

Figure 2.3. Mean free path of electrons in solids as a function of their kinetic energy.

2.3 In-situ Characterization

2.3.1 Low energy electron diffraction (LEED)

LEED is a surface sensitive technique for the determination of the surface structure of crystalline materials by shooting a collimated beam of low energy electrons (20-600eV) to the sample surface and observing the diffracted pattern on a fluorescent screen, as shown in Figure 2.4 (a). For electrons within this energy range, the wavelength is comparable or shorter than the crystal lattice constant, which means that the interaction between the electrons and the crystal is especially strong. The electron penetration depth is in the range of 10Å, a thickness of 1~2 unit cell in most of the materials, which makes LEED extremely surface sensitive.

LEED can be used in both qualitative and quantitative ways. Qualitatively the diffraction pattern can be analyzed to get information on the symmetry of surface structure. Figure 2.4 (b) is the LEED pattern of parent $SrTiO_3$, where surface has a 1×1 pattern.

Quantitatively the intensities of diffracted spots can be recorded as a function of incident electron beam energy to generate the so-called I-V curves. By comparing them with theoretical calculations, we may obtain accurate information of atomic positions or lattice structure in the proximity of surface, which is referred as LEED I-V structural refinement.

More specifically, the first thing we need to do when doing LEED I-V analysis is to set up a model surface structure, which should be chosen to be consistent with the symmetry of the LEED pattern. Calculations are them done by applying multiple-scattering theory to produce theoretical I-V curves, which are compared to the experimental results. The surface structure is

finally determined by how well the two sets of curves match with each other. The so-called

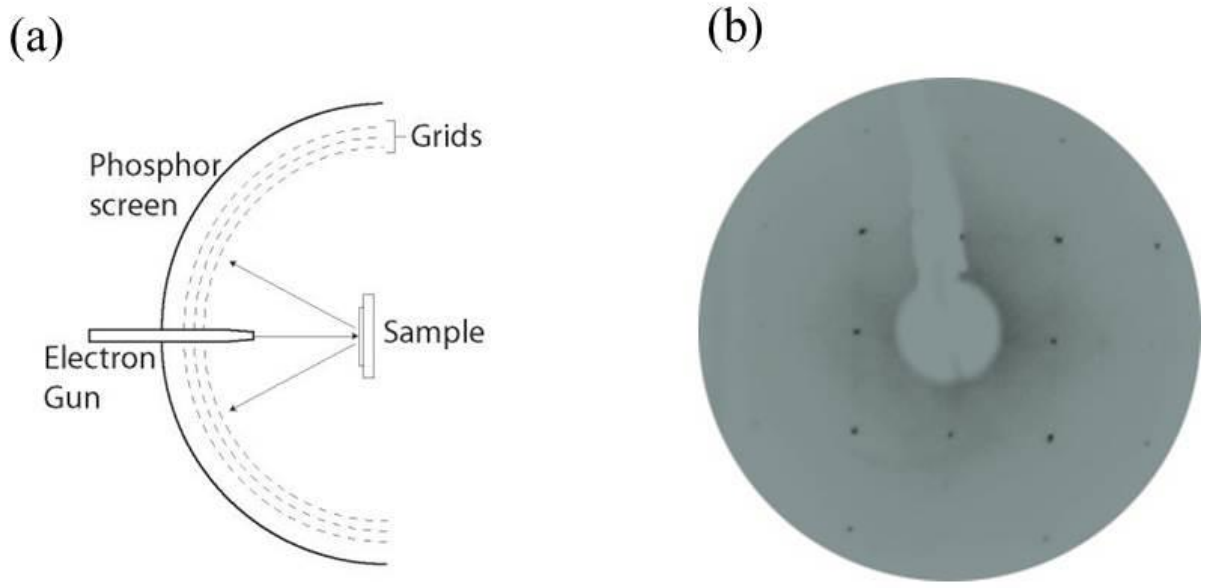

Figure 2.4. (a) Schematic of the LEED. The electron beam is elastically reflected by the sample surface and constructing diffractions are shown on the fluorescent phosphor screen as spots. (b) LEED diffraction pattern of $SrTiO_3$ (001) surface with energy of 125eV at T = 300K.

reliability factor (R_P-factor) is used to quantitatively evaluate the goodness of fit between the theoretical and experimental I-V curves. If R_P=0 there is perfect correlation between the theoretical and experimental I-V curves, while R_P=1 means that they are completely uncorrelated. The lower R_P factor acquired, the better is the surface structural determination. Usually, it is confident if $R_P < 0.3$.

The LEED instrument in our lab is an Omicron LEED. It works in the UHV system where the pressure is usually maintained at low 10^{-10} Torr. LEED I-V data acquisition is done with a high resolution camera and LabView programmed software.

2.3.2 Scanning tunneling microscopy and spectroscopy (STM/STS)

The STM is a technique for imaging surfaces in real space at the atomic resolution based on quantum tunneling theory. When a conducting tip is brought very close to the sample surface, a voltage bias applied between the two can allow electrons to tunnel through the vacuum between them. The tunneling current can be fairly well approximated by:

$$I \approx \frac{4\pi e}{\hbar} e^{-\frac{1}{2}\sqrt{\frac{8m\varphi}{\hbar^2}}} \rho_t(0) \int_{-eV}^{0} \rho_s(\varepsilon) d\varepsilon \quad (2.1)$$

where I is the current, m is the electron mass, φ is the local barrier height, ρ is the local density of states (LDOS), subscript t means tip and s means sample. The integral integrates the LDOS starts from the bias below the Fermi level up to the Fermi level.

In Figure 2.5 (a), a photo of our variable temperature scanning tunneling microscopy

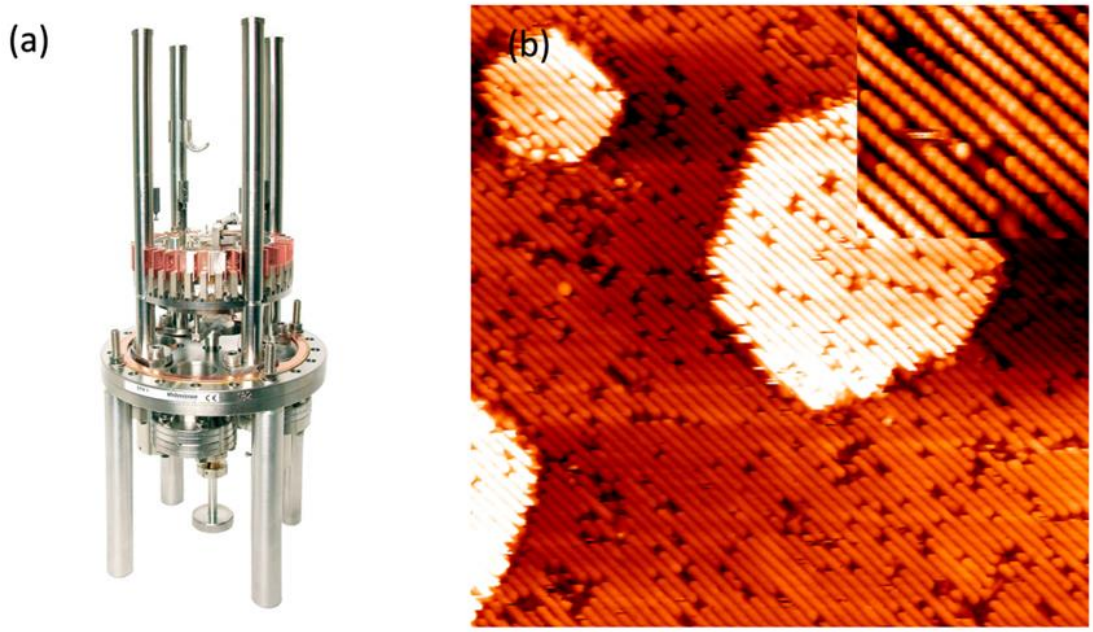

Figure 2.5. (a) A photo of Omicron VT-STM. (b) A topographic image of TiO_2 (110)-(2×1) surface using Omicron STM. The inset is a zoom-in image. The image is acquired at room temperature with V_{bias} = 2.0 V and I = 0.1 nA.

(VT-STM) is presented. The STM in our lab is a newly designed Omicron combination of STM and Q-Plus AFM (Atomic force microscopy). Figure 2.5 (b) is an example of high-resolution STM image on TiO_2 (110) (2×1)-reconstructed surface.

In addition to imaging the surface topography, STM also allows one to probe the local LDOS on the surfaces. This is due to the fact that the derivative of tunneling current with respect to the bias voltage is proportional to the LDOS: $\frac{dI}{dV} \propto \text{LDOS (eV)}$. This mode is specifically called Scanning Tunneling Spectroscopy (STS). In the surface topography imaging mode, the tunneling current is held constant; while in STS mode, the tip stops scanning at a certain location to obtain an I-V curve. The piezo feedback signal is temporarily frozen in place to hold constant the spacing between the tip and the sample, while the tip-sample bias is swept through a desired range, and the tunneling current is recorded. Through this method, the information of the metallicity of the sample surface can directly be obtained by checking the dI/dV value at the zero bias, which makes it very useful for probing the MIT.

Apart from the dI/dV (V) curve, the shape of the I-V curve can also provide support to the information of the surface metallicity of the sample. For a metallic surface, one will expect the I-V curve to be somewhat linear-like with varying voltage. On the other hand, for nonmetallic surface, the presence of gap in the density of states will result in a partially flat I-V curve, as shown in Figure 2.6.

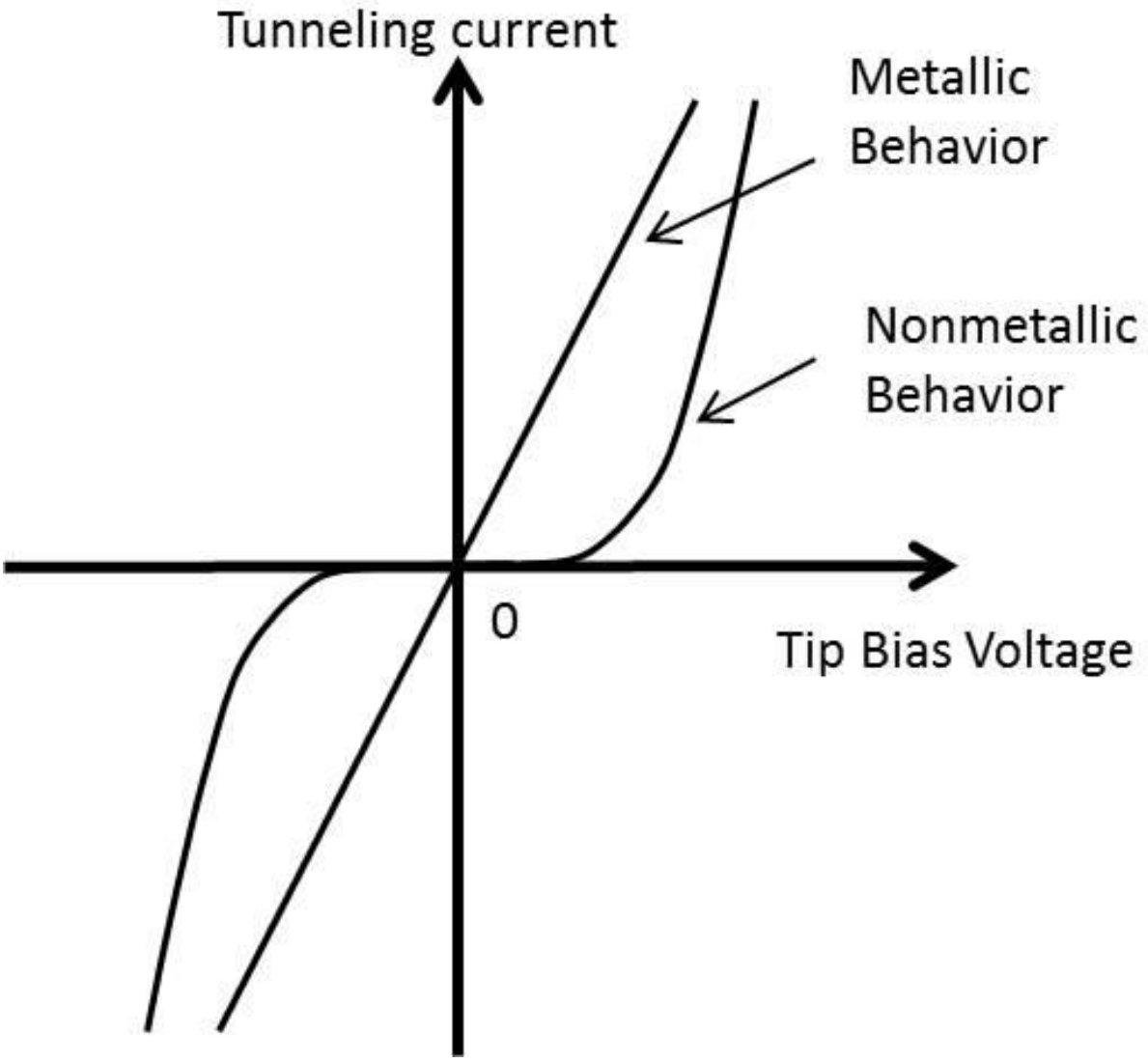

Figure 2.6. A rough sketch of the expected STS curves for metallic and insulating sample surfaces.

2.3.3 Photoemission Spectroscopy: X-ray photoelectron Spectroscopy (XPS) and Ultraviolet Photoemission Spectroscopy (UPS)

Photoemission spectroscopy (PES) is an extensively used technique in physics, chemistry and biology to investigate the electronic structure of matter based on the photoelectric effect, as shown in Figure 2.7. When a beam of light with energy $\hbar\omega$ hits a solid, an electron in the solid

with binding energy E_b will absorb the photons and be emitted as a photoelectron. With the energy conservation, the kinetic energy E_k of the photoelectron is

$$E_k = \hbar\omega - (E_b + \phi) \quad (2.2)$$

where E_b, E_k are defined as above, and ϕ is the work function of the spectrometer. These photoelectrons will be collected by a kinetic energy analyzer and reach the detector, where their

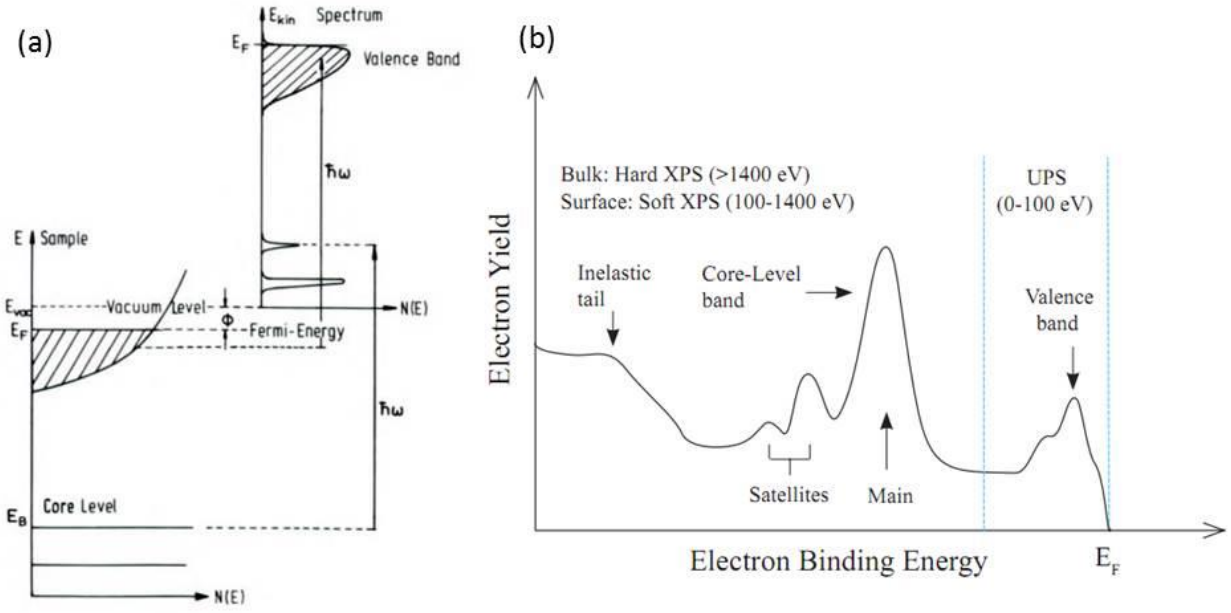

Figure 2.7. (a) Energetics of the photoemission process [36]. (b) A schematic photoemission spectrum produced by experiments.

momentum and energy information is recorded. PES can be divided into three regimes based on the energy of the photon used in the experiments. The ultraviolet regime (5-100 eV, UPS) is used to explore the low-energy excitations of the valences bands, the soft X-ray regime (100~10^3 eV, Soft XPS) is used to investigate the core-level excitations of electrons in the sample surface while the hard X-ray regime (10^3~10^4 eV, Hard XPS) has to be achieved by synchrotron

radiation and is used to study the core-level excitation of electrons in the bulk. In our lab, we will only use the former two kinds of setup for the characterization of the sample. A schematic diagram of the experimental setup of XPS is shown in Figure 2.8. By replacing the X-ray source with an ultraviolet light source, UPS is realized. Moreover, by adjusting the relative angle between the sample and the analyzer in UPS, we can detect not only the kinetic energy of the photoelectrons but also their momentum. This mode is also named Angle-Resolved Photoemission Spectroscopy (ARPES). In ARPES, the initial momentum of an electron in the plane parallel to the sample surface, denoted as $K_{||i}$, is conserved while the momentum perpendicular to the surface is not. Therefore, apart from the energy conservation equation (2.2), we also have a similar equation for the momentum:

$$|K_{||i}| = |K_{||f}| = \frac{\sqrt{2mE_k}}{\hbar}\sin\phi \tag{2.3}$$

where ϕ is the relative angle between the sample normal and the central axis of the analyzer collection cone, E_k is the kinetic energy, m is the mass of the photoelectron and i and f denote the initial and the final momentum in the surface plane respectively.

In our system, the XPS setup consists of an X-ray source XR 50 M with Al anode (Al K_α 1486.6eV), a FOCUS 500 X-Ray Monochromator and a PHOIBOS-150 analyzer from the Specs Company. The UPS/ARPES setup shares the same analyzer with XPS, the resolution of which is about 7meV in energy and 0.1 rad in angle. The source for ARPES is a standard VUV5k UV source equipped with a VUV5040 UV monochromator, which produces plasma Helium discharge at ~ 21.2 eV.

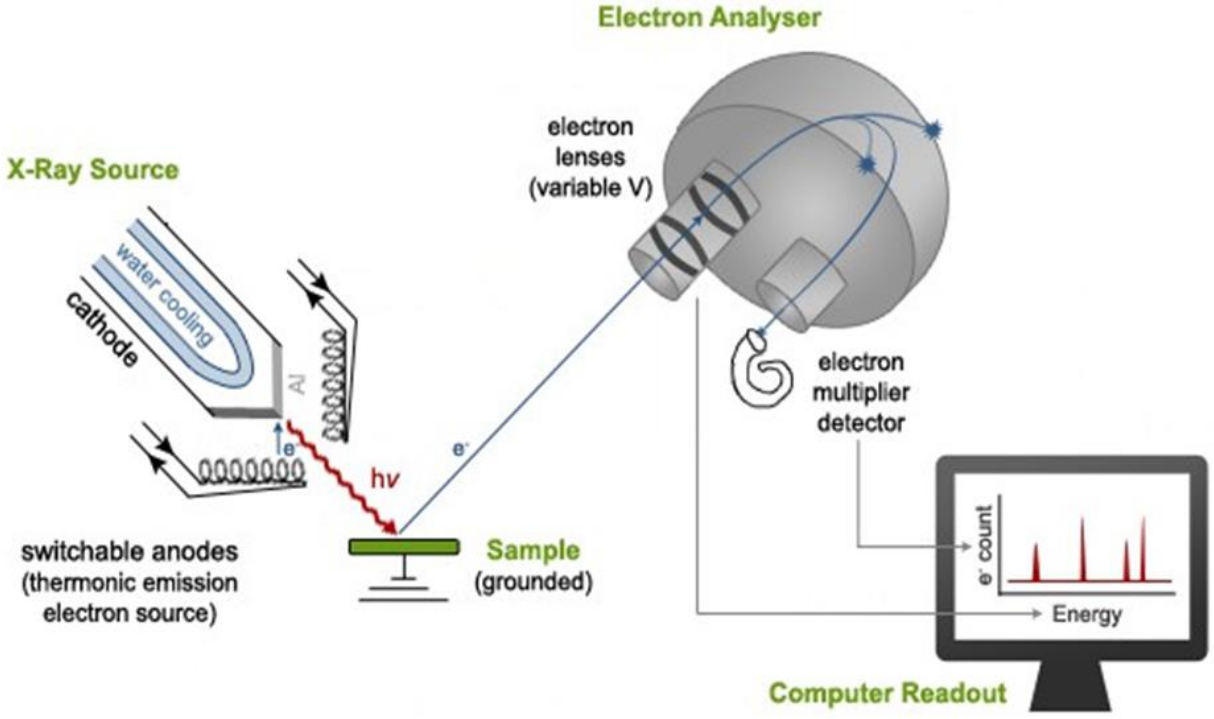

Figure 2.8. Experimental setup of X-ray photoelectron spectrometer

The use of different photon energy determines the difference in functionality of XPS and UPS/ARPES. XPS explores the core-level of the elements and quantitatively measures the elemental composition, empirical formula, chemical state and electronic state of the elements that exist within a material. On the other hand, UPS/ARPES mainly probes the electron near the Fermi surface, and serves as a direct experimental technique for the observation of the distribution of the electrons in the reciprocal space of solids.

2.4 Ex-situ Characterization

Compared to the in-situ techniques stated in the previous section, which mostly focus on detecting the film surface, the ex-situ techniques allow us to gain information near the

film/substrate interface and the more general properties of the film like transport and magnetic properties. In the following section, we will give a brief introduction of the ex-situ techniques we applied in this study, Scanning Transmission Electron Microscopy/Electron Energy Loss Spectroscopy (STEM/EELS) and Physical Property Measurement System (PPMS).

2.4.1 Scanning Transmission Electron Microscopy/Electron Energy Loss Spectroscopy (STEM/EELS)

Scanning transmission electron microscopy (STEM) is one type of transmission electron microscope (TEM). In TEM, an electron beam is transmitted through an ultrathin specimen, forming images from the interaction of the electrons with the sample. The images are then magnified and collected by an imaging device, providing a direct mapping of atoms positions. The first TEM was designed after de Broglie's theory of matter waves was brought up, when scientist realized that other than light, electrons could also serve as a powerful source which could theoretically allow imaging specimen down to atomic scales due to the small De Broglie wavelength of electrons. With years of development improvement of TEM imaging properties, the first modern STEM was developed in the 1970s, with Albert Crewe at the University of Chicago developing the field emission gun [37] and adding a high quality objective lens. As an improvement to the conventional TEM, in STEM the electron beam is well-focused to a fine spot and then scanned over the sample in a raster, which enables the application of analytical techniques during imaging like Energy Dispersive X-ray (EDX) Spectroscopy and Electron Energy Loss Spectroscopy (EELS), and allows one to gather images and spectroscopic data

simultaneously. A schematic diagram of STEM/EELS instruments used is shown in Fig. 2.9. The electron beam goes through a set of magnetic lens and aperture before reaching the sample. The

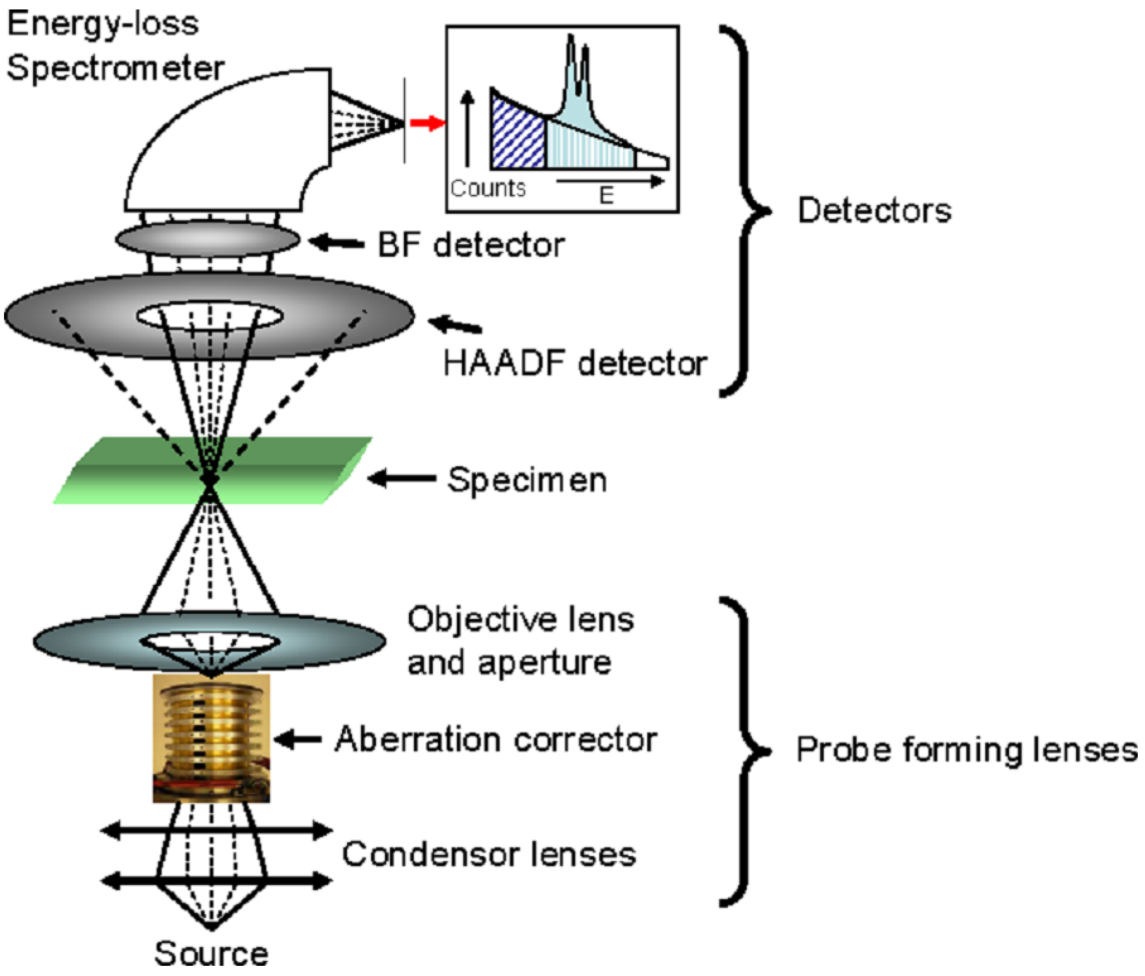

Figure 2.9. A schematic view of STEM/EELS system [38].

existence of the aberration corrector enables the electron beam to be focused to sub-Angstrom diameters, which is the most critical part for controlling the image resolution. The most advanced aberration-corrected STEMs existing nowadays have been developed with sub-50 pm resolution [39]. The fine-focus beam is controlled by scanning coils and raster-scanned across the sample,

during which process various modes of signal collection are applied, the most common among which are High Angle Annular Dark Field (HAADF) imaging, Annular Bright Field (ABF) imaging and EELS.

HAADF imaging is formed only by collecting electrons scattered at very high angles in a ring-shaped circumference. These angles are typically too large for coherent elastic scattering so the atom positions can be directly measured in the images with much reduced or even eliminated diffraction effect. The Coulombic interaction between the electron beam and the nucleus is dominating in the HAADF mode. The image intensity is ideally proportional to Z^2, with Z being the atomic number, thus making it sensitive to heavy elements. For lighter elements like oxygen and such, HAADF is unable to identify these elements; in which case the ABF imaging comes to the spotlight. ABF collects the scattered electrons from a ring-shaped circumference that is much smaller in semi-angle compared to HAADF, near the center of the beam path. Unlike HAADF, ABF images are sensitive to both lightweight and heavy elements. However, ABF imaging also has its disadvantages. It is strongly dependent on sample thickness and defocus, which makes the interpretation of ABF images more complicated than HAADF.

Apart from structural imaging, spectroscopic information like EELS can also be collected to give chemical composition and electronic structures about a specimen. As the electron beam travel through a specimen, some electrons will lose energy through inelastic scattering interactions with the sample. In EELS, an electron spectrometer is used for measuring the energy loss distribution of the scattered electrons, which allows us to identify the inelastic interactions

like plasmons, phonons and such. EELS is also capable of observing the fine structure of ionization edges, which is unique for each element, thus enabling EELS for elemental mapping and chemical spectroscopically mapping down to atomic scales [40].

Our STEM study is performed in Brookhaven National Laboratory. Cross-section TEM sample were prepared by Focused Ion Beam (FIB) with Ga^+ ions following by the Ar^+ ions Nano-milling. The microscopy work was performed on a JEOL ARM200 microscope at Brookhaven National Laboratory (BNL) equipped with two aberration correctors. High-angle annular dark-field (HAADF) STEM images were collected with a HAADF detector with an inner angle of 18 mrad and outer angle of 160 mrad. All electron energy loss spectroscopy (EELS) were acquired at a convergence angle of 18 mrad and a collection angle of 120 mrad. An energy dispersion of 0.25eV/channel with energy resolution of ~0.8eV was used for fine structure study of EELS spectra. The EELS spectra of ionization edges for each element were obtained simultaneously at an energy dispersion of 1eV/channel for composition analysis. Dural EELS mode was used in order to calibrate the energy shift in the spectra collection process.

2.4.2 Physical Property Measurement System (PPMS)

The transport properties and the magnetoresistance in this study are measured by a commercial Physical Properties Measurement System (PPMS) from Quantum Design Inc. shown in Fig. 2.10 (a). PPMS is designed to perform a variety of macroscopic measurements like transport, specific heat, magnetoresistance, thermal transport and susceptibility.

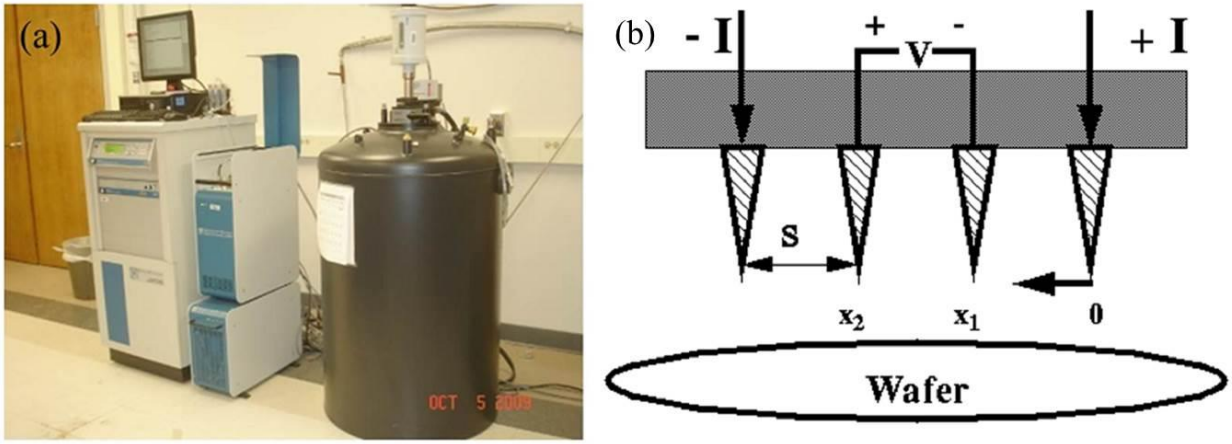

Figure 2.10. (a) The Physical Property Measurement System (PPMS), which is the instrument used in this study. (b) A schematic diagram of the four-point probe measurements.

To measure the transport, four-point probe method is applied to all our films. Four-point probe based measurement is a long-established standard technique which is widely used for measuring the average resistance of thin films. A schematic view of the four-point probe setup is shown in Fig. 2.10 (b). The current is passed through the outside two points of the probe and voltage drop is measured across the inside two points. Compared with the traditional two-point probe method, the four-point probe measurements can eliminate the contact resistance created by the ohmic contact of the probes and the sample, and are therefore much more accurate. We will discuss the four-point probe methods in more details in the later chapters.

2.5 Summary

The most important topic in surface science today is how to delicately control the fabrication and characterization of the material down to atomic scale. For complex materials, RHEED monitored Laser-MBE has been a widely used technique for achieving well-controlled

layer-by-layer growth with only one unit cell of surface roughness. The in-situ transfer best guarantees the cleanness and quality of the sample surface during characterization. LEED and STM can be used to study the film surface structure and morphology; while the chemical composition, electronic properties of the films are investigated by XPS, UPS/ARPES and STS. For the more general properties of the films and the information inside the film and near the interface, ex-situ tools like PPMS and STEM/EELS are used for analysis. The combination of these powerful tools allows us to systematically study the properties of the films down to atomic level and helps us to gain more understanding of the system from the microscopic point of view.

Chapter 3. SVO Film Growth and Film Quality

3.1 Introduction

In this chapter, we mainly focus on the growth process and characterization of SVO films to prove that our films are of high quality. Our SVO films are grown on the $SrTiO_3$ (001) (STO) substrates, which need to be treated before achieving a flat surface that is ideal for film growth. We will start by introducing the process of substrate and then come to the optimization of the film growth by Laser-MBE and RHEED. XPS, LEED and STM are applied for confirming the quality of the film.

3.2 Substrate Preparation

In our study, STO (001) were used as the substrates for film growth. STO is one of the most widely used substrates for oxide thin film growth due to its compatible lattice constant with a variety of materials like manganites, titanates, ruthenates and so on. Many interesting phenomena have been observed at the interface of other materials and STO including the two-dimensional electron gas and superconductivity [41-43]. STO is an insulating cubic perovskite with a band gap of 3.2 eV. Doping by Nb or self-doping with oxygen vacancies changes STO to an n-type semiconductor and makes it suitable for both in-situ and ex-situ analysis. By HF buffer solution etching and subsequent annealing, atomically flat TiO_2 terminated surface can be obtained for the STO for the best preparation for the epitaxial film growth [44].

STO and SVO have bulk lattice constants of 0.3905 nm and 0.384 nm, respectively, which results in a reasonable lattice mismatch of approximately 1.6%, causing the SVO film to go under tensile strain. For our in-situ measurements like LEED, XPS, UPS and STM/STS, 0.1wt% Nb doped STO substrates were used to prevent the charging effect caused by the accumulation of electrical charges on the sample. For ex-situ transport measurements, the non-doped STO substrates have to be used to avoid interferences with the film transport. All the STO substrates used in our study were single crystals supplied by CrysTec GmbH from Germany, in the size of 5 mm $\times$ 5 mm $\times$ 0.5 mm.

In order to get an atomically-flat substrate surface for the best of film growth, a certain process of treatments has to be applied on STO. Firstly, the STO substrates are cleaned using an ultrasonic cleaner to get rid of the impurities attached on the surface in the following sequence: (1) in acetone for 4min, (2) in ethanol for 4 min and (3) deionized water for 4 min. The substrates are then dried subsequently by ultrapure N_2 gas to remove the residual water. Secondly, the clean STO substrates are etched for 30s in the buffered-oxide- etch 10:1 solution (also known as buffered-HF) from J.T. Baker. The substrates are then rinsed off with water to remove the residual HF and dried again. Thirdly, the STO substrates are annealed in oxygen in a furnace under 950˚C for 1h to ensure an atomically flat TiO_2-terminated surface and efficiently reduce the forming of oxygen vacancies in the substrates.

3.3 SVO Film Growth and Quality

In this section, we discuss the details of the optimization of the growth conditions and the confirmation of the quality of the SVO films. We show that successful 2D layer-by-layer growth has been obtained by PLD while monitored by RHEED. The film was checked by XPS, STM, LEED and XRD, which proved the films are of good quality.

3.3.1 SVO film Growth with Laser-MBE and RHEED

With a near-stoichiometric $SrVO_3$ target, we have deposited SVO films on the TiO_2-terminated substrates prepared as stated in the last section using the Laser-MBE system. During the growth process, RHEED patterns and oscillations were used to monitor the film surface to make sure the growth occurs in a 2D layer-by-layer fashion. The LBME growth is a complicated dynamic process which involves many parameters, like substrate temperature, gas partial pressure, laser energy intensity, laser frequency, and so on. In order to get optimized growth, we have explored the effects of tuning each parameter mentioned above, and found out that the SVO film growth can only be stabilized within a somewhat narrow parameter window. In the following, we will explain this in details.

3.3.1.1 Oxygen Partial Pressure

The naturally stable valence for vanadium is 5+, making a $SrVO_3$ a very easily oxidized compound. With this fact in mind, we assume that oxygen partial pressure would be the most sensitive growth parameter in SVO film growth, which later proved to be the case. We have found that introducing oxygen even in the order of 10^{-7} Torr will result in a 3D growth pattern,

which indicates that the film is of poor quality with a significant amount of islands formed on the film surface. Therefore, we have chosen to grow the SVO films in ultra-high vacuum of 10^{-8} Torr without oxygen, which allowed us to stabilize a 2D growth.

3.3.1.2 Substrate Temperature

We have tried growing SVO films with substrate temperatures from 500˚C to 800˚C and found the growth optimized at 600-650˚C. At lower temperatures, the growth speed tends to slow down and eventually becomes 3D. At higher temperatures, the growth is maintained in 2D mode, but the RHEED oscillations vanish faster than those of the films grown at the optimized temperature, indicating the likely possibility of having step-flow growth instead. To obtain layer-by-layer growth, we have fixed our substrate temperature at the optimized 600-650˚C.

3.3.1.3 Laser Energy and Frequency

For film growth, we used a 248 nm KrF excimer laser to ablate the target at a frequency of 3Hz with an energy intensity of approximately 2.5 J/cm^2. We have found that lower frequency and intensity would slow down the speed of growth and make it go to 3D easily, while a frequency/intensity too high was likely to cause uneven ablation of the target, which is also not preferable for achieving layer-by-layer growth.

Overall, we had found that the best SVO growth was always achieved with a growth speed of 13-22 seconds/layer. In order to control it, we have optimized the growth parameters as follows: no oxygen, base vacuum level of 10^{-8} Torr, substrate temperate of 600-650℃, laser pulse rate of 3Hz and energy intensity of 2.5 J/cm^2. Figure 3.1 is a picture of the RHEED pattern

and the intensity oscillation curve of a 20 ML SVO sample grown under the conditions stated above. We can conclude from the pattern that 2D layer-by-layer growth was successfully achieved.

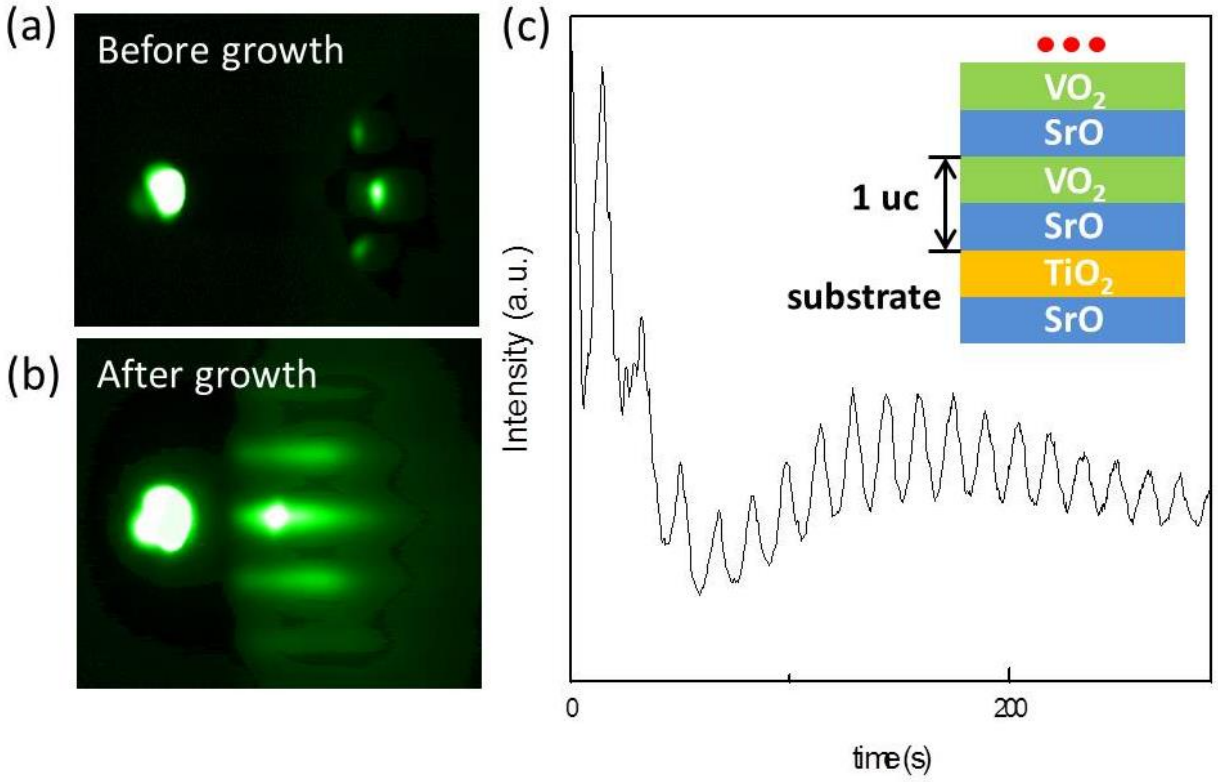

Figure 3.1. (a-b) The RHEED patterns of the substrate STO and after the SVO film growth, respectively. (c) The intensity oscillation during film growth. Each oscillation corresponds to the formation of a single unit cell, as shown in the upper right panel.

3.3.2 SVO Film Quality Characterization

We performed different characterizations to check the quality of the SVO films grown under the optimized condition mentioned in the previous part. With a good 2D layer-by-layer growth, the SVO film should be atomically flat on the surface. We demonstrate this fact by STM

morphology and LEED. Also, to confirm that the film is of correct phase, we did XPS composition check and XRD. The results will be discussed in the following sections.

3.3.2.1 STM Morphology

In Figure 3.2 (a) and (b), we present two STM morphology images of 3 u.c. and 50 u.c. SVO films respectively. In Figure 3.2 (a), we can see that the 3 u.c. film growth evidently follows the steps of the STO substrate, while some extra coverage can be seen as a result of imperfect timing

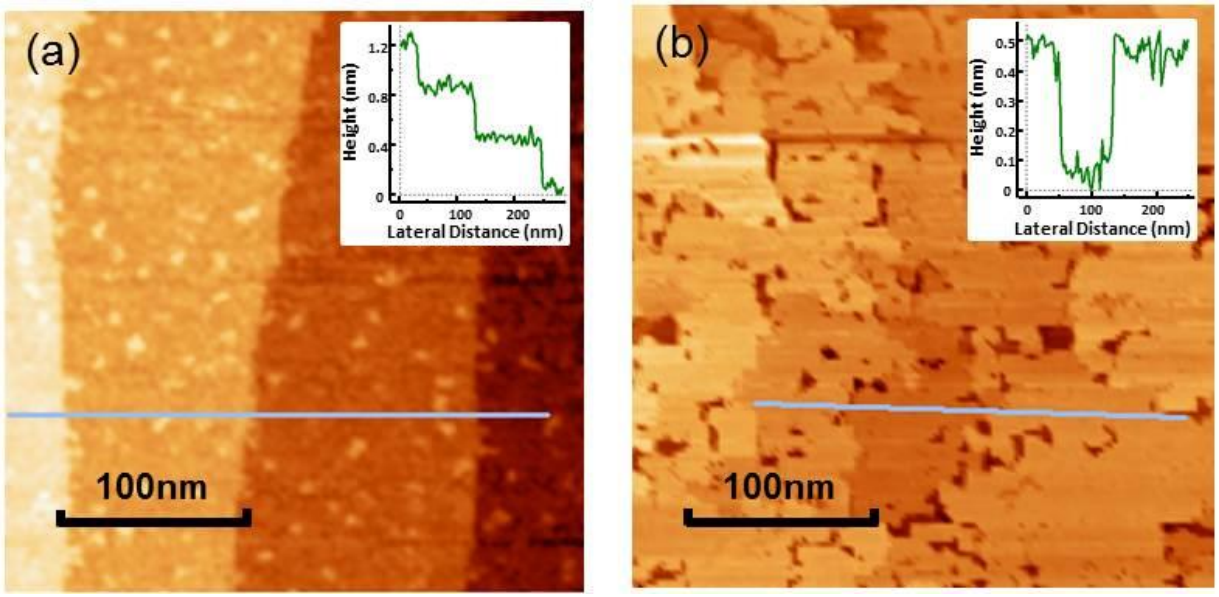

Figure 3.2. The STM images of SVO films of (a) 3 u.c. and (b) 50 u.c. with height profiles displayed in the upper right panels.

for the termination of film growth. By drawing a line profile across the terraces, the height difference can be analyzed, which is displayed in the upper right panel. If we subtract the difference between two adjacent terraces, we get the same different of ~ 0.4 nm, which is approximately the height of the one single unit cell of SVO. The 50 u.c. film, on the other hand,

as shown in Figure 3.2 (b) has a rougher surface compared to the 3 u.c. film. The step edges are no longer in straight and almost-parallel lines, which is a natural outcome as the film thickness increases. To analyze the surface roughness, we also draw the line profile across different terrace features. The same height difference of ~ 0.4 nm is obtained. The absence of clusters on the surface in both cases indicates that our films are grown in a good 2D layer-by-layer fashion with atomically flat surfaces.

3.3.2.2 LEED Image

In Figure 3.3 (a) and (b), we show the LEED images of a 100 u.c. SVO film at a beam energy of 80eV and 150eV, respectively. The 80 eV image displays a c(2x2) reconstructed

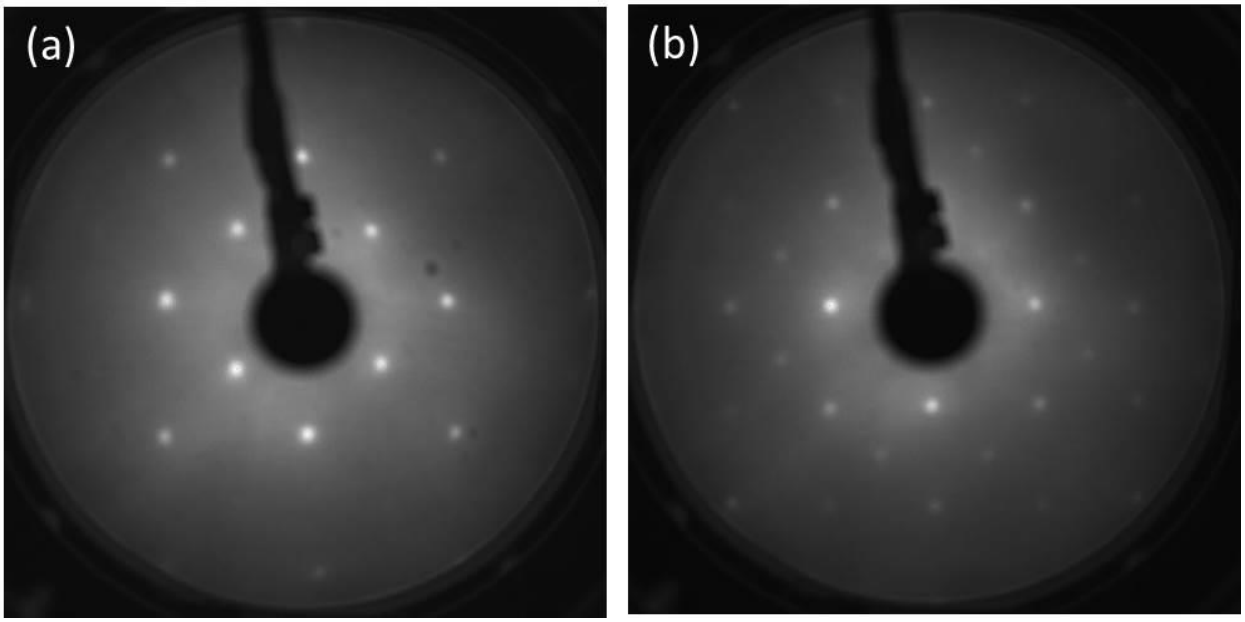

Figure 3.3. LEED image of a 100 u.c. SVO film at beam energy of (a) 80 eV and (b) 150 eV.

pattern with bright and well-defined fractional spots at the center of the original 1x1 diffracted pattern. The increase of the beam energy brings more diffraction spots to the screen, but the spots

remains sharp and clear; no extra spots other than the √2 fractional spots can be observed. This indicates that even at 100 u.c. thickness, the surface of the film is still well-ordered.

We have done some structure refinement investigation of the possible reasons behind the c(2x2) reconstruction but failed to come to any conclusion due to the complication of the system. The best guess seems to be the self-arrangement and buckling of the surface atoms, along with some possible ordered oxygen vacancy. The details will not be included in this thesis.

3.3.2.3 XPS Composition Check

The composition check of the SVO film is performed by the XPS scan across the whole binding energy range, which is shown in Figure 3.4. The spectrum is obtained from a 50 u.c.

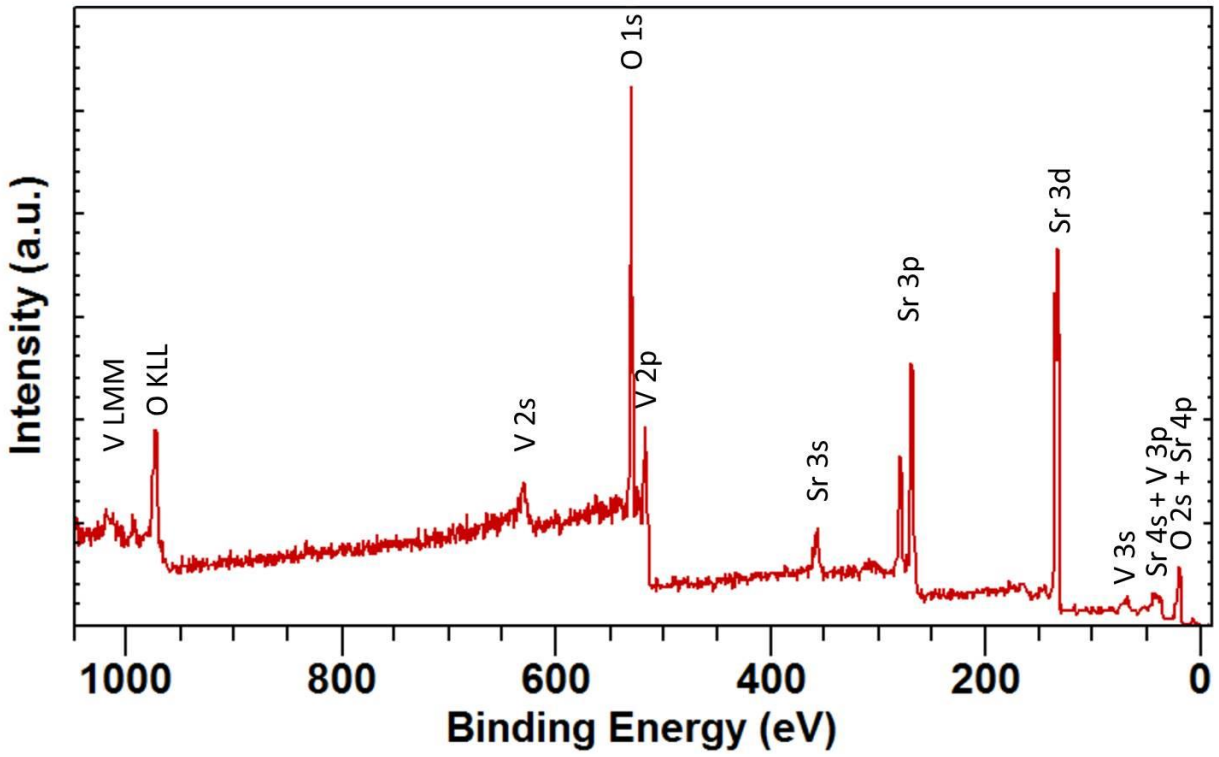

Figure 3.4. The XPS spectrum of a 50 u.c. SVO film, scanned across the binding energy range from 1050 eV to -10 eV. All the peaks are attributed to Sr, V and O.

SVO film, in which case the signal only comes from the film and not the substrate. By comparing the spectrum with the standard database of core level energies, we can see that every peak we observed in the spectrum comes from Sr, V or O and no other elements. This indicates that our film growth does not involve any impurities from other source. However, it should be noted that the above observation only proves that our film is made purely from the desired elements, but does not guarantee that it is the correct phase. To check if the film is in the correct phase, other tools like XRD or STEM must be applied.

3.4 Discussion and Summary

In the chapter, we discussed the recipe for high-quality growth of SVO films. The STO (001) substrate was prepared in a way to ensure an atomically-flat TiO_2-terminated surface without reconstruction. The growth of SVO films was optimized by changing different growth parameters like growth temperature, oxygen partial pressure and laser energy and frequency. We found that 2D layer-by-layer growth can be achieved at a growth temperature of 600~650˚C at a vacuum level of 10^{-8} Torr without introducing oxygen, with a laser intensity of ~2.5J/cm^2 at a frequency of 3Hz. Under this optimized growth condition, the atomically-flat surface of SVO films is confirmed by STM and LEED while the composition and phase of the films are checked by XPS and XRD. In the next chapter, we will focus on the characterization of the structures and chemical information of our SVO films.

Chapter 4. Structure and Chemical Composition of SVO Film

4.1 Introduction

In the last chapter, we have shown how to fabricate the SVO thin films in a layer-by-layer fashion by PLD through the control of the growth parameters and confirmed the quality of the SVO films by RHEED, LEED and STM. In this chapter, we will mainly focus on the investigation of the film structure and the chemical composition. Through STEM/EELS measurements, we can obtain a microscopic picture of both atomic arrangement and chemical information for each single layer all the way from the interface. A more global investigation of the chemical composition of SVO films of different thicknesses near the film surfaces is performed by ARXPS. We find that the SVO films we have grown does not shown preference of a single termination of VO_2 or SrO, possibly because of the unavoidable introduction of defects caused by strain relaxation. Moreover, near the interface of SVO/STO a decrease of the V-valence can be observed, indicating the existence of a significant amount of oxygen vacancies.

4.2 Structure Characterization with STEM Images

A large scale high-angle annual dark field (HAADF)-STEM image of a 50 u.c. SVO film is shown in Figure 4.1 (a). The regions of the SVO film and the STO substrate are marked out on the image with two blue arrows as indication of the location of the interface. From the image we can tell that the majority of the SVO film is uniform, but still, some stripe-like inhomogeneous features can be observed. This may be caused by defects or dislocation, but it is also possible that the features represent a completely different phase than the expected SVO (113) phase.

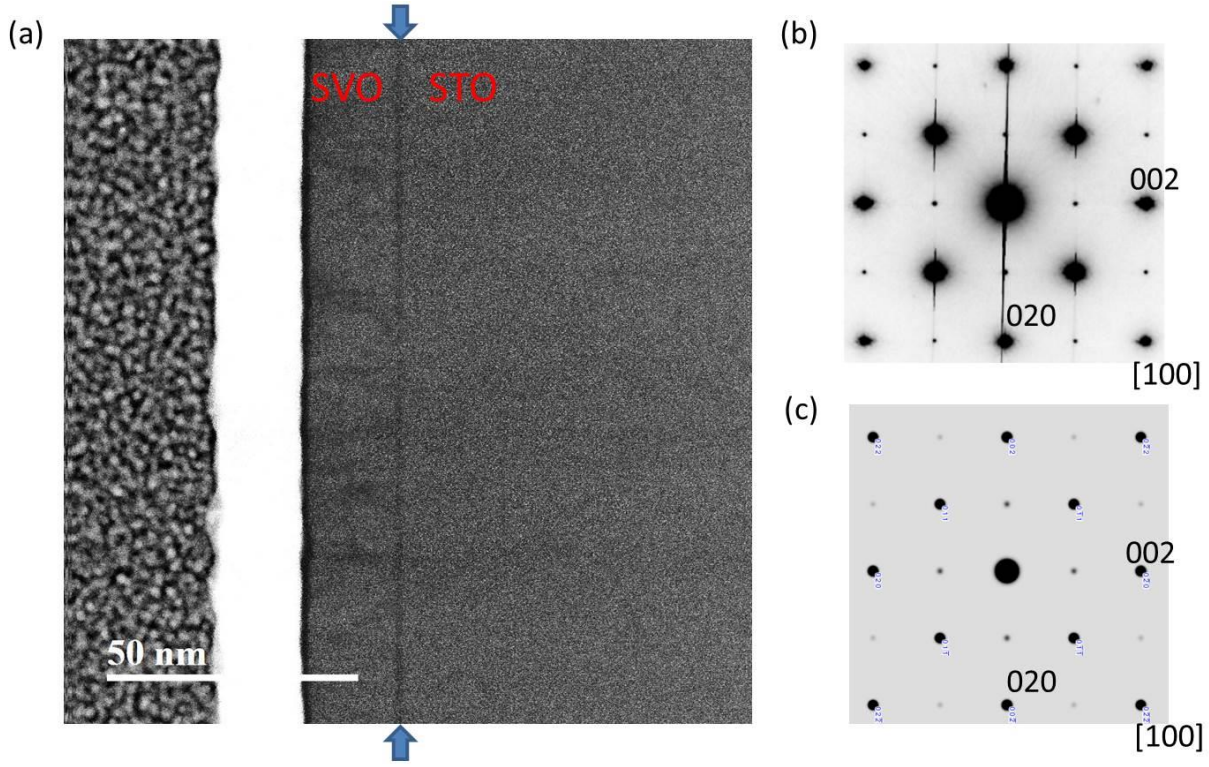

Figure 4.1. (a) Large scale HAADF-STEM image taken along [100] direction. The blue arrows indicate the location of the interface. (b) Selected area electron diffraction (SAED) pattern and (c) simulated diffraction pattern for $SrVO_3$ phase along the [100] direction showing good agreement.

Therefore, in order to confirm that the film is in the correct phase, we performed selected area electron diffraction (SAED) on the image and compared it to the simulated diffraction pattern of $SrVO_3$. The results are shown in Figure 4.1 (b) and (c). The extra trails in the SAED pattern are artifacts due to CCD saturation. From the SAED pattern, we observed no extra spots compared to the simulation of SVO (113) phase. This indicates that our film is indeed in the desired phase.

From the image in Figure 4.1, another interesting thing can be observed, and that is the obviously different intensity contrast at the interface. This implies us that near the interface there

may also be another feature. Later in this section, we will zoom in in this region and take a closer look.

Since we have confirmed that the majority of the film is in the correct phase, we will limit our following discussion to the uniform region of the SVO film. In Figure 4.2, we display a comparison of the zoomed-in HAADF and ABF images in the uniform region of the SVO films, with SVO structural models superposed on top showing the position of atoms from each element. As stated previously in Chapter 2, HAADF image is sensitive only to heavy elements with column intensity proportional to atomic number Z, while ABF image is sensitive to both heavy and light elements. This is clearly presented in Figure 4.2. Since Sr has a larger atomic number (38) than V (23), it is represented by the brighter dots in Figure 4.2 (a). The O element is absent

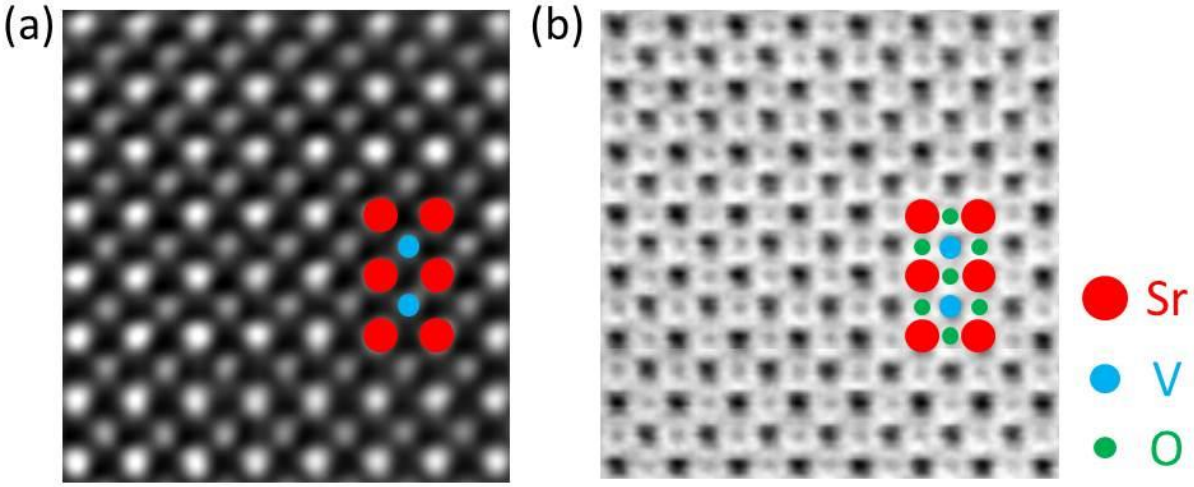

Figure 4.2. A comparison of (a) HAADF-STEM and (b) ABF-STEM images of SVO films, taken along [100] direction. Ball models of each element are shown in the images.

in the HAADF image since it is too light to be detected. In the ABF image in Figure 4.2 (b), the O atoms do show up, however. The darker dots in the image represent Sr/V and the lighter dots

are O. Both HAADF and ABF images have shown the expected stacking sequence of SVO in the correct phase. To make sure that the effect is global, several different areas in the uniform region of the film have been checked and the results are the same, once again proving that the film is in the right phase.

Now we come back to the interesting feature that we observed at the interface as shown in Fig. 4.1 (a). After zooming in the area near the interface, as shown in Figure 4.3, we can see that the interface between the film and the substrate is very sharp and well defined, which

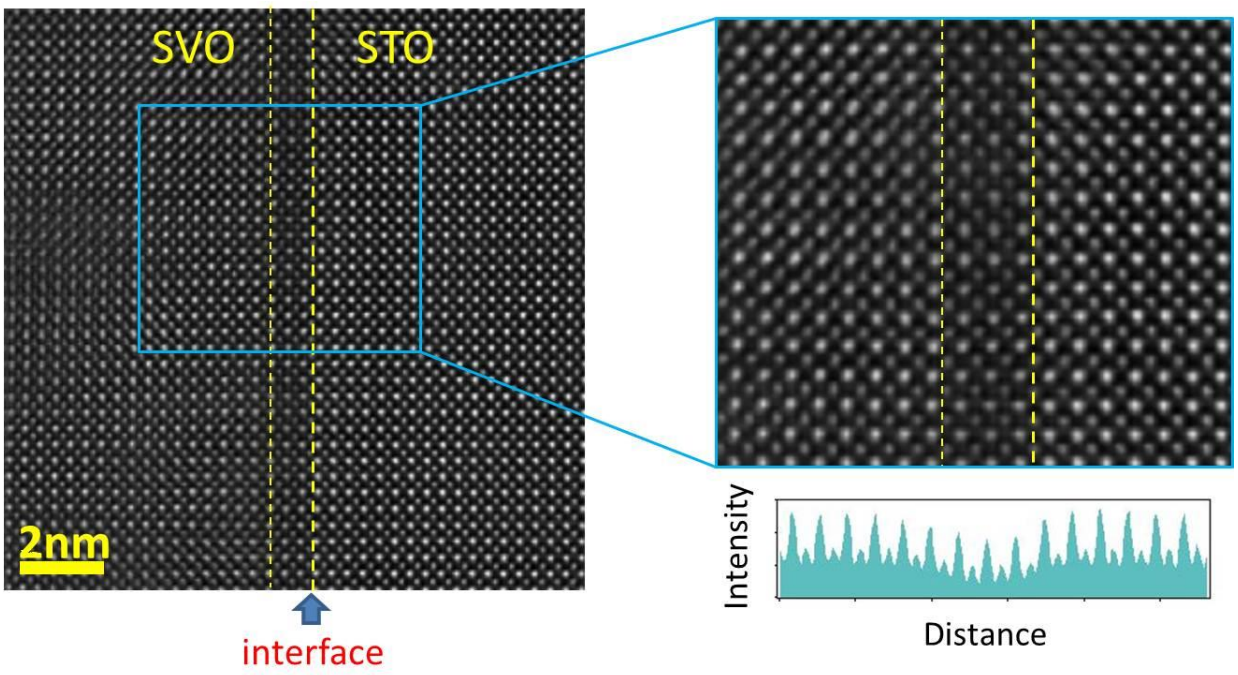

Figure 4.3. Zoomed in HAADF-STEM image near the interface. The dashed yellow lines are for the guidance of the eye. An intensity profile is plotted out and displayed for the area marked in the blue box, showing a decrease in the first three u. c. of SVO film.

indicates a coherent epitaxial growth of the SVO film on the STO substrate. In the first three layer of the SVO film, however, which we have highlighted out with visual guidelines for

convenience, a darker contrast is indeed visible; although the stacking sequence of the atoms does not appear any different from the other part of the film. We can see this more clearly from the plotted out intensity profile in the bottom right. A decrease of the intensity is obvious over the first three unit cells of film above the interface. To simply the argument later in this chapter, we will refer this part of the film as the "dark area" (DA) hereafter. To better understand this special feature, in the following section, we will apply EELS mapping and spectroscopy study to achieve more quantitative results.

4.3 Composition Probe with STEM/EELS Spectra

By the application of EELS, we have performed various detailed quantitative analysis of the region near the interface and the results are presented in Figure 4.4 and Figure 4.5. We first calculated the out-of-plane lattice constants as a function of distance from the interface, as shown in Figure 4.4 (b). The lattice constant of the STO substrate is consistent with its bulk value 3.905Å (dotted line in the red zone). For SVO film beyond the 'DA', the measured out-of-plane lattice constant also converges to the value of bulk SVO (3.84Å, dotted line in the blue zone). However, for the 'DA', the out-of-plane lattice constant expands around 3.97 Å, which is larger than both SVO and even STO. This is weird because we originally expected the lattice constant in the film near the interface to be at least the same as the bulk value, if not smaller. Our assumption is not difficult to understand because if SVO in 'DA' is stoichiometric, then the tensile strain induced by the substrate STO would like to 'stretch' the film in the in-plane direction; in order to maintain the same unit cell volume, the out-of-plane lattice constant must

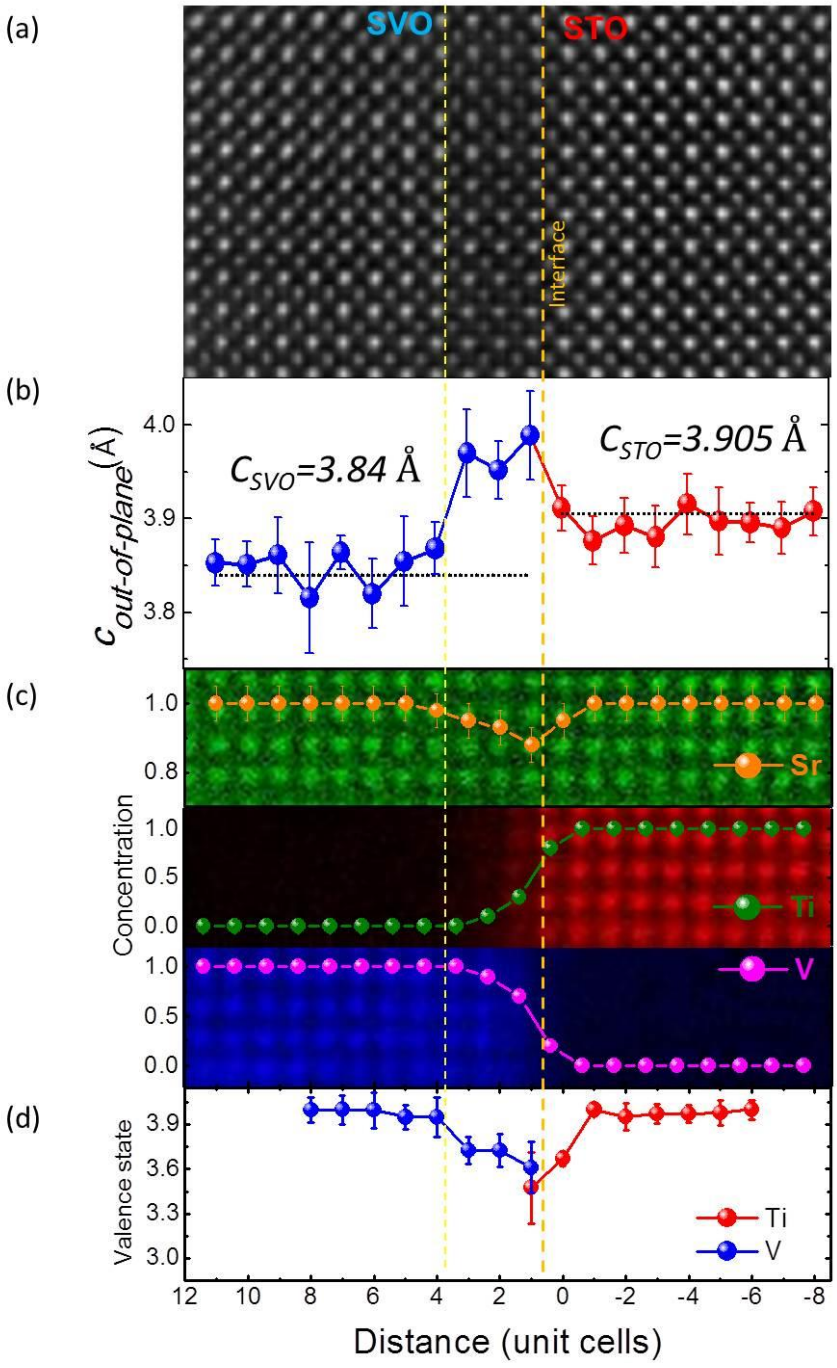

Figure 4.4. (a) HAADF-STEM image across a 50 u.c. SVO/STO film taken along [100] direction. The orange dotted line marks the interface. (b) Out-of-plane lattice constant as a function of distance from the interface (x=0), measured from HAADF-STEM image by averaging 20uc along b-axis direction. The lattice constant for bulk STO and SVO are indicated by dotted lines. (c) Falsed colored elemental maps for Sr (green), Ti (red) and V(blue), with lateral averaged profiles overlaid. (d) Oxidation state of Ti and V ions across the interface layer by layer.

then be reduced. So what should be accounted for this abnormal lattice expansion (so as the unit cell volume) that we observed in the 'DA'? Here we give the speculation that it is likely related to existence of considerable oxygen deficiency. There have been many reports on how oxygen-deficiency driving the lattice expansion in complex oxides, both in bulk and in thin film [45-47]. Also, the fact that the 'DA' has a dark contrast in HAADF-image itself indicates possible existence of oxygen-deficiency [48]. To test this speculation, we explored the film further by performing EELS elemental mapping to characterize the composition distribution and electronic structure across the interface. In Figure 4.4 (c), the atomic resolved elemental mappings of Sr-$L_{2,3}$, V-$L_{2,3}$ and Ti-$L_{2,3}$ edges are displayed. By averaging along the interface, we are able to obtain the EELS composition profiles. The elemental concentration profiles are derived from the intensity profile, which is superimposed on the corresponding atomic sites in the elemental maps. The STO substrate is terminated with a TiO_2 layer, as expected from the substrate preparation. From the concentration profile, we can see that there is a mixture of B-site atoms (Ti and V) occurring in the top layer of the STO substrate and the first two u.c. of SVO film. If we assume that the Ti and V level to be 100% in STO and SVO far away from the interface, respectively, the Ti intensity drops to about 80% in the TiO_2 termination layer of the substrate, 30% in first VO_2 layer and 10% in the second VO_2 layer. Besides the B-atom intermixing, we have also observed a slight depletion of Sr in the 'DA', which is around 10% of the amount in SVO and STO. The reason behind this Sr deficiency is still unknown to us, but there is a possibility that it has something to do with the growth process.

We further analyzed this region from the EELS spectra. The EELS spectra of V-$L_{2,3}$ and Ti-$L_{2,3}$ edge taken across the interface is displayed in Figure 4.5 (a) and (b); in Figure 4.5 (c) and (d), we plotted out the peak positions of the V and Ti L_2 and L_3 peaks respectively. The

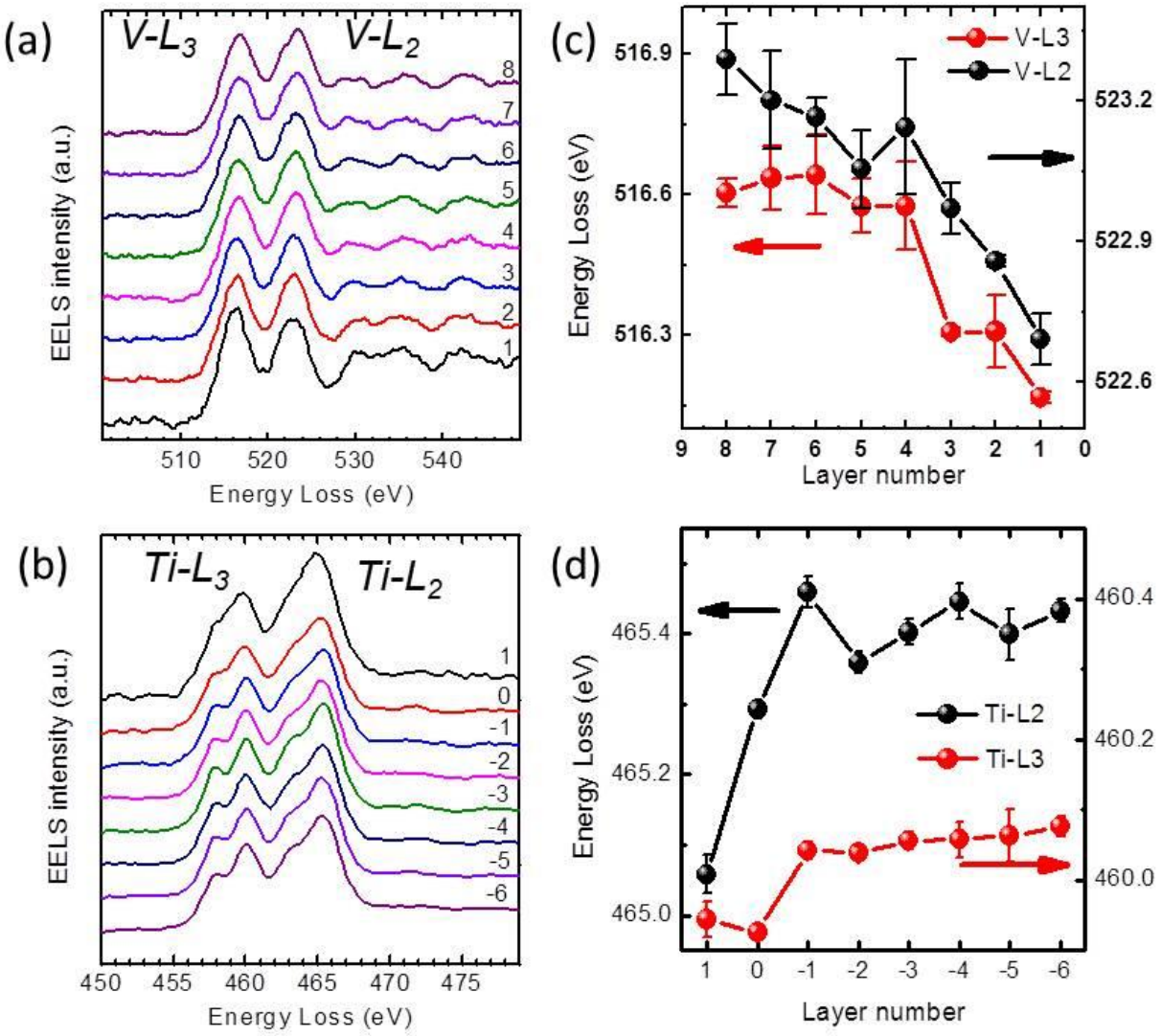

Figure 4.5. (a-b) Background subtracted V-$L_{2,3}$ and Ti-$L_{2,3}$ EELS spectra. (c-d) The energy position of V-L and Ti-L peaks.

extraction of O-K edge in SVO is hampered by the proximity of the V-$L_{2,3}$ edge so no O edges are analyzed here. For better comparison, the EELS spectra have been normalized to the

integrated intensity under the V-L edge; the spectra of Ti-L edge are normalized to the continuum interval 25 eV before the onset of the oxygen K edge. From the Figure 4.5, it is observed that a red shift of about 0.4 eV of the V-L_3 peak occurs within the first 3 u.c. from the interface, namely our 'DA'. This indicates that the vanadium valence state is reduced in this region [49]. The two Ti spectra of the TiO_2 termination layer and the doped VO_2 layer also shift towards lower energy, implying a decreased valence state of Ti ions [50]. The details on the valence change of V and Ti are calculated and plotted in Figure 4.4 (d). A drop of V-valence to about 3.6+ within the 'DA' is quite evident, along with a decrease in the oxidation state of Ti to ~3.5+ in the same region.

As a system which does not favor tilt and rotation and also being non-polar along the [100] direction, no polar-discontinuity need to be compensated by structural/charge reconstruction at the interface when SVO is grown on STO. Therefore, in order to maintain the charge neutrality near the interface ('DA'), we expect the existence of a significant amount of oxygen-deficiency; one part for compensating the slight-Sr deficiency that we observed, and the other part for the reduced oxidation of Ti and V. As we may recall from the introduction, the reported critical thickness of metal-insulator transition for SVO films is also around 2-3 u.c., about the same thickness with our 'DA'. The coincidence makes us wonder if this oxygen-deficiency that we have observed has played a certain role behind the MIT. In the next two chapters, we aim to test our assumption from two aspects: first, we would like to test the MIT itself-- whether we can observe the thickness-dependent MIT and whether it occurs at the same critical thickness; second,

if we can observe the same MIT behavior, then whether oxygen deficiency should be accounted for this. These two points are elaborated in Chapter 5 and 6, respectively. In the rest of this chapter, however, we plan to do a bit more investigation of the composition of the SVO films by another tool, angle-resolved X-ray photoelectron spectroscopy (ARXPS).

4.4 ARXPS Studies

ARXPS is no other than XPS measurements performed at a set of different emission angles. Although not designed for structural analysis, it has some different advantages compared to STEM/EELS. In ARXPS, the beam size is around 1.5 mm^2, thus it is a much more global tool compared to STEM, which allows us to explore the properties of the entire film rather than locally at microscopic level. Also, by increasing the emission angle, ARXPS can be tuned from being bulk sensitive to surface sensitive; while in STEM, during the sample preparation the surface of the film will be damaged, thus STEM mostly focus on the study inside of the film, including getting important information about the interface. In our study, we performed ARXPS on SVO films of three different thicknesses, 3 u.c., 6 u.c. and 50 u.c., and tried to analyze the films by termination and the elemental concentration characterization.

In Figure 4.6, we present the raw ARXPS spectra of Sr3d, O1s and V2p core levels for 3 u.c., 6 u.c. and 50 u.c. SVO films for a set of different emission angle θ. It is not difficult to notice that the shapes of the peaks seem to change with thickness. Partially, this is due to the change of intrinsic properties of the films with different thickness; there is also another important factor which cannot be ignored, though, which is the influence of the substrate. In the measurements

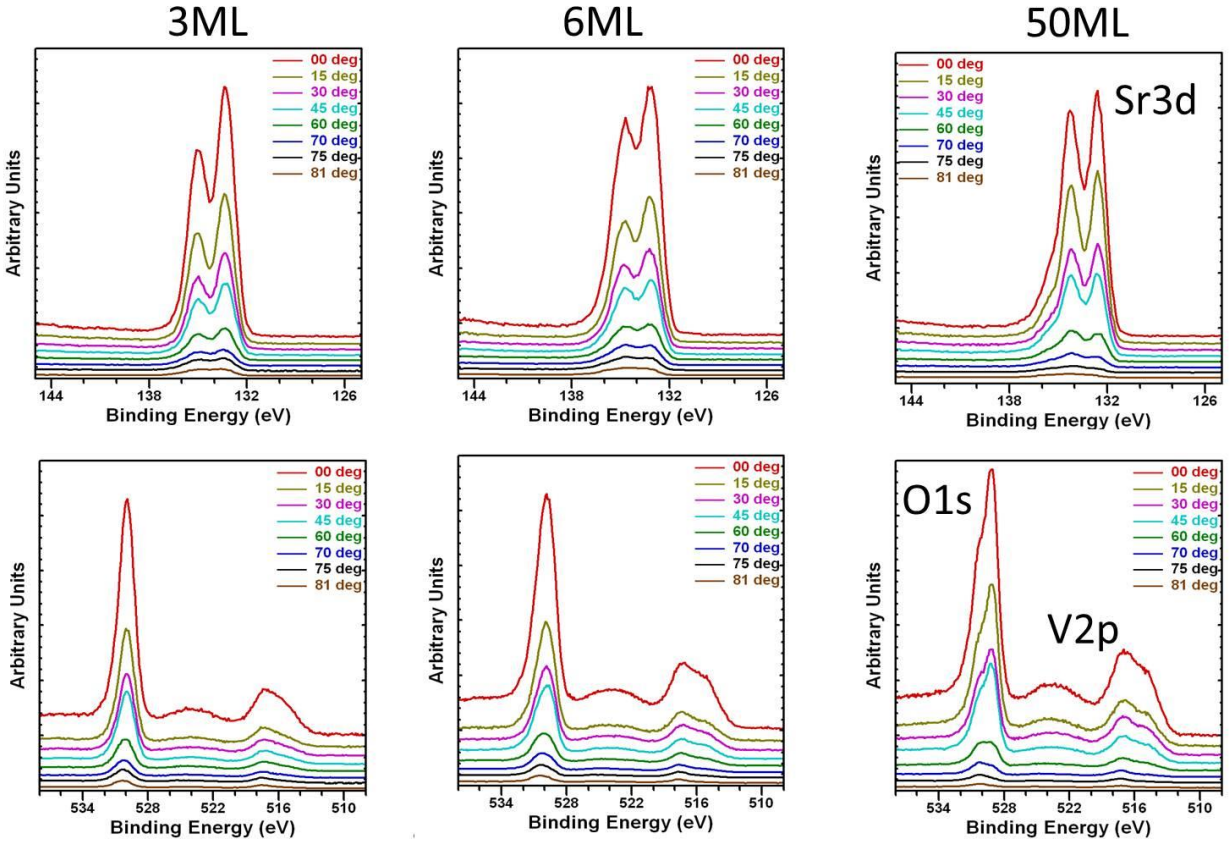

Figure 4.6. The raw ARXPS spectra of Sr3d, O1s and V2p core levels for 3 u.c., 6 u.c. and 50 u.c. SVO films.

done on the 3 u.c. and 6 u.c samples, the penetration depth exceeds the film thickness by a fair amount, at least in low emission angles; therefore, the peaks we obtained contain signals from both the film and the substrate. For a more reasonable comparison among the different films, we would like to try and remove the signals from the substrate and compare those only from the film. This is in fact a very tricky procedure which is not very widely tested and therefore not very exact. But still, we think it may offer some side support to our conclusion and we would like to try and propose a way to apply it to our study.

To begin with, we would first like to explain a little about the penetration depth we mentioned earlier. When we speak about the ‘penetration depth’ in ARXPS, in most of the cases we are not really referring to the actual penetration depth of the X-ray into the sample; rather, we mean an average of the depth from which the electrons can still escape out of the sample under a given emission angle, which is usually much smaller compared to the actual penetration depth of the photon itself. Therefore, we are really talking about the ‘electron escape depth’ when we talk about the ‘penetration depth’. In the following argument, we will still refer to this concept as the ‘penetration depth’ when we do not elaborate.

It is natural that we would assume the penetration depth to be in the same order of the electron mean free path, which actually proves to be true. Experimentally, the penetration depth can be examined by checking films with different thicknesses but grown on the same substrate. If the core level peaks from elements that only exist in the substrate can be observed, it means that the penetration depth still goes beyond the film thickness, vice versa. To be more specific, in our case, the SVO film is grown on STO substrate, so Ti is an element that only exists in the substrate and not in the film. We find that once the SVO film thickness exceeds 20 u.c., the Ti peaks can no longer be observed at normal emission, indicating a penetration depth of about 8 nm in SVO film. At an emission angle θ other than the normal emission, the penetration depth, or the part of the film that we can pull information out of from the spectra, can be roughly estimated by multiplying the normal emission penetration depth, which is 8 nm in our case, by $\cos\theta$. However, this method is not so experimentally accurate and can deviate from the actual

results by a factor of 2 approximately. To obtain more reliable results, it is recommended that we check each angle in the same way for normal emission.

According to theory, the XPS intensity ratio of two core level peaks A and B at emission angle θ can be calculated by [51]:

$$\frac{I_A}{I_B} = \frac{\sum_i N_A \cdot \exp\left(\frac{-id}{\lambda_A \cos\theta}\right)}{\sum_j N_B \cdot \exp\left(\frac{-jd}{\lambda_B \cos\theta}\right)} \cdot \frac{\sigma_A}{\sigma_B} \tag{4.1}$$

where σ_A is the photoionization cross section of element A, d is the interlayer spacing, λ is the inelastic mean free path of the photoelectrons with a certain energy, θ is the emission angle with respect to the surface normal, and N_A is number of A atoms at the ith layer. For the top surface layer, i is defined to be zero. For the quantities with the B index, same definitions apply, except they are for another element B.

By applying the above equation to the simply case of STO substrate, we will be able to get an estimate of the intensity ratios between the Sr3d, Ti2p and O1s peaks under different emission angles. Similarly, when we have films of thickness t on top of the STO substrate, the same equation can apply, except in this case, we have to add the extra thickness into the calculation. Therefore, from the above calculation, we will be able to get a whole profile of intensity ratios between Sr3d, Ti2p and O1s that comes purely from the substrate for calibration purpose.

Next, when we perform the measurements on the ultrathin films, by which we mean that the substrate can still be detected under such a film thickness, it is important that we should also collect the Ti2p peak information at all emission angles, along with the other elements we desire.

Take our case for example; for 3 u.c. and 6 u.c. SVO films, we will collect the peak intensity from Sr3d, V2p, O1s, and Ti2p. Once all the information is available, we will be able to use the intensity ratio calibrations from the substrate to estimate the actual contribution of substrate in the experimental collected peak intensities, and by subtracting that part, we can get the information on the contrition from the film. Although theoretically applicable, the actual quantitative analysis can result in a very big error bar due to the inaccurate estimate of the mean free paths and the cross sections. Nevertheless, it still offers us some qualitative insight for the film composition and we present them in the following figures.

Figure 4.7 display the intensity ratios between Sr3d, V2p and O1s peaks for SVO films of different thicknesses, both before and after the subtraction of the contribution from the substrate. By comparing the Sr3d/V2p ratios at low and high emission angles, we do not see any obvious trend of increase or decrease. This indicates that in all three cases, it is most likely that our films do not prefer a single termination of SrO or VO_2. By referring back to our observation from the STEM where we see the stripe-like defects along the growth direction, a mixed termination seems to be the reasonable outcome.

If we ignore the diffraction effect observed at certain angles in between and only compare the 0˚ and 81˚ cases and plot out the intensity ratio change over thickness, we get the results shown in Figure 4.8. Note that all results displayed here in this figure are from after subtracting the contribution from the substrate. Under both emission angles, the Sr3d/V2p ratio and the Sr3d/O1s ratio for 50 u.c. seem to be bigger than the thin films; we may interpret this as that the

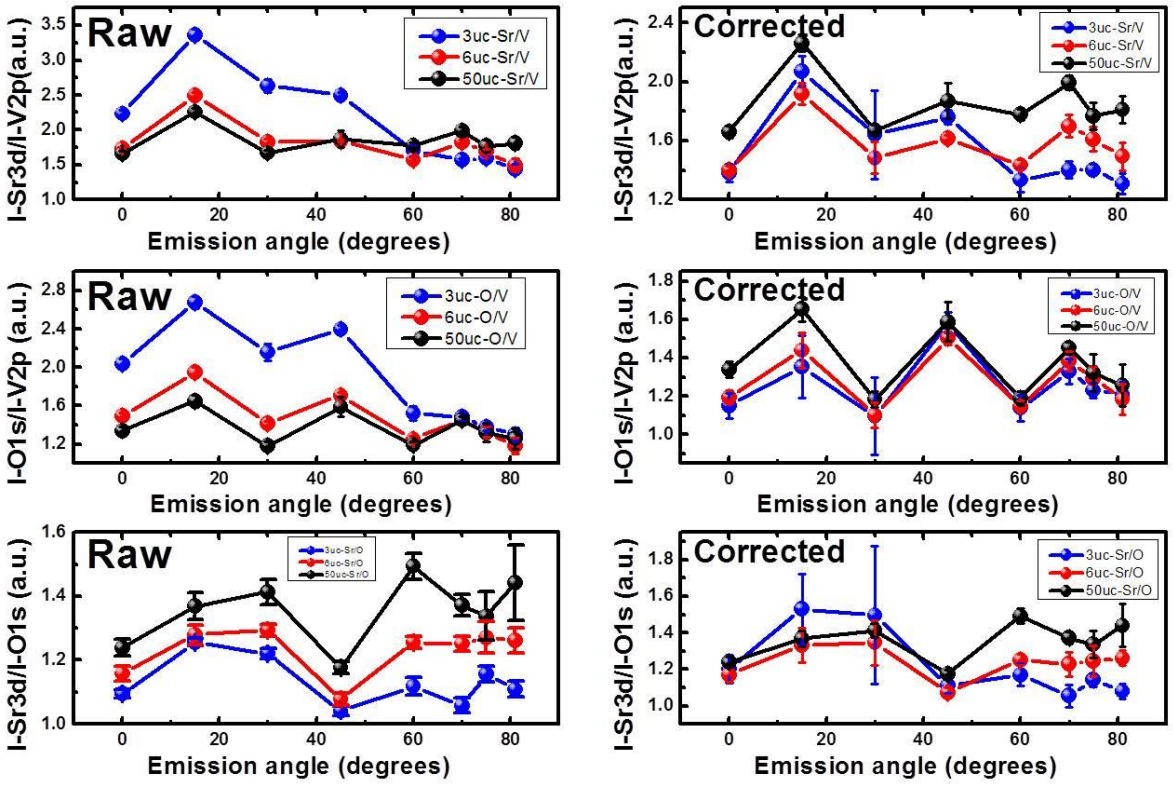

Figure 4.7. Intensity ratios between Sr3d, V2p and O1s peaks for SVO films with different thicknesses. The left panels are calculated without subtraction of the contribution from the substrate, and the right panels are the corrected calculations after subtracting the substrate information.

50 u.c. film is more Sr-rich. This is likely to be related to the introduction of more SrO defects in the growth process as the film thickness increases. For O1s/V2p ratio, it seems also to increase with thickness, at least under the normal emission. This also seems to imply that the thin films are more oxygen-deficient than the 50 u.c. film. From the top panel of Figure 4.8, we may also try and deduce some information about the surface termination. Although in all three cases, the surface termination seems to be mixed, yet in 3 u.c., a smaller Sr3d/V2p ratio at high emission angle suggests that the faction of SrO termination is slightly smaller than VO_2; in contrast, in

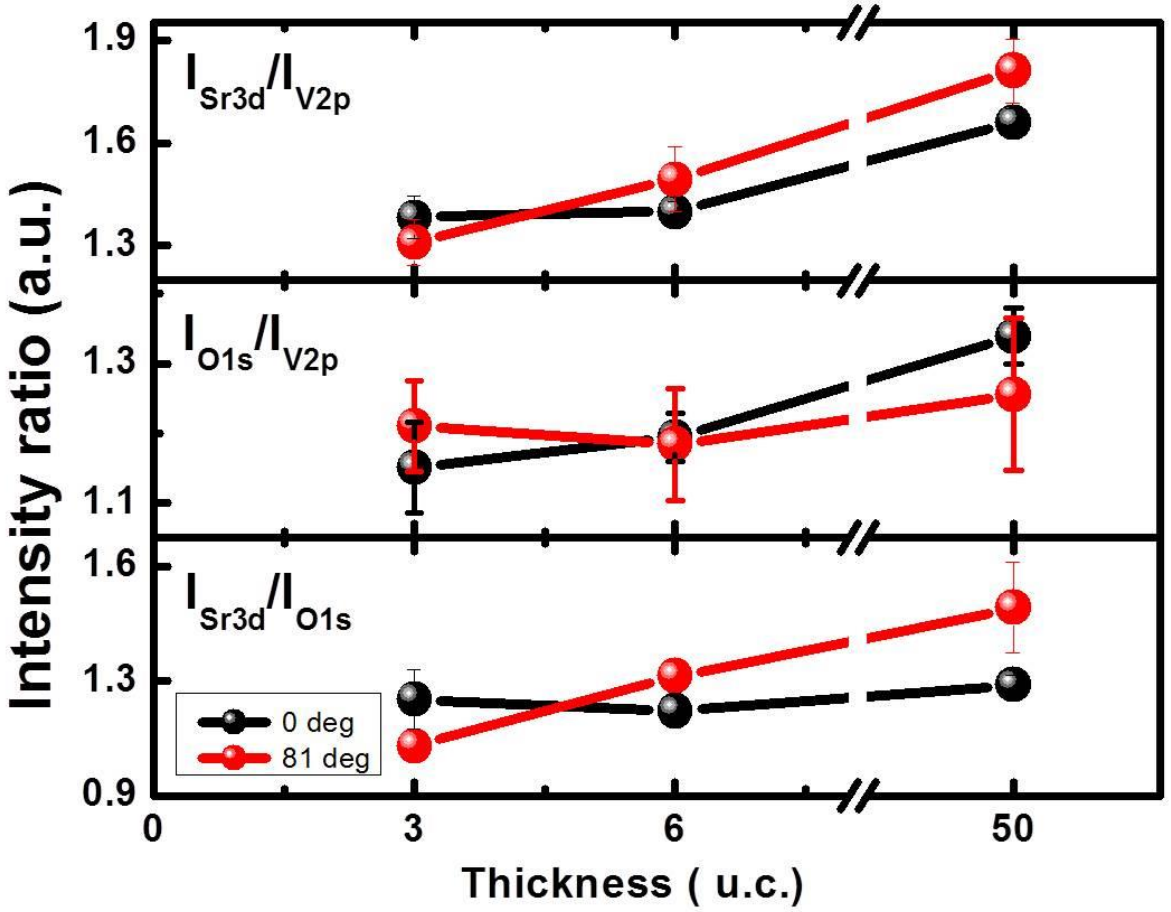

Figure 4.8. The intensity ratios comparison at 0 and 81 degrees, as a function of film thickness.

thicker films, the SrO fraction seems to be higher. This is reasonable considering the possible introduction of more SrO defects as the film grows thicker. However, as we pointed out in the previous argument, these results can have very large error bars due to the estimate of parameters; so to avoid over-interpretation, we shall only consider them as a side support rather than solid proof.

4.5 Discussion and Summary

In this chapter, we have reported our studies on the structural characterization and composition check of our SVO films by STEM/EELS and ARXPS. We have found that in the first three u.c. of the SVO film above the interface, a reduction of the oxidization state of both V and Ti can be observed, which leads to the conclusion that a significant amount of oxygen deficiency must exist in the same area. The coincidence of the thickness and the reported critical thickness has brought to our attention that there may be a link between this oxygen deficiency and the reported MIT. In the next chapters, we plan to test if the similar MIT can be observed, and whether our speculation is right that oxygen deficiency has a role to play behind it.

Chapter 5. Thickness-Dependent Properties

5.1 Introduction

In this chapter, we aim to test if our SVO films show the similar thickness-dependent MIT as the results reported by other groups, which we have already reviewed in the introduction chapter [21]. In order to do this, we will mainly focus on the investigation of the electronic properties of the SVO films and see if the behaviors show any significant change with the variation of film thickness. We have performed UPS, STS and transport measurements and found that the thickness-dependent MIT with the same critical thickness of 3 u.c. as previously reported was also observed in our SVO films.

5.2 Thickness-Dependent Properties and Metal-Insulator Transition

5.2.1 Transport Behavior

The most direct way to characterize the MIT is through the transport measurements. In order to measure the transport, four-point probe method is applied. In Chapter 2, we have given a general introduction about this widely applied technique. Now we would like to elaborate a little bit and discuss how this method is applied for the thin films.

For a two-dimensional thin film, sheet resistance is usually used for the characterization of transport behavior. In a regular bulk conductor with length L, width W and thickness t, the resistance is given by

$$R=\rho\frac{L}{Wt} \tag{5.1}$$

where ρ is the resistivity of the sample. The above equation can be rewritten with a definition of sheet resistance R_s:

$$R = \frac{\rho}{t}\frac{L}{W} = R_s\frac{L}{W} \tag{5.2}$$

If the thickness of the sample is known, then the bulk resistivity can be calculated from the above equation to be $\rho=R_s t$.

When four-point probe method is applied on a thin film, different configurations of the probes will usually lead to slight differences in the determination of transport. In our measurements, the most common configuration is applied like the one shown in Figure 5.1 (a). The four probes are aligned with an equal spacing of s between adjacent probes. For a thin film sample with infinite size (d>>s, a>>s) and a film thickness much smaller compared to the probe spacing s (t<<s), the current flow in the film is ring-shaped and the sheet resistance can be calculated to be [52-55]

$$R_s = \frac{\pi}{\ln 2}\left(\frac{V}{I}\right) = 4.5324\cdot\left(\frac{V}{I}\right) \tag{5.3}$$

Where V and I are the measured voltage and applied current in the four-point probe setup. If the sample size is finite or the sample thickness cannot be ignored compared to the probe spacing, then additional correction factors f_1 and f_2 should be introduced into the above equation, and the new expression for the sheet resistance will be

$$R_s = 4.5324\cdot\left(\frac{V}{I}\right) f_1 f_2 \tag{5.4}$$

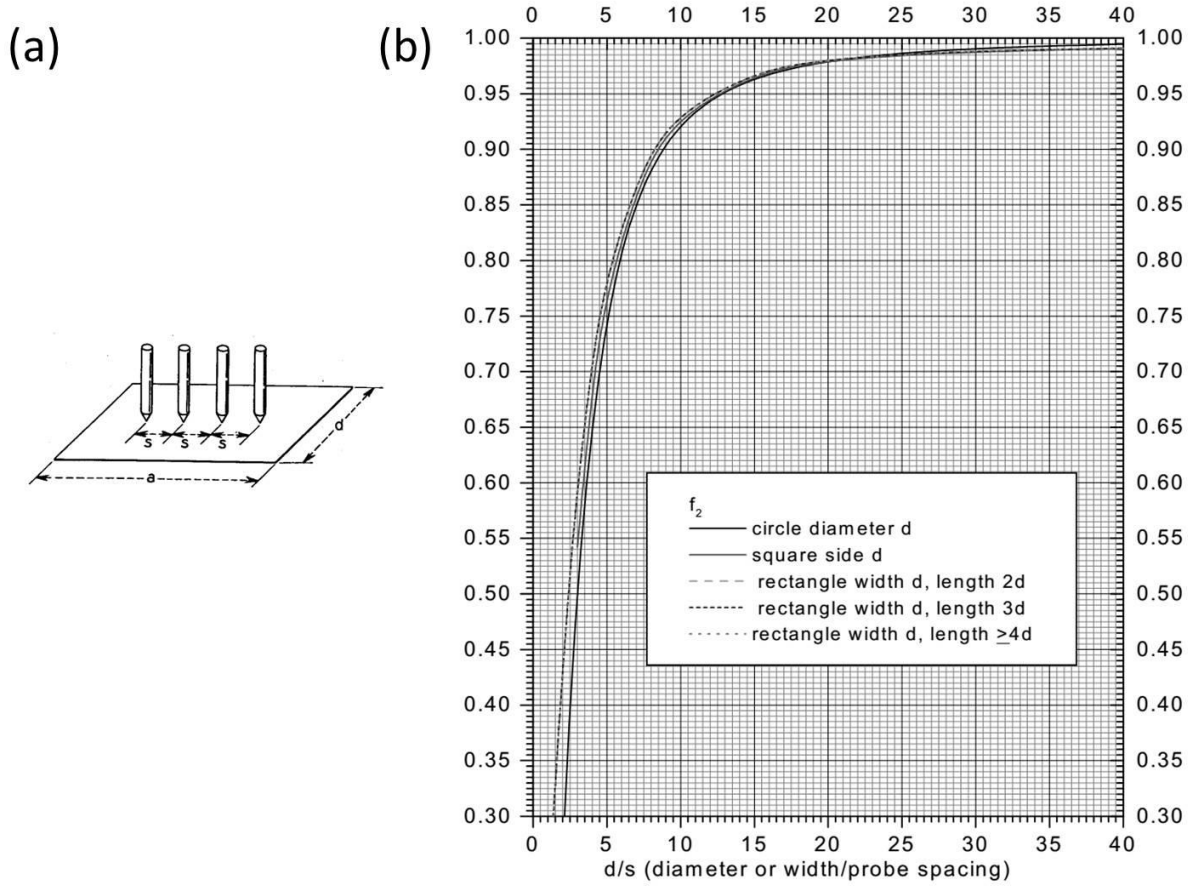

Figure 5.1. Taken from reference [52, 53]. (a) The schematic configuration for the four point measurement for a finite thin film. (b) The corresponding correction factor f_2 for the calculation of the sheet resistance with different diameter-spacing ratios.

For our ultrathin SVO films, the sample thickness is negligible compared to the probe spacing which will give f_1=1. The f_2 correction factor can be looked up from the chart displayed in Figure 5.1 (b) once the sample size and probe spacing are measured.

By using the method stated above, we have measured and plotted out the sheet resistance and the corresponding bulk resistivity of a series of SVO films with thickness ranging from 3 u.c. to 20 u.c.. The results are displayed in Figure 5.2. The sheet resistance shows an overall increase with decreasing film thickness, which agrees with our expectation that the system is driven

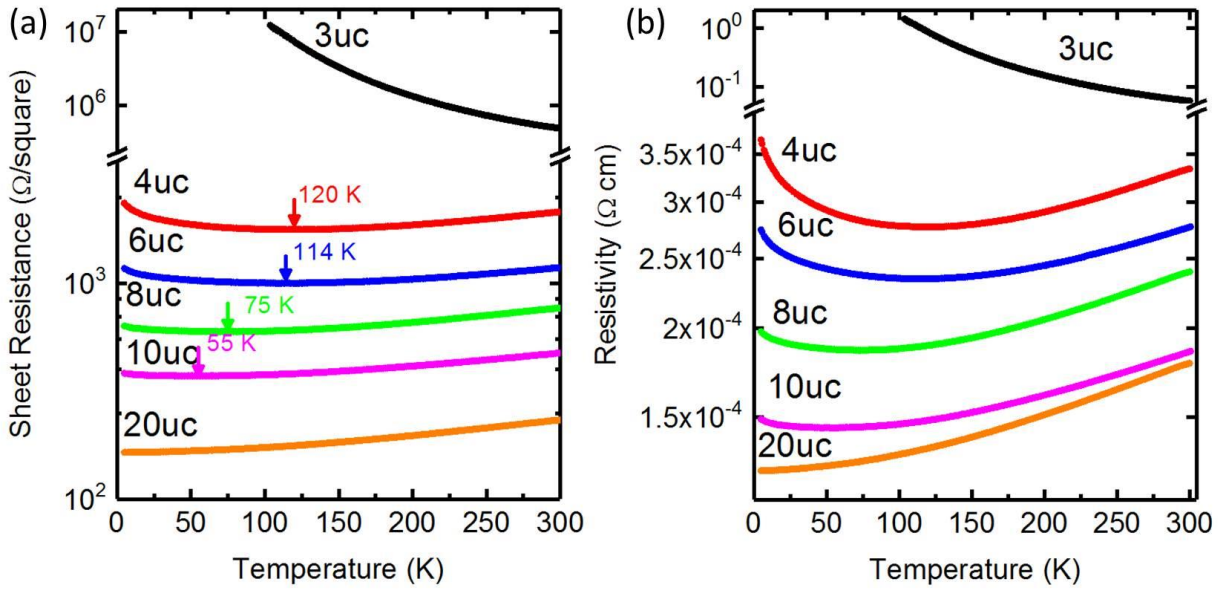

Figure 5.2. (a) The sheet resistance and (b) the calculated resistivity versus temperature for SVO films from 3 u.c. to 20 u.c.. The minima are indicated by arrows and the corresponding temperatures are marked out on the side.

towards MIT with thickness change. The 3 u.c. SVO film clearly shows an insulating behavior with its sheet resistance increasing with decreasing temperature. For the films with thickness between 4 u.c. and 10 u.c., the behaviors of the transport are similar. The sheet resistance first decreases with decreasing temperature start from 300 K, then at some point, it reaches a minima and starts increasing with further temperature decrease all the way to 5 K. As the film thickness increases, the minima temperature is pushed to the low temperature side and finally vanishes at 20 u.c., where a fully metallic behavior is observed. We thus make the claim that we have observed an MIT with a critical thickness of 3 u.c.. The upturn of resistivity (sheet resistance) of the 4-10 u.c. SVO films at low temperatures fits into the picture of weak localization described in

the Anderson theory, in Chapter 6, we will perform more detailed analysis on these transport data and investigated the mechanism behind it.

Also evident in confirming the MIT, there exists a small problem with transport measurements for our SVO films: the measurements are conducted ex-situ, and the SVO thin films are sensitive to degradation in the air. We solved this by depositing a layer of amorphous STO capping on top the SVO films for film protection before taking them out from high vacuum. However, the capping may still cause change to the properties of the film surface. To bypass this problem, we have also performed in-situ measurements on the electronic properties of SVO by UPS and STS, which are discussed in the following two sections.

5.2.2 UPS Measurements

As stated in Chapter 2, UPS is a very useful tool for detecting the electronic band structure. By probing the density of states near the Fermi surface, we will be able to observe the MIT directly if a band gap opens. In Figure 5.3 (a) and (b), we presented our UPS measurements for the valence band and near the Fermi edge for SVO films with 1-4 u.c. and 25 u.c. of thicknesses. The V 3d spectra observed at the Fermi surface show an obvious evolution with the change of film thickness. For help with the analysis, a plot of the intensity at the Fermi edge is shown in Figure 5.3 (c). A drop of the intensity at the Fermi edge is clearly noticeable in the SVO films with decreasing thickness, which eventually evolves into a gap of ~0.4eV at film thickness of 1 u.c., as shown in Figure 5.3 (b). Considering the error bar of the measurements, we can conclude that below 2 u.c. thickness, there is no intensity at the Fermi edge. From 3 u.c., the intensity at

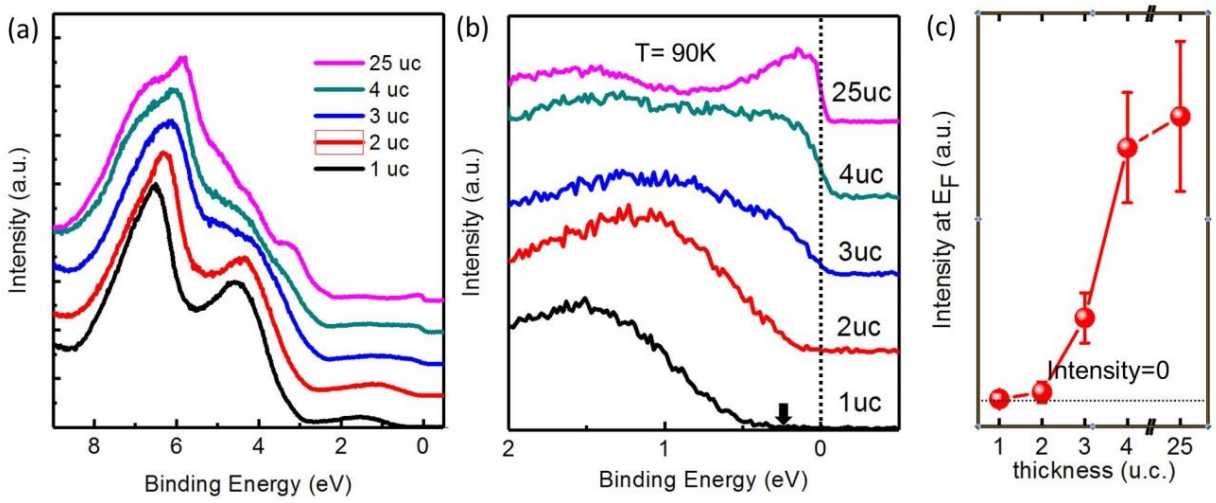

Figure 5.3. (a) The UPS spectra of SVO films with thicknesses of 1-4 u.c. and 25 u.c.. (b) The same plot in (a) zoomed in near the Fermi edge (E_F). (c) The intensity change at the Fermi edge with increasing thickness.

the Fermi edge starts to increase. The intensity at the Fermi edge for 4 u.c. film almost reach to the same level for 25 u.c. one, and the film becomes fully metallic. Our observed spectra are quite consistent with the reported results from Ref. [1], confirming the quality of our samples.

5.2.3 STS Measurements

Besides UPS, we have also taken STS measurements for our SVO films to help investigate the electronic properties on the film surface. We have mentioned in Chapter 2 that the intensity of the STS dI/dV measurements is proportional to the local density states, therefore making the observation of MIT possible. A note of caution must be mentioned here that the STS is a fairly local technique and not meant to detect a large portion of the sample like UPS does; therefore, single STS measurements performed in a limited area cannot represent the properties for the whole film. Nevertheless, this problem can still be solved in a statistical manner by taking

measurements on a reasonable number of points randomly sampled in different locations on the same sample. By comparing and averaging of these results, we will be able to obtain a more general look of the film's electronic properties.

In our experiments, we have measured the SVO films from 1-4 u.c., along with a STO substrate. Both STS current v.s. bias voltage (I-V) curves and the dI/dV curves are obtained with ten or more points are sampled for each film, with about 20 curves taken for each point. Figure 5.4 (a) presents the averaged I-V curves of SVO films of different thicknesses compared with the

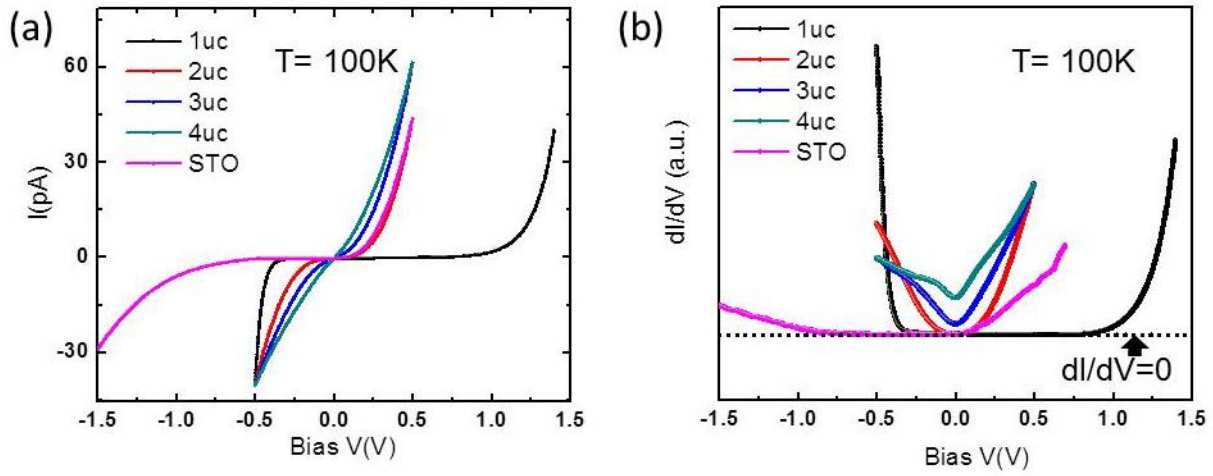

Figure 5.4. (a) Scanning Tunneling Spectroscopy I-V curves for 0.1% Nb-doped STO substrate and SVO films with thicknesses of 1-4 u.c.. (b) dI/dV-V curves for the samples in (c), measured by the lock-in amplifier. All the curves are measured at 100 K.

one from STO substrate. The semiconductor-type curve shape exists in both STO substrate and 1 u.c. SVO film, although the gaps are clearly in different voltage ranges, indicating that the deposition of 1 u.c. SVO drives the n-type STO substrate into p-type. When the film thickness increases to 2 u.c., the gap is no longer visible and the curves become more and more like the

ones for metallic surfaces as the thickness increases. For more accurate analysis, we refer to the dI/dV v.s. bias voltage curves obtained by the lock-in measurements shown in Figure 5.4(b). With the directly proportional relationship between dI/dV intensity and local density of states, based on STS theory [8], dI/dV curves provide us a good indication of the metallicity of the sample. From the dI/dV results, obvious gaps can be observed in the both STO substrate and 1 u.c SVO film; in the 2 u.c. film the gap is clearly closing and yields zero density of states only at zero bias; as the film thickness further increases, the density of states near zero bias also becomes higher, completing the transition from insulating to metallic structure. The observation is consistent with those from transport and UPS, confirming the occurrence of the thickness-dependent MIT with a same critical thickness as reported.

5.2.4 Surface LEED Images

Apart from the thickness-dependent MIT that we have confirmed above, we have also noticed some interesting phenomena from the LEED measurements. We have taken the LEED images for SVO films of different thicknesses, and observed surface structure change occurring at a critical thickness of 2-3 u.c.. As shown in Figure 5.5 (a), the LEED pattern remains 1x1 at 1 u.c. and 2 u.c., while at 3 u.c. weak factional spots start to emerge and beyond 4 u.c. these fractional spots become clearly visible, forming a reconstructed c(2x2) pattern. A plot of the intensity profiles drawn from the images in Figure 5.5 (a) along a line connecting the (-1, 1) and (-0.5, 0.5) spots is shown in Figure 5.5 (b). From the intensity profile we can clearly see that below 3 u.c., there is no intensity at the place where the fractional spots emerge, and above 3 u.c.

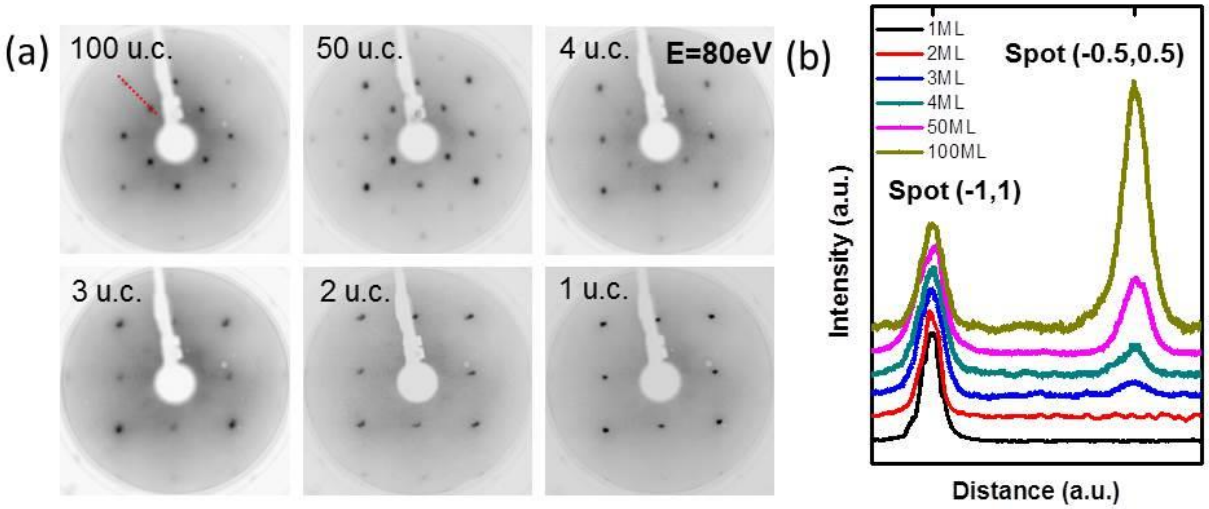

Figure 5.5. (a) Low Energy Electron Diffraction (LEED) patterns of SVO films with thicknesses of 1-4 u.c., 50 u.c. and 100 u.c. at E=80eV. (b) Intensity profiles along the cut line across the integer spot (-1,1) and the fractional spot (-0.5,0.5) from the patterns displayed in (a). The cut line is shown in the 100 u.c. pattern in (a) as the red dotted line.

the fractional spot intensity increase with film thickness. At the thickness of 100 u.c., the intensity of the factional spots is so strong that it exceeds the integer spots by a great amount, which is quite unusual. Since our trials on the LEED-IV refinements are not successfully, we are not able to obtain a possible surface structure model for these SVO films; However, the change of the surface LEED pattern occurring also at 2-3 u.c. hints that there might be some sort of structural change accompanying the MIT. Although we are unable to get any solid proof for this speculation, we still present the observation here in hope that it might become useful for future researchers.

5.3 Discussion and Summary

In this chapter, we have confirmed that a thickness-dependent MIT is indeed occuring in our SVO samples with a same critical thickness of 2-3 u.c. as reported. Combined with our previous observation from STEM/EELS that points to the existence of oxygen vacancies in the first three u.c. of SVO films, we aim to united them under a big theoretical picture--the Anderson localization theory which predicts disorder-induced MIT. We will discuss about this in the following chapter.

Chapter 6. Nature of Metal-Insulator Crossover

6.1 Introduction and Motivation

In the previous chapters, we have investigated the SVO films from both structural and electronic point of view. We have shown by STEM and EELS that there exists oxygen deficiency in the first three layers above the interface, and UPS, STS and transport measurements confirms that the SVO film we grow on STO (001) substrate undergoes a similar thickness-dependent MIT as reported, with the same critical thickness. Now we will test our speculation that the oxygen deficiency we have observed is possibly responsible for inducing the MIT.

In this chapter, we will first present some basic introduction of the long-established theory of Anderson localization and discuss how theory predicts that disorder can induce the MIT in a system. We will then continue to go further on the transport analysis we observed in the last chapter and also present some magnetoresistance measurements and show how oxygen deficiency drives the SVO films to insulating.

6.2 Introduction of the Anderson Localization Theory

This part of the theoretical discussion is mostly based on two very well-written reviews on Anderson localization: one by Kramer and MacKinnon on the general introduction on both localization theory and experiments [56], the other by Lee and Ramakrishnan which mostly focus on theory and the electron-electron correlation effects in disordered systems [57]. In the following sections we plan to address several aspects of the theory introduction. We will first

give a brief review of the history of localization and scaling theory; then we will talk about the weak localization scenario; and last, how electron-electron correlation effects fit in the picture.

6.2.1 General Introduction and History

Being a major part of condensed matter physics, the study of crystalline materials have been done intensively by many physicists since the introduction of band theory. In an ideal crystal, the periodicity of the lattice allows the single-electron Schrödinger equation to be solved with Bloch waves as solutions:

$$\psi(\mathbf{r}) = e^{i\mathbf{k}\cdot\mathbf{r}} \cdot u(\mathbf{r}) \tag{6.1}$$

When the symmetry and atomic information are given, the band structures of a crystal can be calculated. However, in real life, the crystal is never perfect ordered. Defects can exist in many forms from impurities and vacancies to dislocation and grain boundaries. The existence of such "disorder" introduces an additional random potential to the periodic potential. When the disorder is weak, the random potential can be considered as a perturbation to the periodic potential; the electrons can still propagate in the lattice as Bloch waves, but will lose coherency on a scale of the phase coherence length l_ϕ, which is on the same order of the electron mean free path l, as shown in Figure 6.1(a) [56]. In such a case, we name the wave functions "extended states" since they can extend through the whole crystal.

However, when the disorder in a system gets sufficiently strong that the random potential can no longer be treated as a perturbation, the situation becomes completely different. It was first pointed out by P. W. Anderson in 1958 [3] that in the case of strong disorder, the electrons may

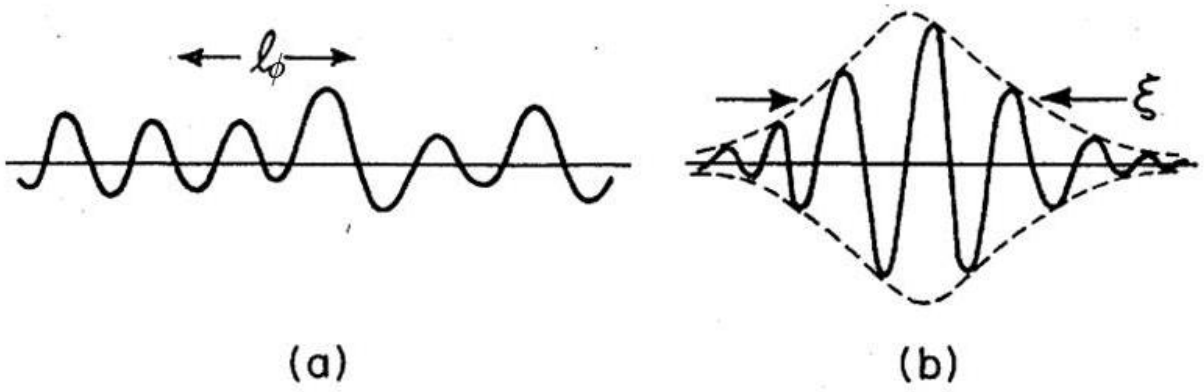

Figure 6.1. Taken from Reference [56]. Electron wave functions of (a) extended states with mean free path l and (b) localized state with localization length ξ.

become localized at the absolute zero of temperature, which means that the amplitudes for the electron wave functions are exponentially decaying from some point in space,

$$|\psi(\mathbf{r})| \sim \exp(|\mathbf{r} - \mathbf{r_0}|/\xi) \tag{6.2}$$

where ξ is the localization length, like shown in Figure 6.1(b). Under such a scenario, the zeroth-order of the eigenstate is bound by the random potential and the admixtures between different orbitals can be treated as perturbation. It is not likely that the admixtures will produce extended states through the linear combinations of localized orbitals because for the orbitals that are close in space and have significant overlaps in the wave functions, their energy are generally very different which makes the perturbation term small; while for the orbitals that are close in energy, they are usually far from each other in space and almost does not overlap. As a result, the wave functions will be exponentially localized and restricted to finite regions in space.

Experimentally, these electrons cannot contribute to transport and the DC conductivity σ_{DC} will vanish at the absolute zero temperature, T=0K, making the system into an insulator.

From the above discussion of the cases of weak and strong disorder, we would naturally assume that for a system with moderate disorder, there exists a mixture of extended states and localized states, which is indeed the case. In 1967, Mott proposed that by changing the energy of the eigenstates the states may change between being localized to being extended. The critical energy that marks this change is called the mobility edge [58]. If the Fermi energy falls in the region with only localized states, the conductivity σ_{DC} will be zero at T=0 K, like in the strong-disorder limit; while if the Fermi level falls in the region with extended states then σ_{DC} will have some finite value and the system will be metallic. Therefore, the mobility edge also marks the transition of a system between being metallic and insulating.

In the mid-seventies of the last century, Thouless and many others began to quantitatively discuss the localization problem and pointed out that when a finite system doubles in size, the nature of the eigenstates, localized or extended, seems to be able to be controlled by the sensitivity to boundary conditions [59-61]. In the paper he stated that the conductance of the finite size sample G is dimensionless and introduce the quantity of dimensionless conductance,

$$g = \frac{G}{e^2/\hbar} \tag{6.3}$$

which is directly related to the sensitivity of the boundary conditions and can be physically measured, thus being the single parameter which controls the nature of a system when its size gets doubled. The theory was further developed into the scaling theory by Wegner in 1976 [62-65]

and later combined with perturbation theory by the famous "Gang of Four" in 1979 [66]. In the following section, we will introduce the scaling theory in more details.

6.2.2 The Scaling Theory

In scaling theory, the basic assumption is that the behavior of the system near the transition between localized and extended states can be sufficiently described by using only one scaling variable, namely the conductance. In order to describe the conductance g(L) of a system with the volume L^d, where d is the dimension, we construct the scaling function β(g) by taking the logarithmic derivative of g(L):

$$\beta(g) = \frac{d(\ln g)}{d(\ln L)} = \frac{L}{g} \cdot \frac{dg}{dL} \tag{6.4}$$

It is assumed that β(g) only depends on the conductance itself and not on the system size L. Later we will discuss more about this function; for the moment let us first take a look at the conductance itself. We have briefly mentioned the a few characterization lengths of the system in the previous introduction section and now we plan to elaborate a bit more for the purpose of understand the conductance g(L) in different regimes.

In a disordered system with size L, the momentum of the electrons will be destroyed after they travel for some distance, mainly due to due to the elastic scattering by the static centers in the lattice; this distance is called the electron mean free path *l*. Beyond *l*, the electron motion is no longer ballistic; therefore *l* defines the lower length cutoff for the diffusive motion of the electron. Now let us consider two extreme limits. When the disorder in the system is very weak, the scattering due to the extra randomness is small and the electrons still behaves very much like

plane-waves. In such a case, one would expect a larger electron mean free path l compared to the Fermi wavelength k_F^{-1}. In the limit of $(k_F l)^{-1} \ll l$, we end up in the metallic regime where the DC conductivity is independent of the size of the system L when the system is large enough and the electron mean free path is well-defined, or to say, $L \gg l$. The Ohm's Law holds true under this limit, which gives for $L \gg l$,

$$g(L) = \sigma L^{d-2} \tag{6.5}$$

In the other limit, we may have a smaller mean free path compared to the electron wavelength λ. In such a case we enter the insulating regime where the electrons are localized. The DC transport under this scenario is contributed by electron hopping between localized states which are energetically close. The envelopes of the localized wave functions are characterized by the localization length ξ. Generally speaking, the localization length ξ is bigger than the electron mean free path l in this regime and therefore we use ξ as a characteristic parameter. For a large enough system $L \gg \xi$, we have a non-Ohmic description of the conductance

$$g(L) \propto e^{-L/\xi} \tag{6.6}$$

Now that we have the two forms of the conductance in different regimes, we can calculate the scaling function $\beta(g)$.

In the metallic regime, the conductance is very large, i.e. $g \gg g_c$, where g_c is a characteristic conductance on the order of π^{-2}. In this case we have

$$\beta(g) = d - 2 \tag{6.7}$$

In the insulating regime, $g \ll g_c$,

$$\beta(g) = \ln(\frac{g}{g_c}) \tag{6.8}$$

Between the two limits or strong localization and Ohmic behavior, we may have an intermediate precursor state which is the weak localization. In this case, a correction to the DC conductivity can be calculated according to the perturbation theory. The results for all three dimensions are given in the following forms:

$$\sigma_{3D}(L) = \sigma_0 - \frac{e^2}{\hbar\pi^3}(\frac{1}{l} - \frac{1}{L}) \tag{6.9a}$$

$$\sigma_{2D}(L) = \sigma_0 - \frac{e^2}{\hbar\pi^2}\ln(\frac{L}{l}) \tag{6.9b}$$

$$\sigma_{1D}(L) = \sigma_0 - \frac{e^2}{\hbar\pi}(L - l) \tag{6.9c}$$

Correspondingly, a correction of a g^{-1} term is added to the scaling function

$$\beta(g) = d - 2 - \frac{a}{g} \tag{6.10}$$

where in this case, g is defined as $\sigma(L\pi)^{d-2}$.

Given the above equations, the behavior of the scaling function β(g) can be obtained on the plausible assumptions that β(g) is monotonic and continuous. The results are shown in Figure 6.2 [66].

In one dimension, i.e. d=1, β(g) is always negative and decreases with decreasing conductance. In other words, as the system size keeps increasing, the conductance g will decrease to zero at a faster and faster pace. All states are localized under this scenario.

In two dimensions, again we always have β(g) < 0; so when the system gets big enough, it will always become localized. In the weak-disorder limit the localization length can be estimated based on the perturbation theory as

$$\xi \sim l e^{\frac{\pi}{2} k_F l} \tag{6.11}$$

We can see that in this case the localization length shows an exponentially dependence on the mean free path. This means that although there are no truly extended states in two dimensions,

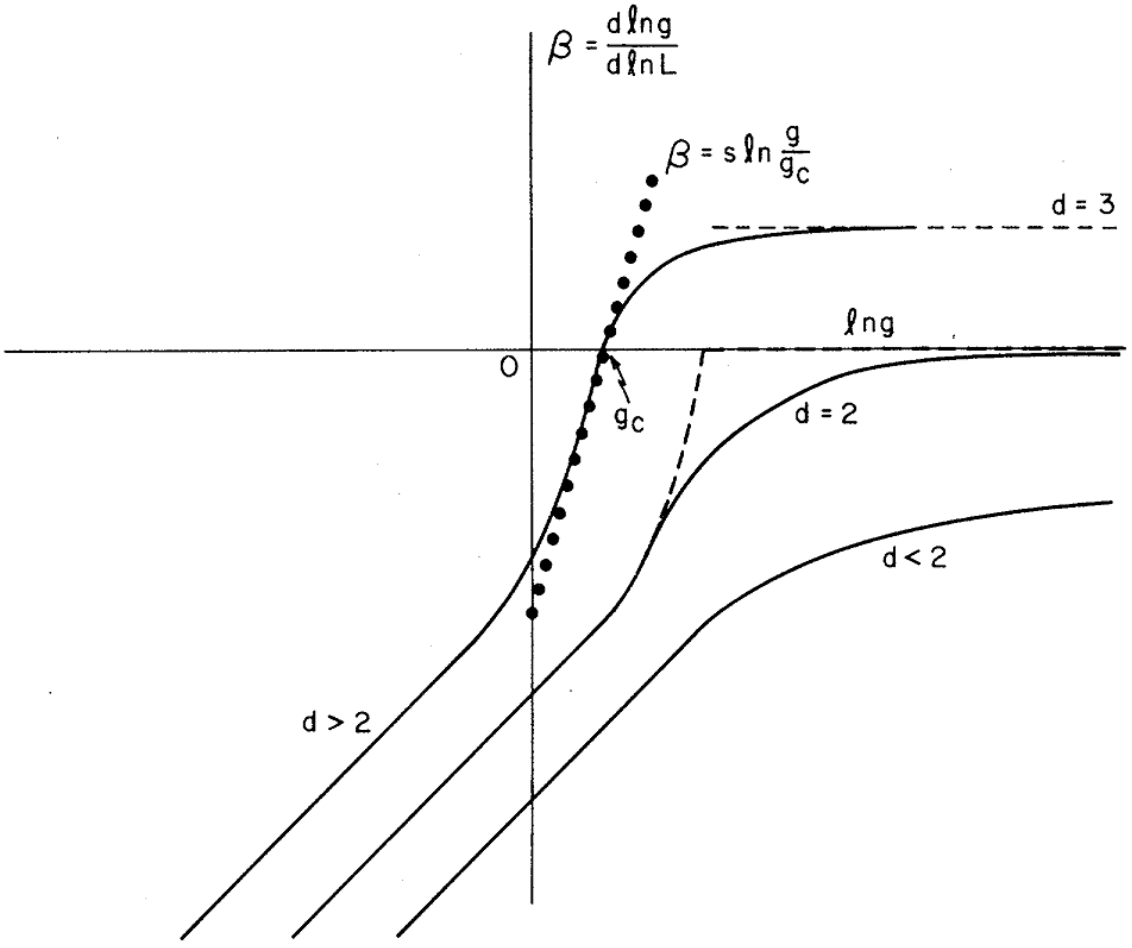

Figure 6.2. Taken from Reference [66]: Plot of the scaling function β(g) v.s. lng for different dimensions.

for a system with large conductance and weak disorder, the localization length can be astronomical and the corresponding effects will be difficult to observe from experiments. Later in

the next section, we plan to have some more detailed discussion about the 2D weak localization case since this is of major relevance to our study.

In three dimensions, we have positive β(g) on the large conductance side and negative β(g) on the small conductance side, which means that depending on the initial g_0 we start with, the conductance either decreases or increases as the system sizes increases, ending up on one limit of the β(g) curve. Macroscopically, this means that the system can be either metallic or insulating. The point where β(g) passes zero therefore marks a change of regime, i.e. the metal-insulator transition. Compared to the previous cases, the three dimensions is the only case where a disorder-induced MIT can occur in the system. However, this is already beyond the scope of our study and we will not give more discussion about this scenario.

One thing to note is that the whole discussion above is based on the simplified assumptions that there are no electron-electron correlations or magnetic scattering in the system. With electron correlations, thing get more complicated and extra corrections have to be made. We will also talk about this in more details later in this chapter.

6.2.3 Weak Localization

Now that we have discussed the basic predictions of the scaling theory, let us come to the regime of weak localization which is most closely related to our experimental observations, by which we mean the upturn of resistivity at low temperatures in the 4-10 u.c. ultrathin SVO films that we presented in the last chapter. We know from the arguments from the previous section that weak localization is some sort of intermediate state between the metallic and insulting limits

which is induced by a moderate amount of disorder. Now we would like to go deeper into the discussion about the nature of this effect and how it caused the resistivity increase at low T.

To understand the origin of weak localization, we have to come back to the quantum mechanical nature of transport. We have mentioned about that in a system with disorder the nature of electron motions is diffusive, which we can understand as a random walk controlled by the random scatterings from the impurities. The transport process is related to the probability of an electron to propagate in space between point A and point B. Classically, it is assumed that the total probability is simply the sum of the probabilities of the paths between A and B; but in quantum mechanics, this total probability for an electron to move from a point A to a point B is calculated by summing up the amplitudes rather than the probabilities of the paths. This will result in a number of extra interference terms caused by the self-intersecting paths and increase the probability of the electron to go around in loops, thus increasing the resistivity. The process is also called coherent backscattering, which controls the weak localization effect. In low dimensions, due to the dimensionality restriction, it is much more likely to find self-intersecting paths compared to the higher dimensional case, thus, the weak localization effect is much stronger in 1D and 2D.

Experimentally, in 2D, the weak localization takes form as the logarithm decrease of the conductivity of thin metallic films with decreasing temperature as T approaches the absolute zero. All the discussion we have had so far from the previous part is still limited to zero temperature and we have to make some modification to the theory to predict the temperature dependent

behavior of a disorder system. In his 1977 paper, Thouless pointed out that [67] the quantum interference that accounts for the weak localization will be reduced by the random fluctuations in the time evolution of an electronic state caused by inelastic scattering. Assume that an electron state has a lifetime of τ_i before its phase again gets destroyed by the inelastic scattering, then the distance that the electron diffuses within τ_i can be calculated as

$$L_{in} = \sqrt{D\tau_{in}} \tag{6.12}$$

where D is the diffusion constant, τ_{in} is the lifetime of the electron state we talked about and is temperature-dependent. L_{in} denotes the mean distance between two successive inelastic scattering processes that the electron undergoes, which serves as a cutoff length for the quantum interference. Therefore, the temperature-dependent $L_{in}(T)$ can be used as a system size in the original T=0 theory. Suppose p is a parameter characterizing the scattering mechanism and $\tau_{in} \propto T^{-p}$, we can then obtain

$$L_{in} = aT^{-p/2}, \tag{6.13}$$

By plugging this expression back into Equation 6.9a-c, we get

$$\sigma_{3D}(T) = \sigma_0 + \frac{e^2}{\hbar\pi^3}\frac{1}{a}T^{p/2}) \tag{6.14a}$$

$$\sigma_{2D}(L) = \sigma_0 + \frac{p}{2}\frac{e^2}{\hbar\pi^2}\ln(\frac{T}{T_0}) \tag{6.14b}$$

$$\sigma_{1D}(L) = \sigma_0 - \frac{e^2}{\hbar\pi}T^{-p/2} \tag{6.14c}$$

and now we have the formula for temperature-dependent behaviors of conductivity. Later in this chapter, we will apply these to our experimental data for test. However, one thing to note is that

electron-electron interactions/correlations will also result in a lnT correction to the conductivity in 2D [68, 69], which we show in the next section.

The inelastic cutoff length is important for the determination of effective dimensionality when characterizing the system. In the case of a thin film with film thickness t, if $t < L_{in}$, we can view it as a 2D case; otherwise the 3D theory has to be applied. Moreover, since L_{in} is temperature-dependent, for the same film, the change of temperature may also change the behavior with a dimensional crossover at some temperature $T_{crossover}$. It has also been proposed by a few scientists that the electric field can also provide a cutoff length [70-72]; however, it is beyond the scope of our study and therefore will not be discussed here.

6.2.4 Electron-Electron Correlation Effects and Magnetoresistance (MR)

The discussion we have had above is based on non-interacting disordered system; with electron interactions/correlations the behavior of the disordered system gets more complicated. There have been many studies from the 1980s dealing with disordered Fermi liquid [73-83]. We will not address to the detailed calculation except presenting the experimental prediction here. In a 2D system, the electron correlations give rise to a correction to the conductivity which is also proportional to lnT, so that in the correlation picture, the conductivity can be rewritten with an additional Coulomb term,

$$\sigma(T) = \sigma(T_0) + \frac{1}{2}\frac{e^2}{\hbar\pi^2}[\alpha p + (1 - \frac{3}{4}\widetilde{F_\sigma})]\ln(\frac{T}{T_0}) \quad (6.15)$$

where p is the parameter that determines the dominant inelastic relaxation mechanism; usually p=1 for electron-electron scattering and p=3 for electron-phonon scattering.

Since both localization and electron-electron correlation effects contribute to a $\sigma \propto \ln T$ behavior in 2D, we need to find a way to distinguish the two effects. It has been proposed that this problem can be solved through the application of an external magnetic field. It has been proposed by Altshuler et al [84] that a uniform magnetic field will break the time-reversal symmetry and suppress the localization effect by destroying the phase coherence of the closed path electron waves, thus giving rise to a negative magnetoresistance experimentally. Later it was found by the quantitative studies of Hikami et al [73] on the MR for 2D disordered systems that in the presence of spin-orbit scattering a positive magnetoresistance may also be possible. However, while both negative and positive MR can happen for a disordered system; electron correlations, on the other hand, always lead to a positive MR.

When neglecting the Zeeman splitting, the conductivity of a 2D disordered system in a magnetic field with can be expressed by a modified version of the Maekawa-Fukuyama formula [85],

$$\frac{\sigma(H)-\sigma(0)}{\frac{e^2}{\pi h}} = \alpha\left\{-\Psi\left(\frac{1}{2}+\frac{H_e}{H}\right)+\frac{3}{2}\Psi\left(\frac{1}{2}+\frac{H_{in}+H_{so}}{H}\right)-\frac{1}{2}\Psi\left(\frac{1}{2}+\frac{H_{in}}{H}\right)-\left[\ln\left(\frac{H_{in}+H_{so}}{H_e}\right)+\frac{1}{2}\ln\left(\frac{H_{in}+H_{so}}{H_{in}}\right)\right]\right\}+AH^2 \quad (6.16)$$

where Ψ is the digamma function, α=1 for weak localization, A is constant, and H_e, H_{in}, H_{so} are effective fields related to the elastic, inelastic and spin-orbit relaxation times respectively. The forms of H_e, H_{in} and H_{so} are similar, given by

$$H_e=h/(8\pi eD\tau_e)=h/(8\pi eL_e^2) \quad (6.17a)$$

$$H_{in}=h/(8\pi eD\tau_{in})=h/(8\pi eL_{in}^2) \quad (6.17b)$$

$$H_{so}=h/(8\pi eD\tau_{so})=h/(8\pi eL_{so}^2), \quad (6.17c)$$

where τ_{in}, L_{in} are inelastic relaxation time and the inelastic cutoff length we mentioned in the previous section and τ_{so}, L_{so} is defined similarly for spin-orbit scattering. Note that when we have both inelastic scattering and spin-orbit scattering, when we make the argument about the dimensionality of the system, we have to be careful about which is the more dominating effect and using the correct cutoff length. The inelastic cutoff length can also be used for determining the p-parameter for scattering mechanism, according the Equation 6.13. However, when we add the existence of electron correlations to this picture, an extra Hartree term correction will be introduced which predicts lnH behavior in high field and H^2 behavior in low field [57]. This makes the experimental interpretation much more difficult. Later we shall see this when we present our MR data in the next section.

6.2.5 Strong Localization

Till now, we have discussed about the weak localization and the effects due to correlations, but what about the case of strong localization? A classical theory to treat the transport behavior in the strong localization regime is the variable-rang hopping (VRH) model proposed by Mott [86]. Earlier in this chapter, we have mentioned that the transport in a strongly localized system is still possible by the hopping between localized states that are spatially far apart while being energetically close under thermal activation. Mott proposed that the hopping probability p between the states is given by

$$p \propto \exp(-\alpha R - \beta\Delta) \tag{6.18}$$

where R and Δ are respectively the spatial and energetical distance between the localized states, α is proportional to the inverse of the exponential decay length of the states, and β is $(k_BT)^{-1}$, with k_B being the Boltzmann constant and T being the temperature. In order to get the largest probability, we have to find the relationship between R and Δ. If we assume the localization centers have a homogeneous distribution in a d-dimensional space, then we have

$$\Delta \propto (R^d n(E_F))^{-1} \tag{6.19}$$

From Equation 6.18 and 6.19, we will be able to maximize p at some distance R_{max} by minimizing the part in the exponent. After some algebra, we get $\ln p \propto T^{-1/(d+1)}$. Since the DC conductivity is also proportional to the hopping probability p, we can express it as

$$\sigma = \sigma_0 \cdot \exp(-(\frac{T_0}{T})^{1/(d+1)}) \tag{6.20}$$

which is also known as the famous Mott $T^{-1/4}$ law in 3D case (d=3). This is also part of the theory that we plan to test with our data in the next section.

6.3 Experimental Study of disorder in SVO Films

Now that we finished the discussion on theory, let us come back to our experimental data and see how well they fit in the picture. This is discussed from two major aspects: transport and MR data. We will show that the transport data is consistent with the theoretical predictions for a system with both disorder and electron correlations; and the competition of the two mechanisms can be seen from the MR data. By introducing extra oxygen vacancies into the system, we can drive the system into insulating state.

6.3.1 Transport

We will start with some more detailed analysis of the transport data we have presented in the last chapter. In Figure 5.4, we have shown that the thickness-dependent MIT is indeed observed in the SVO transport data with a critical thickness of 3 u.c.. For SVO films between 4 u.c. and 10 u.c., the upturn for resistivity in the low temperatures are clearly visible and therefore these films fall into the weak localization regime. For 3 u.c. and 20 u.c. SVO film respectively, the insulating and metallic behavior is observed for all temperature range. We will analyze each of these cases separately below.

6.3.1.1 The Insulating Regime

The VRH model can be used to describe the strong localization behavior. By rewriting Equation 6.19, we get

$$\ln\sigma = A + B \cdot T^{-1/(d+1)} \tag{6.21}$$

where σ is the conductance, d is the dimension, T is the temperature, and A and B are constants. In our case of ultrathin films we have d=2, thus a linear relationship of the logarithm of the conductance and $T^{-1/3}$ is expected. In Figure 6.3, we present the fitting trials we have performed on our 3 u.c. SVO transport data with different models. We first tested the fitting with the simply thermal activation model where we expect $\ln\sigma \propto 1/T$ according to the Arrhenius equation, the result is shown in Figure 6.3 (a). We can see that in the 1/T Arrhenius plot there is an obvious curvature in the data, indicating the failure of the linear fitting. We then tested the strong localization VRH model both in 3D and 2D, and the results are shown in Figure 6.3 (b) and (c).

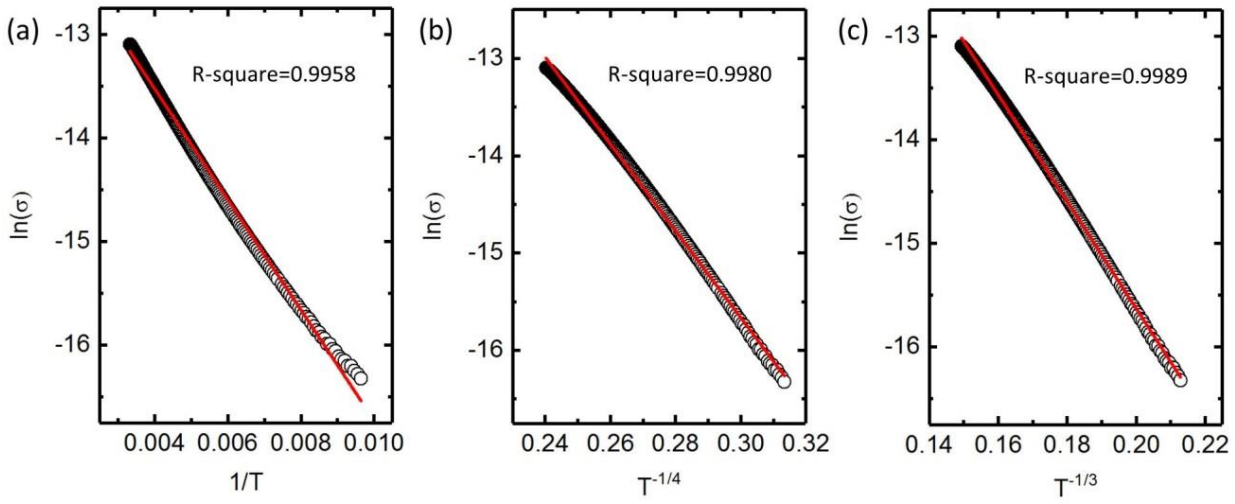

Figure 6.3. Fitting of the transport data of the 3 u.c. SVO film with different test models. (a) The thermal activation model lnσ v.s. 1/T; (b) the 3D VRH model lnσ v.s. $T^{-1/4}$; (c) the 2D VRH model lnσ v.s. $T^{-1/3}$.

The 2D model fitting of lnσ v.s. $T^{-1/3}$ seems to describe the data better compared to the 3D model with a higher R-square value of 0.9989 v.s. 0.9980. It should be noted that the original VRH model applies for low temperature, and our data ranging from 125-300 K does not fit into this category. However, it has also been argued that VRH at high temperature may still be possible due to polaron assisted hopping [87]. Due to the lack to low temperature transport data due to the limited measurement range of the instrument, the thorough interpretation of the insulating 3 u.c. film cannot be obtained; but the good fit of the 2D VRH model indicates that at the high temperature range we have observed, VRH may still be our main conduction mechanism, thus supporting the 2D strong localization picture.

6.3.1.2 The Metallic Regime

The 20 u.c. SVO film we have grown already lands in the metallic regime and we have fitted its resistivity data using the following formula:

$$\rho=\rho_0+AT^2 \quad (6.22)$$

As shown in Figure 6.4 (a), the good fit between the experimental data and the quadratic curve indicates a Fermi liquid behavior as predicted for correlated system which is also observed in the bulk SVO and other TMOs [27, 88-92]. For the 4-10 u.c. films in the weak localization regime, the metallic part of the transport data also shows the same quadratic behavior, as shown in the resistivity v.s. T^2 plot in Figure 6.4 (b). The fitting parameters for all five films are summarized in Table 6.1 below.

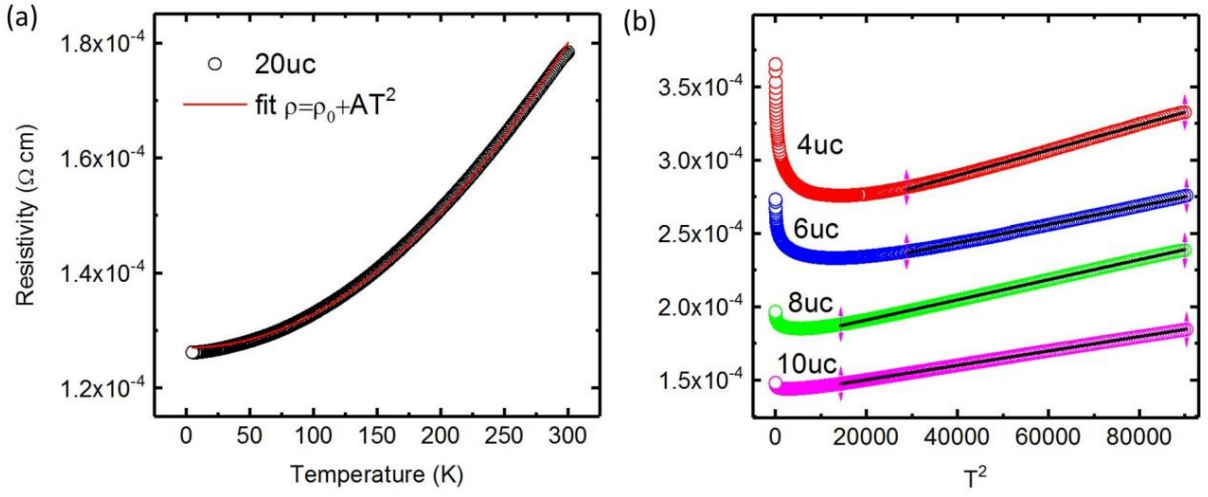

Figure 6.4. Fitting of the transport data of the 4-20 u.c. SVO films to the Fermi-Liquid model $\rho=\rho_0+AT^2$ in the metallic regions. (a) 20 u.c. SVO film, from 5-300 K; (b) 4-6 u.c. SVO film, from 170-300 K; and 8-10 u.c. SVO film, from 120-300 K.

From the table above, an increase of the residual resistivity ρ_0 with film thickness is observed as expected, while the coefficient A does not show obvious trend with the change of thickness. The fitting parameters for all our SVO thin films presented in this section are

consistent with those reported for the SVO bulk with ρ_0 ranging from 6.0 x 10^{-6} Ω cm to 3.0 x 10^{-2} Ω cm and A ranging from 4.0 x 10^{-10} Ω cm/K^2 to 6.0 x 10^{-8} Ω cm/K^2 [27, 89, 93, 94].

Table 6.1. Fitting parameters of resistivity of the 4-20 u.c. SVO films to the quadratic Fermi liquid model $\rho=\rho_0+AT^2$.

Film Thickness	ρ_0 (Ω cm)	A (Ω cm/K^2)	R-square
20 u.c	(1.2696 ± 0.0004) x 10^{-4}	(5.90 ± 0.01) x 10^{-10}	0.9992
10 u.c	(2.561 ± 0.001) x 10^{-4}	(8.61 ± 0.02) x 10^{-10}	0.9989
8 u.c	(2.194 ± 0.001) x 10^{-4}	(6.27 ± 0.02) x 10^{-10}	0.9987
6 u.c	(1.7812 ± 0.0005) x 10^{-4}	(6.866 ± 0.009) x 10^{-10}	0.9997
4 u.c	(1.4125 ± 0.0002) x 10^{-4}	(4.909 ± 0.003) x 10^{-10}	0.9999

6.3.1.3 The Weak Localization Regime

We have shown above that the on both metallic and insulating sides, the behavior of the SVO thin films can fit in the picture describing a disordered correlated system. Now we would like to come to the most important regime of weak localization and analyze the system behavior. From Equation 6.14b, we expect a linear relationship between the conductance and the logarithm of temperature in the 2D weak localization case. In Figure 6.5, the fittings of σ v.s. lnT for 4-10 u.c. films in the low temperature range are displayed with the fitting parameters summarized in Table 6.2; the fitting range for the 10 u.c. film is 5-30 K while for 4-8 u.c. films it is 5-50 K.

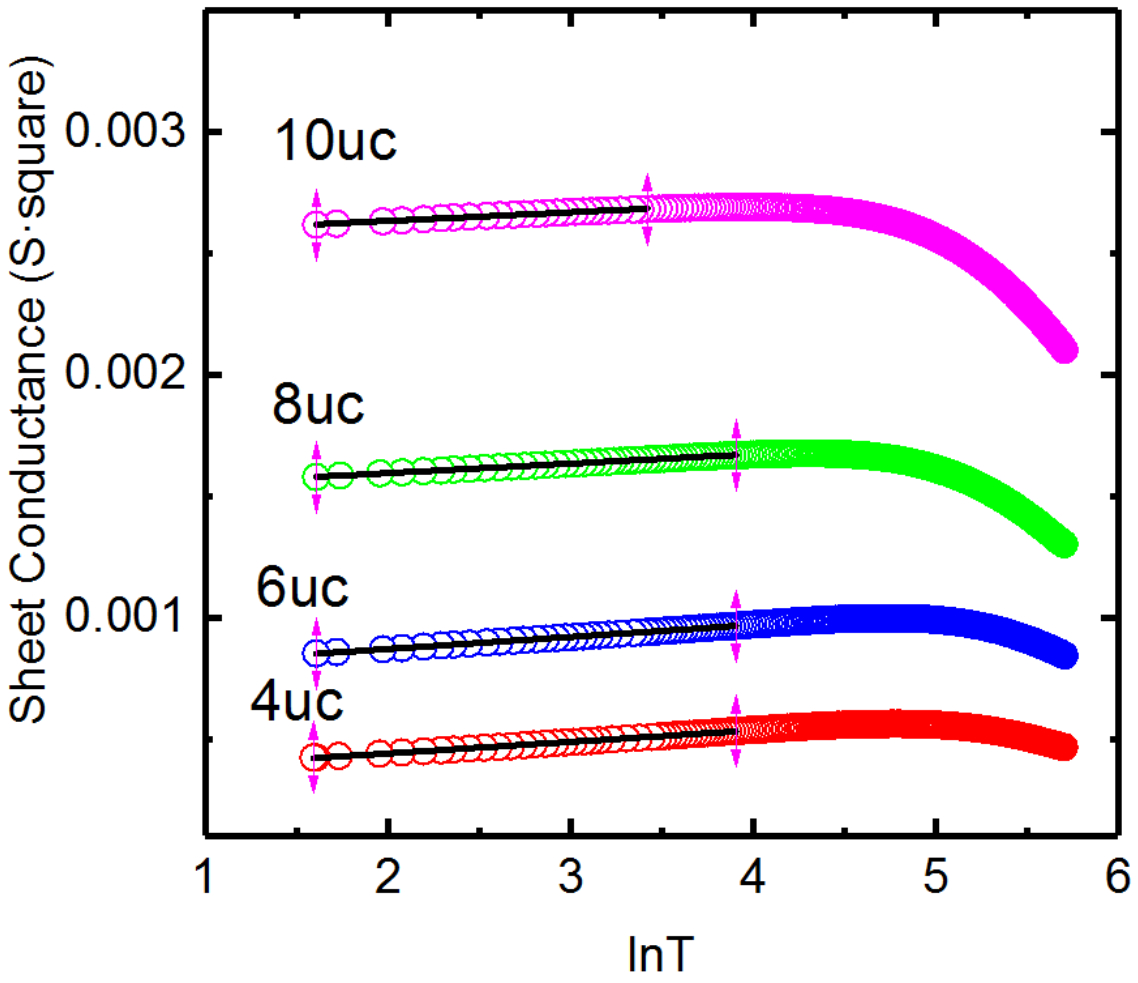

Figure 6.5. Fitting of the conductance v.s. the logarithm of temperature for the 4-10 u.c. SVO films based on the 2D weak localization model. The fitting range is 5-30 K for the 10 u.c. film and 5-50 K for the 4-8 u.c. films.

From Table 6.2, an obvious decrease in the coefficient A with thickness can be observed, which is directly related but not equal to the residual conductance. For the analysis on parameter B, let us come back the original expression of the 2D weak localization model. From Equation 6.14b, we can get $B = \frac{p}{2}\frac{e^2}{\hbar\pi^2}$ and convert the B coefficient to the value of p. The calculations gives p=3.87 for 4 u.c. film, p=4.04 for 6 u.c. film, p=3.18 for 8 u.c. film and p=2.89 for 10 u.c.

film. We have stated before that the value of p dependents on the inelastic scattering mechanism. If p=1, the main mechanism is electron-electron collisions; while p=3 indicates electron-phonon scattering [57]. Our values of p do not seem to be in very good agreement with this prediction. As we may recall, the electron-electron correlations will also give rise to a lnT behavior in the conductance at low temperature, and this correlation effect is additive to the effect caused by disorder. Therefore, we can conclude that in our SVO films, the conductance is not only attributed from disorder; the correlation effect must have also played a role. But which effect is more dominating calls for further investigation.

Table 6.2. Fitting parameters of the conductance v.s. the logarithm of temperature for the 4-10 u.c. SVO films based on model $\sigma=A+B\ln T$.

Film Thickness	A (S·square)	B	R-square
4 u.c	$(3.465 \pm 0.008) \times 10^{-4}$	$(4.76 \pm 0.03) \times 10^{-5}$	0.9988
6 u.c	$(7.724 \pm 0.004) \times 10^{-4}$	$(4.97 \pm 0.01) \times 10^{-5}$	0.9996
8 u.c	$(1.520 \pm 0.002) \times 10^{-3}$	$(3.913 \pm 0.007) \times 10^{-5}$	0.9998
10 u.c	$(2.560 \pm 0.001) \times 10^{-3}$	$(3.56 \pm 0.04) \times 10^{-5}$	0.9983

To make sure that we are not messing up with the system dimension when we analyze the data, we have further checked it by trying to fit the conductance to the 3D weak localization model where $\sigma \propto T^{p/2}$ is expected. Since the p-values we have obtained are close to the electron-phonon scattering case, we have used p=3 for the fitting. The results are displayed in

Figure 6.6. For all four cases, the low temperature side data shows obvious deviation from the fitting, with R-square values ranging from 0.84 to 0.87, apparently indicating the failure of the 3D weak localization model.

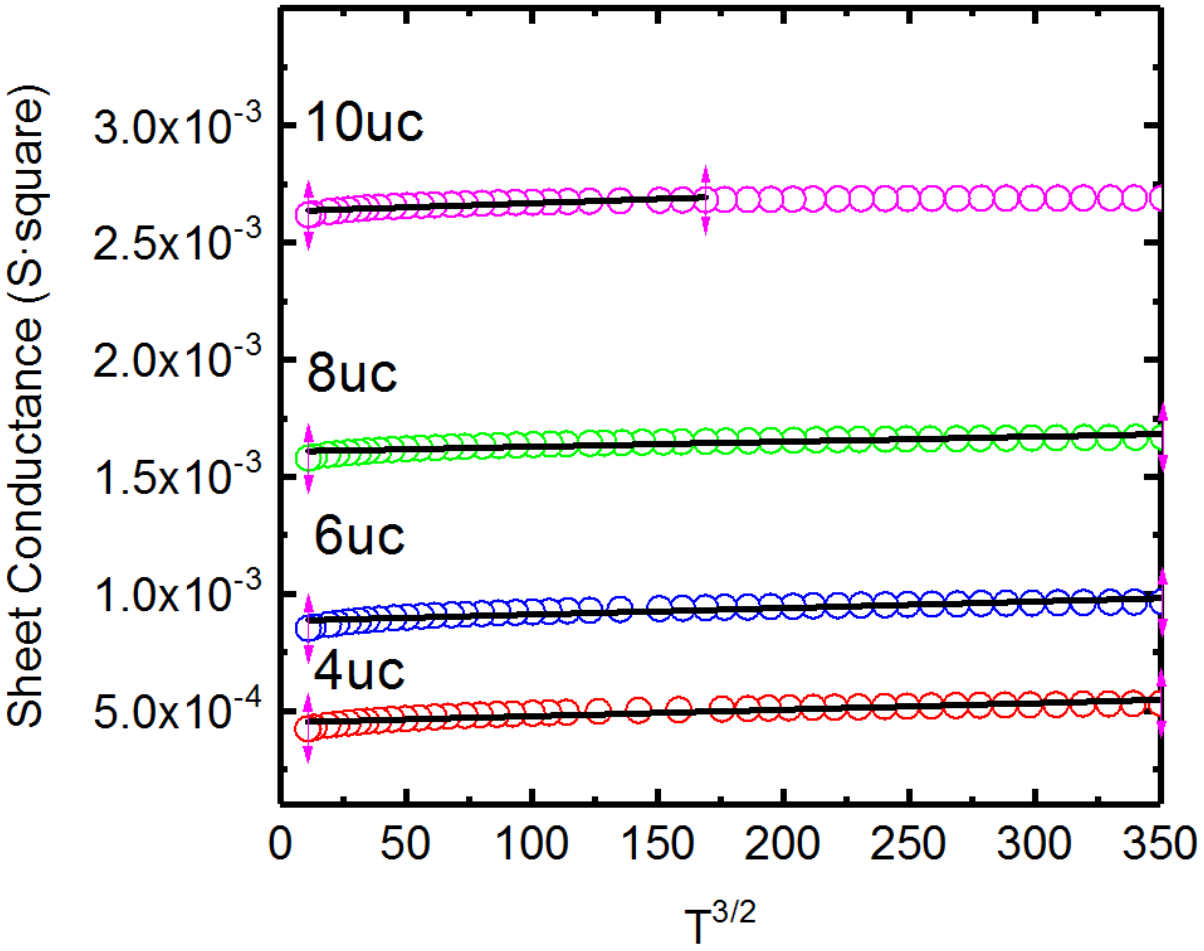

Figure 6.6. The fitting of the conductance v.s. $T^{3/2}$ for the 4-10 u.c. SVO films based on the 3D weak localization model. The fitting range is 5-30 K for the 10 u.c. film and 5-50 K for the 4-8 u.c. films, same for the fitting with the 2D weak localization model.

6.3.1.4 The Effects of the Introduction of the Oxygen Vacancies

Now let us stop and make a brief summary of what we have observed so far: in the insulating regime, the 2D VRH dominates the conduction; in the metallic regime, the behavior of

the SVO thin films fit into the Fermi liquid theory which can be used to describe a disordered system with correlations; in the weak localization regime, the 2D lnT behavior is observed, but as an effect of the coexistence of disorder and correlations. In one word, what we have observed so far all points to the conclusion that neither disorder and correlation effects are negligible when it comes to the contribution to the transport of the SVO thin films, which is not beyond expectation due to the nature of this system, as we stated in the introduction chapter. But as our purpose is to investigate how significant the effect of disorder is in this system, we would like to try and find a way to separate the effect of disorder and correlations. Since the major disorder in our films is oxygen vacancies, we cannot help wondering: what would happen if we deliberately introduce more oxygen vacancies into the SVO thin films? If the disorder-induced localization effect is truly significant, then it is very likely that by introducing extra oxygen vacancies into an originally metallic film, we will be able to drive it to insulating. In fact this is what we did. Since we are already growing the SVO films in vacuum, it is not possible for us to introduce oxygen vacancies into the films during the growth process by tuning down the oxygen partial pressure. Therefore, we have turned to an alternate way by post-annealing the film after growth in vacuum, but under a higher temperature than the growth temperature. With a reasonable annealing temperature and long enough annealing time, we should be able to introduce a significant amount of oxygen vacancies into the SVO thin films.

In Figure 6.7, we present the transport data for three 10 u.c. SVO films, one as grown without any post-annealing, and other two post-annealed under 850˚C for 20 and 40 minutes in

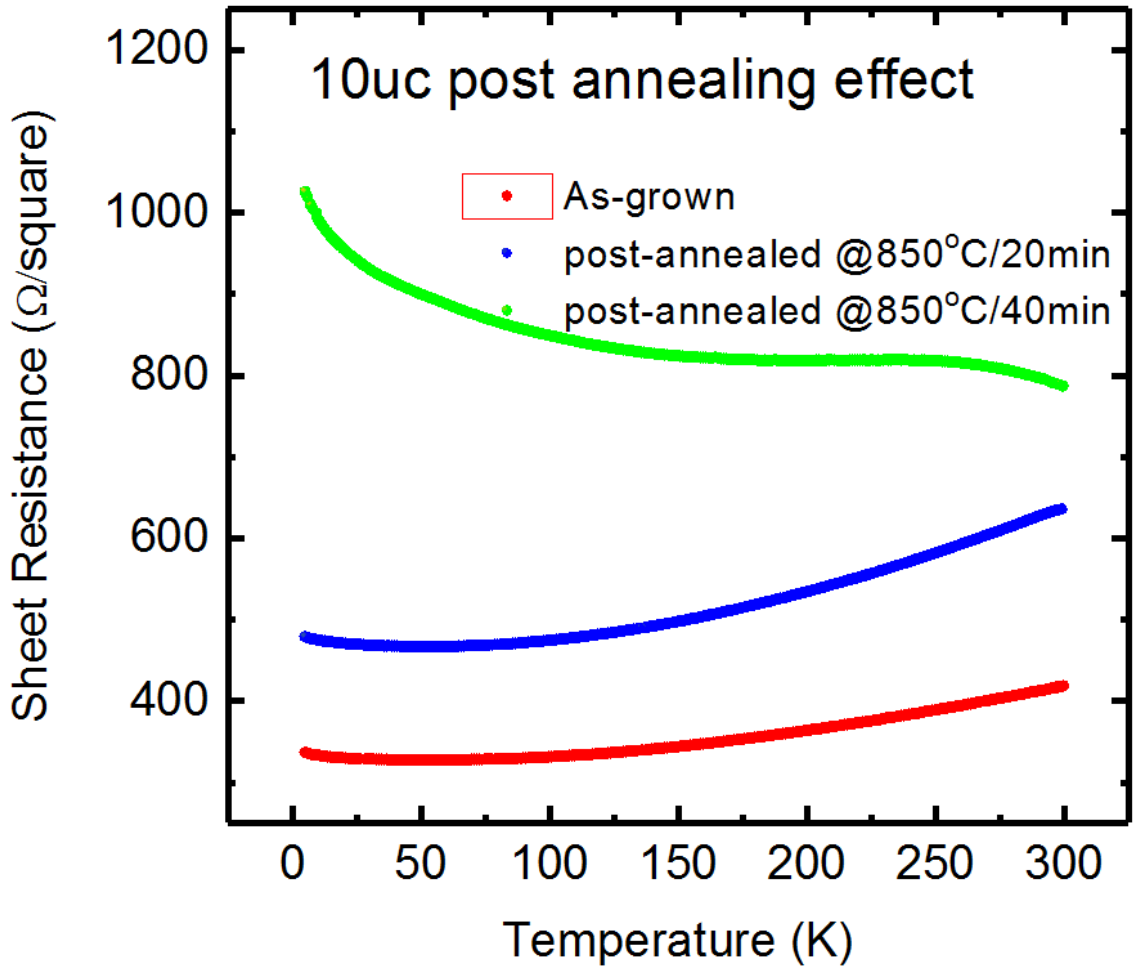

Figure 6.7. The sheet conductance for 10 u.c. SVO films as grown and post-annealed under 850˚C for 20 minutes and 40 minutes, respectively.

vacuum, respectively. We can see that both the 10 u.c. as-grown film and the 10 u.c. film post-annealed for 20 minutes show similar weak localization behavior, while the 10 u.c film post-annealed for 40 minutes has already become insulating. Although it may seem unbelievable that the extra annealing time could make such a significant difference, we can try and offer an explanation for this observation. At the beginning of the post-annealing process, just like in most cases, the atoms will rearrange themselves due to the extra thermal activation and result in a

more ordered film. Once the best order is achieved, the disorder effect resulted from the accumulation of oxygen vacancies becomes more and more significant as the annealing time increases. Eventually, at some point, the disorder finally drives the system to insulating.

6.3.2 Magnetoresistance (MR)

We have shown in the previous section that by introducing more oxygen vacancies, we are able to drive an originally metallic SVO film to insulating. This indicates that disorder caused by oxygen vacancies may be the dominant driving force for MIT, as we predicted. For more support, we have conducted more investigations with the magnetoresistance measurements. To begin with, we have chosen a 4 u.c. and a 6 u.c. SVO film to perform MR measurements on since these films are closer to MIT and show more obvious upturn in the resistivity at low temperatures. We have also tested the MR for the 10 u.c. films, without and with post-annealing, to see if they yield any difference. The results are presented in Figure 6.8 and Figure 6.9.

In Figure 6.8 (a) and (b), we present the MR data for the 4 u.c. and 6 u.c. SVO films. We can see that for the 4 u.c. film, an overall negative MR is observed below 7 K, which is consistent with the prediction that the disorder, rather than electron correlations, is a more dominating factor for the transport behavior. As the temperature increases, the cutoff provided by the temperature becomes more significant than that provided by the field, so the negative MR is no longer observed. However, we have also noticed that in the regime where negative MR exists, a slight positive magnetoresistance can be seen at low field despite the overall negative trend. This can be explained with the consideration of the spin-orbit effect, which has a smaller effective

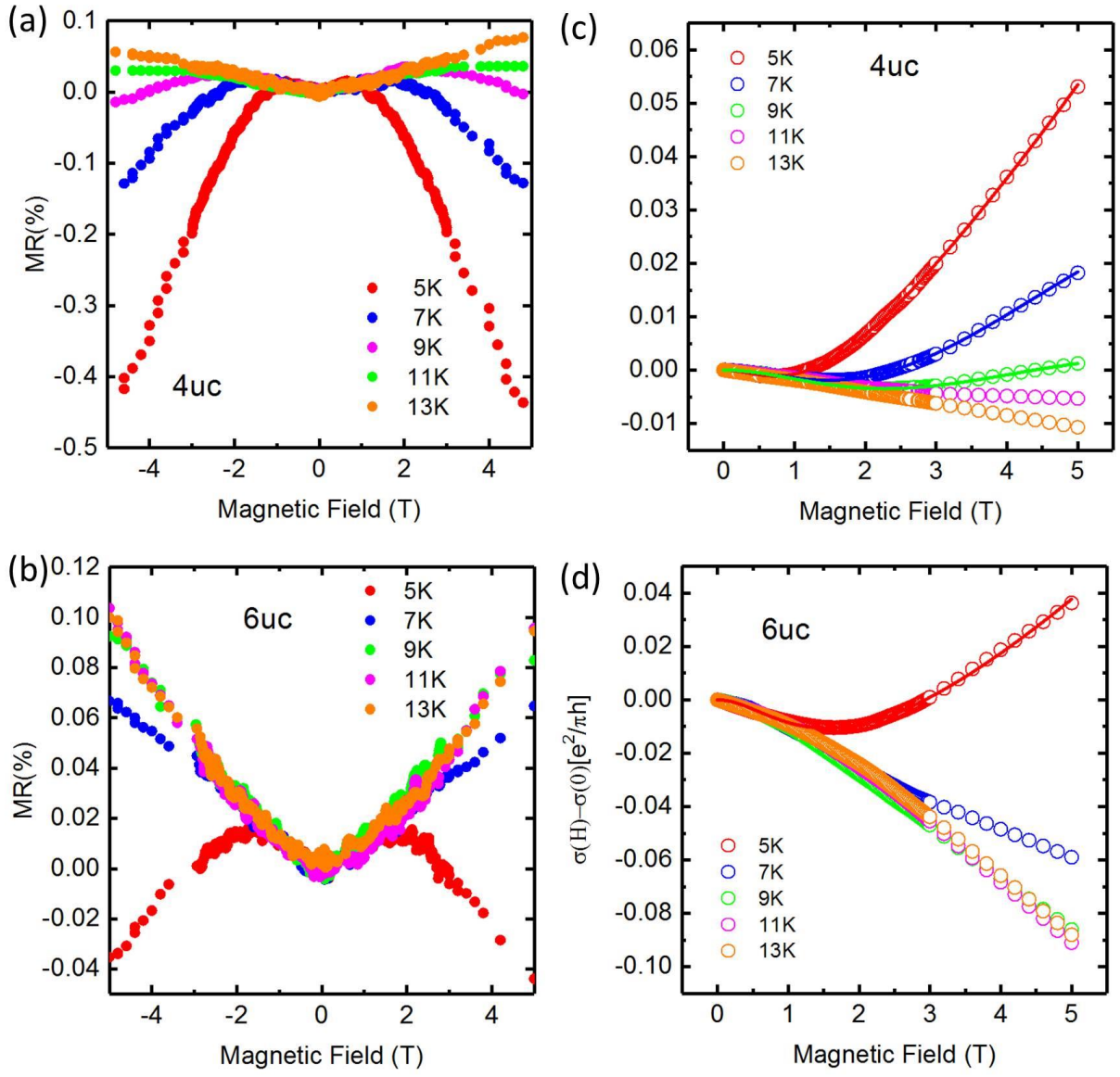

Figure 6.8. (a-b) The field-dependent MR data at different temperatures for a 4 u.c. and a 6 u.c. SVO films, respectively. The magnetic field is applied in the perpendicular direction to the film plane. (c-d) The magnetoconductance the same films as a function of the magnetic field under different temperatures. The solid lines are the fitting curves based on the model depicted in Equation 6.16.

field H_{so} and becomes more significant at low field if H_{so} and H_{in} are comparable. This effect is also seen for the 6 u.c. SVO film. At 5 K, the MR for 6 u.c. film shows strong competition between weak localization and spin-orbit scattering and a smaller absolute value for MR

compared to the 4 u.c. film. Also, above 5 K the negative MR can no longer be seen in the 6 u.c. film, while for the 4 u.c. film this does not happen until 9 K. These results indicated that the disorder-induced weak localization effect is weaker in the 6 u.c film than the 4 u.c., which agrees with our assumption.

In Figure 6.8 (c) and (d), we conducted the fitting of the magnetoconductance based on Equation 6.16 on the 4 u.c. and 6 u.c. curves with the negative MR. This equation takes the effect of spin-orbit scattering into consideration in a weakly disordered system, the extra AH^2 term accounts for the Lorentz force at strong magnetic fields. All of our fitting results give α value equal or close to 1, which is consistent with the theoretical prediction for weak localization α=1. The H_{so} and H_{in} values are summarized in Table 6.3. For all the fitting data, the H_{so} and H_{in} values are comparable, which is consistent with the observation of the competition between the positive and negative MR. From the H_{in} value, the inelastic cutoff length L_{in} can be calculated from Equation 6.17b. The L_{in} value ranges from 11.08~16.16 nm for these two films, which is way beyond the film thickness. Therefore, our arguments for the 2D localization regime hold true. For the curves with positive MR and negative magnetoconductance, similar fitting with the same model can be applied. However, since this model does not include the electron correlations, the quantitative interpretation for the positive MR data will not very accurate, which makes estimate of p-parameter from L_{in} impossible due to the limited number of reliable data points. Therefore, we are not able to determine the major inelastic mechanism for our SVO films from the

experimental data. Nevertheless, the qualitative analysis of MR shows consistency with the speculation that the disorder effect dominates over the electron correlations in our SVO films.

Table 6.3. H_{so} and H_{in} value for 4 u.c. and 6 u.c. films obtained from the fitting to the Maekawa-Fukuyama formula (Equation 6.16).

Temperature	4 u.c.		6 u.c.	
	H_{in} (T)	H_{so} (T)	H_{in} (T)	H_{so} (T)
5 K	0.636	0.315	0.69	0.66
7 K	1.181	0.874	-	-
9 K	1.34	0.93	-	-

Similar MR measurements have been carried out for two 10 u.c. SVO films, one as grown, and one post-annealed at 850˚C for 40 minutes. The results are shown in Figure 6.9. As displayed in Figure 6.9 (a) and (b), the MR for a 10 u.c. film remains positive down to 5 K, while the post annealed film shows negative MR below 6 K. Similarly, calculations of L_{in} can be obtained from the fitting on the magnetoconductance data in Figure 6.9 (c) and (d) which ranges from 15.57~20.29 nm, again satisfying the 2D limit for our argument.

The negative MR observed for the 10 u.c. post-annealed film agrees with the previous prediction that the post-annealing process introduces a significant amount of disorder into the film, which dominates over the electron-electron correlation effects. Combined with the observed MIT induced by the same post-annealing process, the MR data acts as a support for our theory

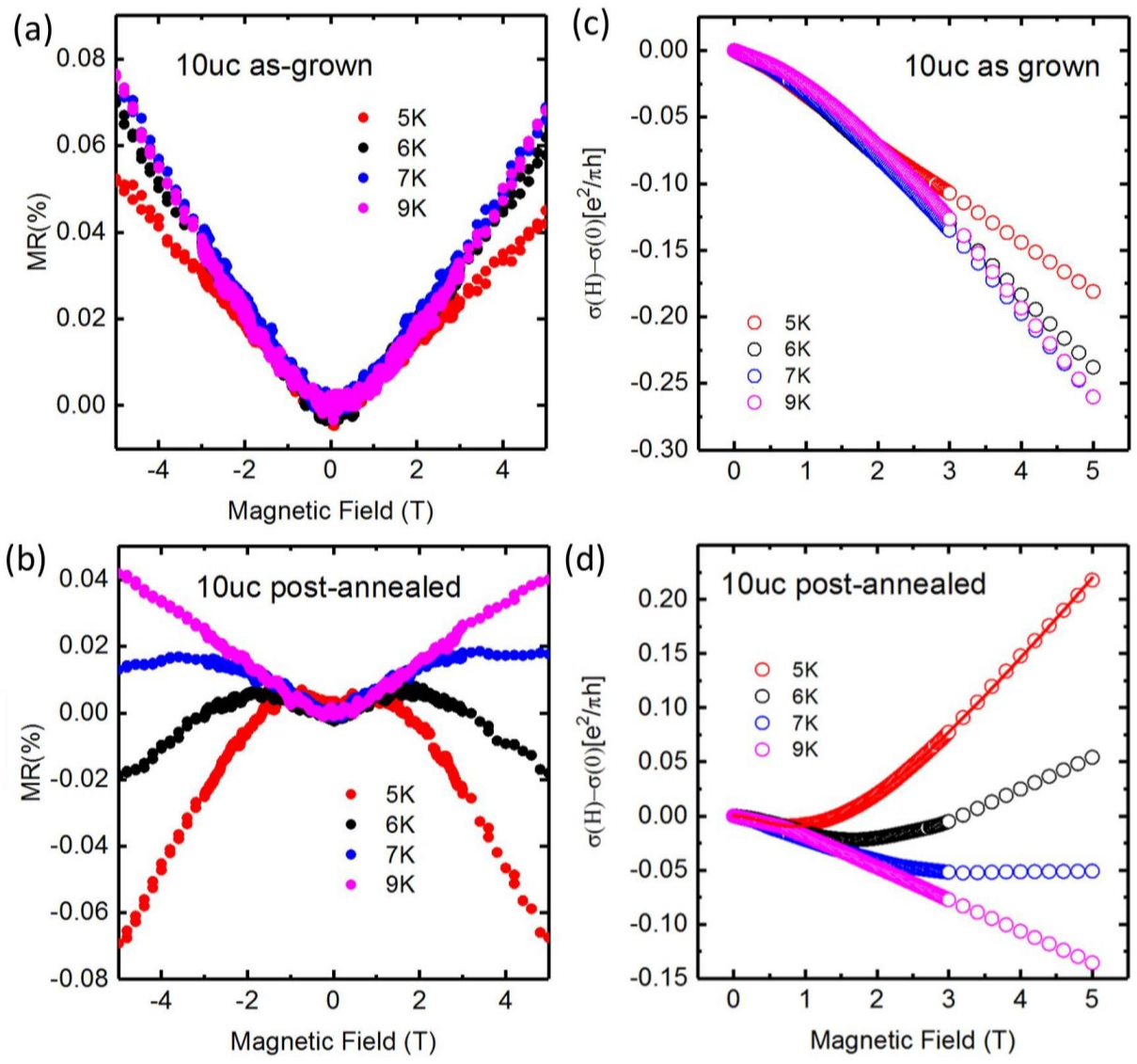

Figure 6.9. (a)-(b) The field-dependent MR data at different temperatures for a 10 u.c. as grown SVO film, and a 10 u.c. SVO films post-annealed under 850˚C for 40 minutes, respectively. The magnetic field is applied in the perpendicular direction to the film plane. (c)-(d) The magnetoconductance the same films as a function of the magnetic field under different temperatures. The solid lines are the fitting curves based on the model depicted in Equation 6.16.

that both disorder and electron correlations exist in the SVO ultrathin films and that disorder makes more significant contribution in the control of the transport behavior, and therefore is responsible for the observed thickness-dependent MIT. However, one other explanation exists for

the MR effects observed in this study: the diffusion of the Ti atoms with reduced oxidation states into the SVO film near the interface may have possibly introduced a small order of magnetism in the film which could also result in a negative MR. This possibility cannot be completed ruled out due to the nature of the film growth, since the intermixture of atoms at the interface due to diffusion is unavoidable. Nevertheless, the possible magnetism is resulted from the reduction of the Ti oxidation states and therefore can still be attributed to the existence of the oxygen vacancies we have deduced in Chapter 4 from STEM/EELS. As a conclusion to this study, we state that our observations are all consistent with the picture of disorder-induced MIT. However, how exactly disorder plays its role remains a very complicated topic calling for more investigation from the future research workers.

6.4 Summary

In the previous chapters, we have characterized our SVO films with various tools on its structural and electronic properties. We have deduced the existence of significant oxygen vacancies in the first three layers of the SVO film near the interface, coinciding with the critical thickness for the thickness-dependent MIT, which is confirmed by the measurements from UPS, STS and transport data. We have made the assumption that the oxygen vacancies as a form of disorder is mainly responsible for the observed MIT, and in this chapter, we have tested our assumption by further analysis of the transport data and MR measurements. The transport data for our SVO films in all three regimes fit into our expected picture of a disordered Fermi Liquid. The MR data is consistent with the prediction that disorder effect is more dominant than

electron-electron correlation effects in the ultrathin SVO films close to the critical thickness. By deliberately introducing more oxygen vacancies into the system, we manage to drive an originally metallic SVO film to insulating one, and the disorder effect is again observed from the MR data after post-annealing, which supports our speculation that disorder is the major contribution behind the thickness-dependent MIT, thus completing the story of this thesis project.

References

[1] M. Imada, A. Fujimori, Y. Tokura, Metal-insulator transitions, Rev. Mod. Phys. **70**, 1039-1263 (1998).

[2] N. F. Mott, The basis of the electron theory of metals, with special reference to the transition metals, Proceedings of the Physical Society. Series A. **62** (7), 416 (1949).

[3] P. W. Anderson, Absence of Diffusion in Certain Random Lattices, Phys. Rev. **109** (5), 1492–1505 (1958).

[4] H. Bethe, Theorie der Beugung von Elektronen an Kristallen, Ann. Phys. (Leipzig) **87**, 55 (1928).

[5] A. Sommerfeld, Zur Elektronentheorie der Metalle auf Grund der Fermischen Statistik, Z. Phys.**47**,1 (1928).

[6] F. Bloch, Bemerkungen zur Elektronentheorie des Ferromagnetismus und der elektrischen Leitfahigheit, Z. Phys.**57**, 545 (1929).

[7] A. H. Wilson, The Theory of Electronic Semi-Conductors, Proc. R. Soc. London, Ser. A. **133**, 458 (1931).

[8] A. H. Wilson, The Theory of Electronic Semi-Conductors. II, Proc. R. Soc. London, Ser. A. **134**, 277 (1931).

[9] R. H. Fowler, An Elementary Theory of Electronic Semi-Conductors, and Some of Their Possible Properties, Proc. R. Soc. London, Ser. A**140**, 505 (1933).

[10] R. H. Fowler, Notes on Some Electronic Properties of Conductors and Insulators, Proc. R. Soc. London, Ser. A**141**, 56 (1933).

[11] J. H. de Boer, E. J. W. Verwey, Semi-conductors with partially and with completely filled 3d-lattice bands, Proceedings of the Physical Society. **49** (4S): 59 (1937).

[12] N. F. Mott, R. Peierls, Discussion of the paper by de Boer and Verwey, Proceedings of the Physical Society. **49** (4S) 72 (1937).

[13] J. Orenstein and A. J. Millis, Advances in the Physics of High-Temperature Superconductivity, Science **288**, 468 (2000).

[14] Colossal Magnetoresistive Oxides, edited by Y. Tokura (Gordon and Breach, London, 2000).

[15] K. F. Wang, J. -M. Liu and Z. F. Ren, Multiferroicity: the coupling between magnetic and polarization, Advances in Physics **58**, 321 (2009).

[16] Kulkarni, A; FT Ciacchi, S Giddey, C Munnings, SPS Badwal, JA Kimpton, D Fini, Mixed ionic electronic conducting perovskite anode for direct carbon fuel cells, International Journal of Hydrogen Energy **37**, 19092-19102 (2012).

[17] J. M. D. Coey, M. Viret; S. von Molnar, Mixed-valence manganites, Advances in Physics **48** (2), 167–293 (1999).

[18] J B Goodenough, Electronic and ionic transport properties and other physical aspects of perovskites, Rep. Prog. Phys. **67**, 1915 (2004).

[19] Michael W. Lufaso and Patrick M. Woodward, Jahn-Teller distortions, cation ordering and octahedral tilting in perovskites, Acta Crystallogr B. **60**, 10-20 (2004).

[20] Mohammad A Islam, James M Rondinelli and Jonathan E Spanier, Normal mode determination of perovskite crystal structures with octahedral rotations: theory and applications, J. Phys.: Condens. Matter **25**, 175902 (2013).

[21] K. Yoshimatsu, T. Okabe, H. Kumigashira, S. Okamoto, S. Aizaki, A. Fujimori, and M. Oshima, Dimensional-Crossover-Driven Metal-Insulator Transition in $SrVO_3$ Ultrathin Films, Phys. Rev. Lett, **104**, 147601 (2010).

[22] L. Zhang, Y. Zhou, L. Guo, W. Zhao, A. Barnes, H.-T. Zhang, C. Eaton, Y. Zheng, M. Brahlek, H. F. Haneef, N. J. Podraza, M. H. W. Chan, V. Gopalan, K. M. Rabe, R. Engel-Herbert, Correlated metals as transparent conductors, Nat. Mater. **15**, 204 (2015).

[23]A. A. Yaremchenko, B. Brinkmann, R. Janssen, J. R. Frade, Electrical conductivity, thermal expansion and stability of Y- and Al-substituted $SrVO_3$ as prospective SOFC anode material, Solid State Ionics **247–248**, 86 (2013).

[24] J. A.Moyer, C. Eaton, R. Engel-Herbert, Highly conductive $SrVO_3$ as a bottom electrode for functional perovskite oxides, Adv. Mater., **25**, 3578 (2013).

[25] C. Eaton, J. A. Moyer, H. M. Alipour, E. D. Grimley, M. Brahlek, J. M. LeBeau, R. Engel-Herbert, Growth of $SrVO_3$ thin films by hybrid molecular beam epitaxy, J. Vac. Sci. Technol.A, **33**, 061504 (2015).

[26] M. Brahlek, L. Zhang, C. Eaton, H.-T. Zhang, R. Engel-Herbert, Accessing a growth window for $SrVO_3$ thin films, Appl. Phys. Lett. **107**, 143108 (2015).

[27] I. H. Inoue et al., Bandwidth control in a perovskite-type $3d^1$-correlated metal $Ca_{1-x}Sr_xVO_3$. I. Evolution of the electronic properties and effective mass, Phys. Rev. B **58**, 4372 (1998).

[28] S. Miyasaka, T. Okuda, and Y. Tokura, Critical Behavior of Metal-Insulator Transition in $La_{1-x}Sr_xVO_3$, Phys. Rev. Lett. **85**, 5388 (2000).

[29] K. Yoshimatsu et al., Metallic Quantum Well States in Artificial Structures of Strongly Correlated Oxide, Science **333**, 319 (2010).

[30] T. Yoshida, M. Hashimoto, T. Takizawa, A. Fujimori, M. Kubota, K. Ono, and H. Eisaki, Mass renormalization in the bandwidth-controlled Mott-Hubbard systems $SrVO_3$ and $CaVO_3$ studied by angle-resolved photoemission spectroscopy, Phys. Rev. B, **82**, 085119 (2010).

[31] E. Pavarini, A. Yamasaki, J. Nuss, and O. K. Andersen, How chemistry controls electron localization in $3d^1$ perovskites: a Wannier-function study, New J. Phys.**7**, 188 (2005).

[32] R. Scherwitzl, S. Gariglio, M. Gabay, P. Zubko, M. Gibert, and J.-M. Triscone, Metal-Insulator Transition in Ultrathin LaNiO3 Films, Phys. Rev. Lett. **106**, 246403 (2011).

[33] W. Brenig, G.H. Dohler, and H. Heyszenau, Hopping Conductivity in Highly Anisotropic Systems, Philos. Mag. **27**, 1093 (1973).

[34] Lin Li, Zhaoliang Liao, Zhenyu Diao, Rongying Jin, E. W. Plummer, Jiandong Guo, and Jiandi Zhang, Reentrance of Low-Temperature Nonmetallic Phase of $La_{2/3}Sr_{1/3}MnO_3$ (110) Thin Films, submitted to Physical Review Materials, currently under review.

[35] Mark Huijben, Interface Engineering for Oxide Electronics: Tuning electronic properties by atomically controlled growth, PhD thesis University of Twente, Enschede, The Netherlands (2006).

[36] Stefan Hüfner. Photoelectron Spectroscopy, volume 82 of Solid-State Sciences. Springer-Verlag, Berlin (1995).

[37] Crewe, Albert V; Isaacson, M. and Johnson, D.; Johnson, D. A Simple Scanning Electron Microscope, Rev. Sci. Inst. **40** (2): 241–246(1969).

[38] Klaus van Benthem and Stephen J. Pennycook, Imaging and spectroscopy of defects in semiconductors using aberration-corrected STEM, Appl. Phys. A **96**, 161(2009).

[39] Kisielowski, C.; Freitag, B.; Bischoff, M.; Van Lin, H.; Lazar, S.; Knippels, G.; Tiemeijer, P.; Van Der Stam, M.; von Harrach, S.; Stekelenburg, M.; Haider, M.; Uhlemann, S.; Müller, H.; Hartel, P.; Kabius, B.; Miller, D.; Petrov, I.; Olson, E.A.; Donchev, T.; Kenik, E.A.; Lupini, A.R.; Bentley, J.; Pennycook, S.J.; Anderson, I.M.; Minor, A.M.; Schmid, A.K.; Duden, T.; Radmilovic, V.; Ramasse, Q.M.; et al.. "Detection of Single Atoms and Buried Defects in Three Dimensions by Aberration-Corrected Electron Microscope with 0.5-Å Information Limit". Microscopy and Microanalysis. **14** (5): 469–477 (2008).

[40] Mundy, Julia A.; Hikita, Yasuyuki; Hidaka, Takeaki; Yajima, Takeaki; Higuchi, Takuya; Hwang, Harold Y.; Muller, David A.; Kourkoutis, Lena F., Visualizing the interfacial evolution from charge compensation to metallic screening across the manganite metal–insulator transition, Nature Communications. **5**, 3464 (2014).

[41] A. Ohtomo, H. Y. Hwang, A high-mobility electron gas at the $LaAlO_3/SrTiO_3$ heterointerface, Nature **427**, 423 (2004).

[42] N. Reyren, S. Thiel, A. D. Caviglia, L. F. Kourkoutis, G. Hammerl, C. Richter, C. W. Schneider, T. Kopp, A.-S. Retschi, D. Jaccard, M. Gabay, D. A. Muller, J.-M. Triscone, J. Mannhart, Superconducting Interfaces Between Insulating Oxides, Science **317**, 1196 (2007).

[43] Jian-Feng Ge, Zhi-Long Liu, Canhua Liu, Chun-Lei Gao, Dong Qian, Qi-Kun Xue, Ying Liu & Jin-Feng Jia, Superconductivity above 100 K in single-layer FeSe films on doped SrTiO3 Nature Materials **14**, 285–289 (2015).

[44] T. Ohnishi, K. Shibuya, and M. Lippmaa, D. Kobayashi, H. Kumigashira, and M.Oshima, H. Koinuma. Preparation of thermally stable TiO2-terminated $SrTiO_3$ (100) substrate Surfaces. Appl. Phys. Lett. **85**, 272 (2004).

[45] Stuart B. Adler, Chemical Expansivity of Electrochemical Ceramics, J. Am. Ceram. Soc. **84**, 2117–19 (2001).

[46] Alexey Kalabukhov, Robert Gunnarsson, Johan Börjesson, Eva Olsson, Tord Claeson, and Dag Winkler, Effect of oxygen vacancies in the $SrTiO_3$ substrate on the electrical properties of the $LaAlO_3/SrTiO_3$ interface, Phys. Rev. B **75**, 121404 (2007).

[47] Shogo Miyoshi, Jeong-Oh Hong, Keiji Yashiro, Atsushi Kaimai, Yutaka Nigara, Kenichi Kawamura, Tatsuya Kawada, Junichiro Mizusaki, Lattice expansion upon reduction of perovskite-type $LaMnO_3$ with oxygen-deficit nonstoichiometry, Solid State Ionics 161, 209–217 (2003).

[48] Young-Min Kim, Jun He, Michael D. Biegalski, Hailemariam Ambaye, Valeria Lauter, Hans M. Christen, Sokrates T. Pantelides, Stephen J. Pennycook, Sergei V. Kalinin and Albina Y. Borisevich, Probing oxygen vacancy concentration and homogeneity in solid-oxide fuel-cell cathode materials on the subunit-cell level, Nat. Mater. **11**, 888 (2012).

[49] M. Chi, T. Mizoguchi, L. W. Martin, J. P. Bradley, H. Ikeno, R. Ramesh, I. Tanska and N. Browning, Atomic and electronic structures of the $SrVO_3$-$LaAlO_3$ interface, J. Appl. Phys. **110**, 046104 (2011).

[50] Q. Qiao, R. F. Klie, S. Ogut and J. C. Idrobo, Atomic and electronic structures of $SrTiO_3$/GaAs heterointerfaces: An 80-kV atomic-resolution electron energy-loss spectroscopy study, Phys. Rev. Lett. **85**, 165406 (2012).

[51] V.I. Nefedov, O.A. Baschenko, Relative intensities in ESCA and quantitative depth profiling, J. Electron Specctrosc. Relat. Phenom. **47**, 1-25 (1988).

[52] Finite-Size Corrections for 4-Point Probe Measurements, by J. R. Senna, Instituto Nacional de Pesquisas Espaciais (INPE), Brasil, taken from the following website: http://four-point-probes.com/finite-size-corrections-for-4-point-probe-measurements/.

[53] F. M. Smits, Measurement the of Sheet Resistivities with the Four-Point Probe, The Bell System Technical Journal **37**, 711-718 (1958).

[54] A. Uhlir Jr., ThePotentialsofInfinite Systems of Sources and Numerical Solutions of Problems in Semiconductor Engineering, The Bell System Technical Journal **34**, 105 (1955).

[55] D.K. Schroeder, Semiconductor Material and Device Characterization, Wiley 1990.

[56] Bernhard Kramer and Angus MacKinnon, Localization: theory and experiment, Rep. Prog. Phys. **56** 1469 (1993).

[57] Patrick A. Lee and T. V. Ramakrishnan, Disordered electronic systems, Rev. Mod. Phys. **57**, 287 (1985).

[58] N. F. Mott, Electrons in disordered structures, Adv. Phys. **16**, 49 (1967).

[59] J. T. Edwards and D. J. Thouless, Numerical studies of localization in disordered systems, Phys. C **5**, 807 (1972).

[60] D. C. Licciardello and D. J. Thouless, Constancy of Minimum Metallic Conductivity in Two Dimensions, Phys. Rev. Lett. **35**, 1475 (1975).

[61] D. C. Licciardello and D. J. Thouless, Conductivity and mobility edges for two-dimensional disordered systems,J. Phys. C: Solid State Phys. **8**, 4157 (1975).

[62] F. J. Wegner, The mobility edge problem: Continuous symmetry and a conjecture, Z Phys, B **35**, 207 (1979).

[63] F. J. Wegner, Disordered system with n orbitals per site: n=∞ limit, Phys. Rev. B **19**, 783 (1979).

[64] S. Hikami, Anderson localization in a nonlinear-σ-model representation, Phys. Rev. B **24**, 2671 (1981).

[65] K. B. Efetov, Supersymmetry and theory of disordered metals, Adv. Phys. **32**, 53 (1983).

[66] E. Abrahams, P. W. Anderson, D. C. Licciardello and T. V. Ramakrishnan, Scaling Theory of Localization: Absence of Quantum Diffusion in Two Dimensions, Phys. Rev. Lett. **42**, 673 (1979).

[67] D. J. Thouless, Maximum Metallic Resistance in Thin Wires, Phys. Rev. Lett. **39**, 1167 (1977).

[68] H. Fukuyama, Effects of Interactions on Non-Metallic Behaviors in Two-Dimensional Disordered Systems, J. Phys. Soc. Jpn **48**, 2169 (1980).

[69] H. Fukuyama, Effects of Mutual Interactions in Weakly Localized Regime of Disordered Two-Dimensional Systems. I. Magnetoresistance and Spin-Susceptibility, J. Phys. Soc. Jpn **50**, 3407 (1981).

[70] T. Tsuzuki, Log E dependence of the conductivity in a two-dimensional random system, Physica B **107**, 679 (1981).

[71] N. F. Mott and M. Kaveh, The conductivity of disordered systems and the scaling theory, J. Phys. C **14**, L659 (1981).

[72] B. L. Altshuler, A. G. Aronov, and D. E. Khmel'nitskii, Suppression of localization effects by the high frequency field and the nyquist noise, Solid State Commun. **39**, 61 (1981).

[73] S. Hikami, Spin-Orbit Interaction and Magnetoresistance in the Two Dimensional Random System, A. I. Larkin and Y. Nagaoka, Prog. Theor. Phys. Vol. **63**, 707 (1980).

[74] A. M. Finkel'shtein, Influence of Coulomb interaction on the properties of disordered metals, Sov. Phys. JETP, **57**(1), 97-108 (1983).

[75] A. M. Finkel'shtein, On the frequency and temperature dependence of the conductivity near a metal-insulator transition, JETP Lett., **37** (9), 517-520 (1983).

[76] A.M. Finkel'shtein, Metal–insulator transition in a disordered system, Sov. Phys. JETP, **59**(1), 212-219 (1984).

[77] A. M. Finkel'stein, Weak localization and coulomb interaction in disordered systems, Z. Physik B **56** (3), 189-196 (1984).

[78] H. Fukuyama, Electron-Electron Interactions in Disordered Systems, Editors: A.L. Efros and M. Pollak, Amsterdam:Elsevier, p155 (1985).

[79] B. L. Altshuler and A. G. Aronov, Contribution to the theory of disordered metals in strongly doped semiconductors, Sov. Phys.JETP **50**, 968 (1979).

[80] B. L. Altshuler and A. G. Aronov, Electron density of states and energy relaxation time in magnetic field, Solid State Commun. **38**, 11-15 (1981).

[81] B. L. Altshuler and A. G. Aronov, Electron-Electron Interactions in Disordered Systems, Editors: A.L. Efros and M. Pollak, Amsterdam:Elsevier, p1 (1985).

[82] C. Castellani, C. Di Castro, P. A. Lee, and M. Ma, Interaction-driven metal-insulator transitions in disordered fermion systems, Phys. Rev. B **30**, 527 (1984).

[83] R. Raimondi, C. Castellani, and C. Di Castro, Zeeman spin-splitting-frequency renormalization in disordered interacting electronic systems, Phys. Rev. B **42**, 4724 (1990).

[84] B. L. Altshuler, A. G. Aronov, and P. A. Lee, Interaction Effects in Disordered Fermi Systems in Two Dimensions, Phys. Rev. Lett. **44**, 1288 (1980).

[85] Maekawa, S. & Fukuyama, H. Magnetoresistance in Two-Dimensional Disordered Systems: Effects of Zeeman Splitting and SpinOrbit Scattering. J. Phys. Soc. Jpn. **50**, 2516–2524 (1981).

[86] N. F. Mott and E. A. Davis, Electronic Processes in Non-Crystalline Materials, 2nd edition, Oxford: Clarendon (1979).

[87] David Emin, Phonon-Assisted Jump Rate in Noncrystalline Solids, Phys. Rev. Lett. **32**, 303 (1974).

[88] Y. C. Lan, X. L. Chen, M. He, Structure, magnetic susceptibility and resistivity properties of $SrVO_3$, J. Alloys Compd. **354**, 95 (2003).

[89] I.H. Inoue, H. Makino, I. Hase, M. Ishikawa, N.E. Hussey, M.J. Rozenberg, Systematic control of the electron correlation and an anomalous metallic state in $Ca_{1-x}Sr_xVO_3$ near the Mott transition, Phys. B: Condens. Matter **237**, 61 (1997).

[90] V. Giannakopoulou, P. Odier, J.M. Bassat, J.P. Loup, $SrVO_3$ and Sr_2VO_4, electrical properties below and above room T, Solid State Commun. **93**, 579 (1995).

[91] W. Noun, B. Berini, Y. Dumont, P.R. Dahoo, N. Keller, Correlation between electrical and ellipsometric properties on high-quality epitaxial thin films of the conductive oxide $LaNiO_3$ on STO (001), J. Appl. Phys. **102**, 063709 (2007).

[92] B. Berini, N. Keller, Y. Dumont, E. Popova, W. Noun, M. Guyot, J. Vigneron, A.

Etcheberry, N. Franco, R.M.C. da Silva, Reversible phase transformation of $LaNiO_{3-x}$ thin films studied in situ by spectroscopic ellipsometry, Phys. Rev. B **76**, 205417 (2007).

[93] M. Gu, S.A. Wolf, J. Lu, Accessing a growth window for $SrVO_3$ thin films, Adv. Mater. Interfaces **1**, 1300126 (2014).

[94] Arnaud Fouchet, Mickaël Allain, Bruno Bérini, Elena Popova, Pierre-Eymeric Janolin, Nicolas Guiblin, Ekaterina Chikoidze, Joseph Scola, David Hrabovsky, Yves Dumont and Niels Keller, Study of the electronic phase transition with low dimensionality in $SrVO_3$ thin films, Materials Science and Engineering B **212**, 7–13 (2016).

Vita

Gaomin Wang was born in December 1988, in Harbin, China. She completed her undergraduate education in Physics in the University of Science and Technology of China (USTC) in 2009. Upon graduation, she came to Louisiana State University in pursuit of her degree of Doctor of Philosophy in Physics. She is currently a PhD candidate in Physics and a dual degree master candidate in Applied Statistics in LSU. She is expected to finish the education in both programs by 2018.